

Report on Alternative Divertor Concepts WP-DTT1 and WP-DTT1/ADC (2014-2020)

Written by Fulvio Militello

19/02/2021

Table of Contents

0. EXECUTIVE SUMMARY	2
1. INTRODUCTION	4
2. EQUILIBRIUM AND COIL OPTIMIZATION.....	7
3. PHYSICS OF THE ADCS.....	10
3.1 MULTIFLUID CALCULATIONS.....	13
3.2 TURBULENCE CALCULATIONS.....	25
4. INTEGRATION IN THE MACHINE.....	31
4.1 STRUCTURAL CALCULATIONS OF THE TF COILS	31
4.2 CONTROL.....	39
4.3 REMOTE HANDLING.....	47
4.4 PUMPING	51
4.5 NEUTRONICS	58
5. THE ADC CONTINUUM AND HYBRID SOLUTION.....	66
6. CONCLUSIONS AND RECOMMENDATION	71
APPENDIX I	73
APPENDIX II	75

0. Executive summary

This report summarizes the activities of the work package DTT1/ADC and its predecessor WP-DTT1 (alternative configuration part). Its scope, as per the work plan, was to “*seek to assess the potential benefits and costs of alternative plasma exhaust solutions for DEMO, identify promising candidates*”. This was done in a synergetic way using multiple approaches spanning from predictive physics simulations of the alternative divertor configurations (ADCs) to investigations of the structural response of the toroidal field coils, of the controllability of the plasma, of the pumping efficiency and of the neutronic irradiation, thus providing a comprehensive overview of the problem.

It is important to note that this was a preliminary comparative analysis. Preliminary because while the tools used were state of the art, a number of simplifications were taken to provide an answer within reasonable time – yet all the approximations were chosen making sure not to leave out dominant effects. Comparative because the emphasis was not on the absolute values given by the calculations but rather on the trends observed and the differences between a configuration and another. Here it is important to remark that we tried to make comparisons as fair as possible by enforcing standards and documenting all the analysis properly.

Five configurations were analysed at different and compared to the baseline single null divertor (SND). These were the double null divertor (DND), the X-divertor (XD), the Super-X divertor (SXD), the Snowflake divertor (SFD). In addition, also a hybrid SND/SXD solution was examined as a compromise between the two. It is important to note that these labels are not representative of an exact design or fixed constraints as what matters in ADCs are their features, which, if properly designed, could lead to benefits on the machine operations. Hence, we present here a specific incarnation of the configurations above, and therefore generalizations might be unwise (e.g. if one of *our* ADCs is bad, it does not mean that that ADC is bad if implemented with a different design).

From the physics point of view, the initial calculations with TECXY and SOLEDGE2D have been replaced in the last two years by SOLPS, the code used to design the ITER exhaust system. While some trends were captured already by the older simulations, others were not (e.g. due to the lack of radiation physics in the old runs). Concerns on the asymmetry of the solutions in long outer connection length cases did not appear as critical in the SOLPS simulations. The latter were organised in matrix scans, systematically performing hundreds of simulations for each configuration, changing fuelling, seeding and power levels. Operating spaces were identified by imposing constraints on the target loads and core physics (e.g. maximum heat load at the target, maximum separatrix density or impurity concentration). With this approach, it was shown that configurations like the SXD or the XD provide a margin of roughly a factor two with respect to the SND. Importantly, the results suggested that a higher power margin was possible at least for the SXD. A concern is that the loads in the SFD (minus) are very sensitive to variations of the position of the secondary strike point (this might happen also in the DND). The (ideal) connected DND configuration showed similar performance to the SND and a tendency to develop up down asymmetries. Finally, the work package has performed the first 3D turbulence simulations of ADCs in the community, showing that increased connection length (SXD and XD) or regions of low magnetic shear (SFD) can affect

the turbulent structures and likely change the perpendicular transport. This effect should probably be taken into account in future multifluid comparisons.

A preliminary assessment of the pumping efficiency in the different configurations has shown that none of the configurations (including the SND) can guarantee enough helium removal. Some configurations had problems also with the deuterium and argon pumping (including the SND). This concern, however, is mitigated by the fact that the input for the simulations is not yet reliable as only fluid neutrals were used in the SOLPS simulations employed as boundary conditions for the pumping study. Comparatively, however, it seems like some ADCs have a slight advantage (SXD) and some disadvantage (XD) with respect to the SND. For this specific study, however, it is probably too early to have a reliable statement.

From the engineering point of view, all the ADCs were generated with only six external PF coils and with a design that respected the force constraints on the coils and on the plasma features in general. Structural calculations were performed with finite element methods and showed that accommodating ADC features comes at the cost of increasing stresses. All the configurations are generally more challenging than the baseline and present criticalities but, in some cases, these are comparable with those in the SND (at least the simplified version used in the WP-DTT1/ADC analysis). Solutions like reinforced intercoil structures (box design like IDTT's) and D-shape morphing (introduced by PPPT and adopted by the WP) were used to minimize the stresses and bring some ADC designs close to pass against a Von Mises yield stress criterion (adopted elsewhere in EUROfusion, but WP-DTT1 typically used the more stringent stress intensity criterion).

Control of the ADCs is particularly critical due to a number of factors. The first is that our preliminary designs were not optimized, and passive structures were rather far from the plasma, thus making it less stable. As a consequence, changes in the plasma equilibrium (I_i and β_{pol}) can induce displacements of the order of 10-20cm, an order of magnitude larger than the SND's. Also, ADC features typically lead to poloidal field coils farther away from the plasma, thus making control with only external coils very challenging. This conspires to generate power requests for the control system that are very large and often unacceptable. On the other hand, small internal control coils could bring the power requests from hundreds of MW down to 10-20MW in the worst-case scenario (typically around 1-2MW), thus making control feasible. Of course, the presence of internal coils brings a number of engineering complexities that will have to be weighed in the overall machine integration and might not be possible. Note, however, that also for the SND the power requests without internal coils would be very large and of the order of several hundreds of MW in critical phases like the start of ramp down. Particularly concerning, though, is the fact that the potential benefits of some configurations rely on precise positioning of the secondary X-points (DND and SFD – ideal and minus), and if this cannot be continually and reliably ensured such benefits might be lost.

Remote handling was assessed for our configurations with the help of PPPT's KDII3 and led to a redesign of the ports and coil positioning in order to ensure installation, extraction and maintenance of the divertor and breeding blanket. It is worth noticing that there are conflicting requirements between the need to have large ports (remote maintenance) and the need to strengthen the TF coil cage rigidity (structural calculations) ensuring proper

nuclear shielding (neutron loads) and positioning the PF coils in appropriate places to generate ADC features (control and equilibrium). Most of these problems are common to the SND and a delicate balance has to be found in order to ensure success. It is therefore important to coordinate these activities synergistically from the very beginning.

The neutronics analysis performed on the SND, XD and SXD configurations shows relatively minor differences and the tritium breeding ratio is basically unaffected by the different designs. While detailed recommendations are available in the technical report, it is worth noting that in our calculations both the baseline and the ADCs have an excessive nuclear heating in the TF coils, well above the limit imposed on the cryogenic superconducting coils. The SXD has a marginally better response close to the lower port due to the amount of material in the divertor region, but it still fails both at the midplane and near the upper port (the other configurations are concerning everywhere in the TF coil's outer limb. Adjusting the port wall thickness or improving the shielding provided by the vacuum vessel might help in this respect.

The conclusions of this work are multifaceted. Our physics studies suggest potential benefits associated with longer outer connection length (XD and SXD). This would consist in an increased margin with respect to fluctuations in the plasma parameters (density, impurity concentration, power). However, configurations relying on a secondary X-point (DND and SFD ideal and minus) do not seem to perform better than the SND, at least at this stage of the analysis. The engineering of the ADCs is necessarily costlier than that of the baseline and it shares several of its criticalities, often in a more acute way. In particular, TF coil stresses and power requirements for control are systematically equal or higher than the baseline (in certain cases much higher). Other areas like the passive vertical stability, the neutronic irradiation and the tritium breeding ratio are nearly identical in all divertor configurations considered (including the baseline).

The solution proposed is to investigate the "continuum" of the exhaust solutions, modifying the baseline incrementally to provide some benefits without affecting significantly the surrounding engineering. A preliminary hybrid SND/SXD configuration was investigated and proved to be a compromise between the two designs, improving the physics of the SND and decreasing the engineering complexity of the SND.

Eventually, whether to implement some form of ADC or hybrid solution should be tied to the confidence of the DEMO team that the baseline solution will work as designed. The additional cost associated with the ADCs is repaid by the margin they give in the face of uncertainty.

1. Introduction

The exhaust of particles and energy in DEMO will be much more demanding than in current machines in terms of both physics and engineering. In particular, the power that needs to be handled by the exhaust system scales with the fusion power, and this fact is in the most fundamental laws of fusion physics, as it is connected with the production of α particles in the fusion reactions. Practically, this means that for a GW reactor the power that needs to be safely absorbed by the walls is in the hundreds of megawatts, at least one order of magnitude larger than what we are experiencing in today's largest tokamaks. In addition, the engineering

of the reactor poses new limitations on what can be built, as plasma facing material properties, remote maintenance and installation, port dimensioning and acceptable forces and stresses on the structural components all conspire to complicate the design.

Focusing on the exhaust system, one of the biggest concerns is to find an operational space that is sufficiently robust and reliable, even in the presence of unavoidable off-normal events and under uncertainty, especially in the physics extrapolation. In particular, the first line of defence against the exhausted power, the divertor, has to be able to sustain steady state loads that, if unmitigated, would reach hundreds of MW/m², well beyond acceptable structural limits for the plasma facing components. Additionally, once in the operating mitigated state, the divertor needs to be able to dissipate the additional power that unexpected transients could produce (maybe from failed pellet injection, radiation fluctuations or emergency ramp downs).

The current European DEMO design is based on the ITER exhaust solution: a single null divertor (SND) with vertical targets. However, extrapolation is not obvious, as the two machines will operate in different regimes. Core radiation will be much larger in DEMO (~66% versus ~33% in ITER) but with similar power crossing the separatrix (~150MW for DEMO and ~100MW for ITER). This means that DEMO will have a large upstream reservoir of power (~300MW versus ~ 50MW) that can endanger a divertor fully detached and under a lot of strain. To give the measure of the problem, a 10% variation in core radiation would unleash an additional ~30MW towards a divertor that in its ideal operation point already needs to dissipate 90% of the power it receives (optimistically assuming a wetted area of 3m² and material limits at 5MW/m²). The DEMO divertor will therefore need to operate in fully detached conditions (ITER will be semi-detached), which implies that there is a risk the detachment front could reach the X-point and cool off the pedestal or destabilize the discharge. Active detachment control in DEMO, however, will be a challenge never faced before due to lack of neutron resistant sensors and actuators so that solutions that provide passive detachment stabilization of would be helpful.

This is an unprecedented physics and engineering challenge. The large uncertainties in the physics models, which lead to difficult extrapolations and an intrinsic lack of confidence in the predictions, implies that back up strategies and alternative approaches need to be developed as a mitigation measure. The importance of this issue is well expressed in the 2018 EUROfusion roadmap, which states:

“A reliable solution to the problem of heat exhaust and helium removal is one of the main challenges in realising magnetic confinement fusion. It is conceivable that the baseline strategy, with a conventional divertor as pursued in ITER, cannot be extrapolated to DEMO and commercial fusion power plants. Hence, in parallel to the programme in support of the baseline strategy, an aggressive programme on alternative solutions for the heat exhaust is necessary. This will focus on improved plasma facing materials and components, and on new divertor configurations. Several concepts will be tested at a proof-of-principle level in upgrades of existing devices, and their technical feasibility for application in a fusion power plant are being assessed.”

These observations motivate research of alternative divertor configurations (ADCs) for the plasma exhaust. EUROfusion has systematically studied these alternatives since 2014 through the DTT1 Work Package. The EUROfusion Work Plan 2019/20 elaborates the specific role of the Alternative Divertor Configurations Work Package in addressing these problems:

“The WP DTT1-ADC project seeks to assess the potential benefits and costs of alternative plasma exhaust solutions for DEMO, identify promising candidates [...].”

The work presented in this report spawns from EUROfusion's recognition that DEMO's exhaust might be significantly different from what we have in current machines and even ITER. Here we give an updated and comprehensive report of the results achieved in the WP-DTT1/ADC Work Package, which mix both physics and engineering considerations. While the potential benefits need to be weighed against the unavoidable cost that the additional complexity entails, the latter must be accepted if the single null divertor (SND) cannot provide a solution. In particular, we investigated four ADCs: the double null (DND), the Snowflake (SFD) the X (XD) and Super-X (SXD) divertors.

It is in the nature of our analysis to be comparative. Indeed, given the large uncertainties on exhaust physics and technology, and the unprecedented level of complexity of the problem, the only wise approach is to dismiss predictions that aim at absolute values and rather focus on similarities, differences and trends observed between the configurations investigated. This, however, requires a rigorous methodology in which analyses are carried out in a standardized way, with the same tools and with agreed procedures, so that the comparison is fair. Despite the triviality of this argument, its practical application is far from easy.

The second important methodological aspect is that the work presented was deeply integrated, with cross-fertilization and continuous exchanges between the physics and engineering aspects, so to form a consistent picture where each configuration analysed can be represented as a single entity, see figure below.

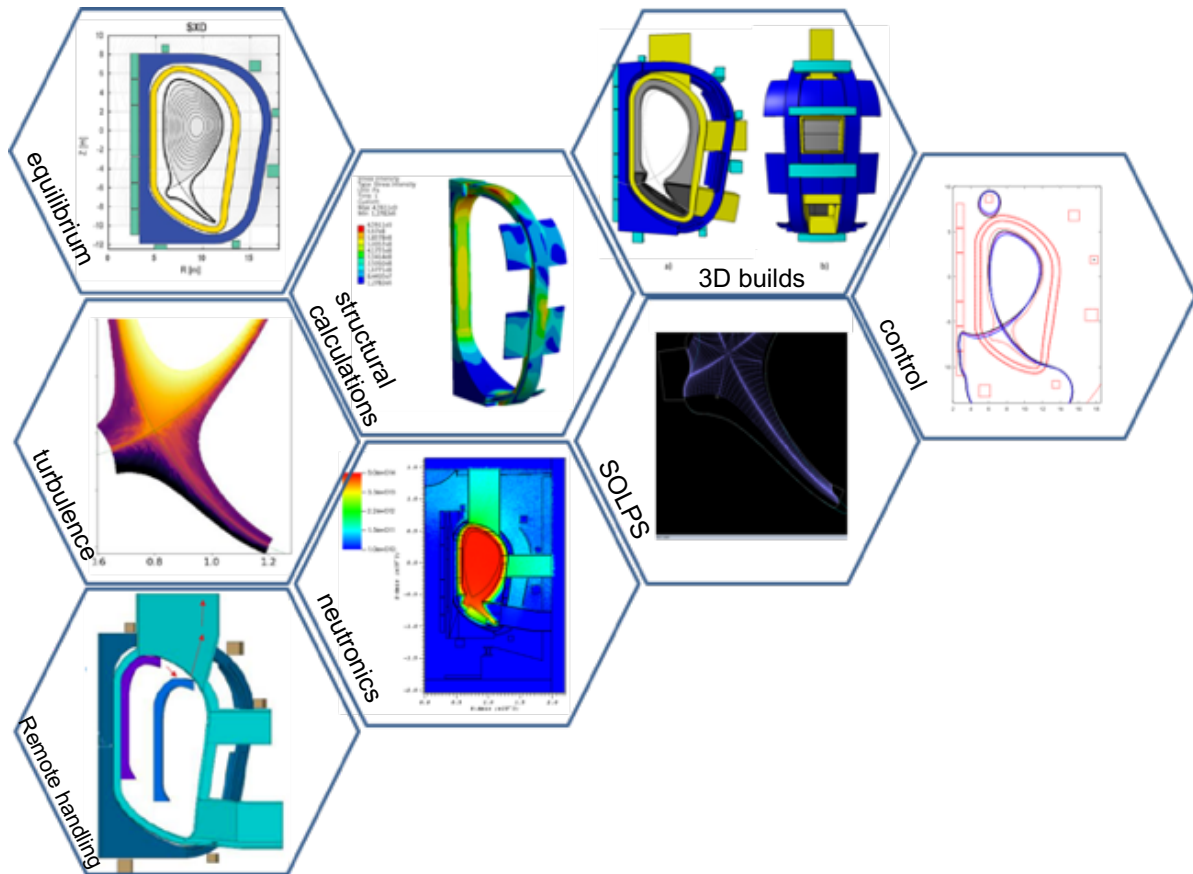


Figure 1: Different activities carried out in a synergistic way within the work package to achieve a comprehensive view of each ADC (here the Super-X configuration is taken as an example)

Finally, the results presented here must be interpreted as a step in the right direction rather than a conclusive assessment of the properties of the ADCs, or a recommendation for how to build an exhaust system for a reactor. Indeed, we started from ADCs for DEMO that included the features that were originally predicted to be beneficial, but that are not yet optimized. This initial attempt cannot lead to the 'right' solution straight away, as this must be the result of iterations based on the lessons learned.

2. Equilibrium and Coil Optimization

The first step the work package took was to design toroidal and poloidal field coil layouts appropriate to accommodate the main features of the ADCs (discussed in Section 3). A number of constraints were given by the PPPT (WP-PMI) in 2015 and engineering team on the desired plasma and engineering of the machine. These were:

Plasma current profile parameters:

- Plasma current $I_p = 19.07MA$
- poloidal beta $\beta_p = 1.141$
- internal inductance $l_i = 0.8$

Flat-top plasma shape parameters:

- Major Radius, $R \cong 8.938m$

- Aspect Ratio, $A \cong 3.1$
- Elongation, $k_{95} \cong 1.65$
- Triangularity, $\delta_{95} \cong 0.33$
- Plasma Volume, $V_p \cong 2466 \text{ m}^3$

PF coil current:

- Poloidal coil cross-sections determined assuming a current density limit of $12.5\text{MA}/\text{m}^2$ (value imposed by PMI even if ITER and IDTT limits are larger).

Magnetic field:

- The maximum field at the location of the PF and CS coils not exceeding 12.5 T.

Vertical Forces:

- Maximum vertical force on a single PF not exceeding 450 MN;
- Maximum vertical force on the CS stack not exceeding 300 MN;
- Maximum separation force in the CS stack not exceeding 350 MN;
- In case of two or more PF coils positioned closer than 3m poloidally, the total vertical force from the PF coils on the supports not exceeding 450MN.

TF coils:

- A 16 TF coil cage shaped to keep ripple below 0.6% (note that the original design was with 18 TF coils);
- TF shells not up-down symmetric

Divertor:

- Distance between the divertor plates and the X-point region $<1\text{m}$;
- Minimum grazing angle at the target 1.5deg.

In all the configurations discussed in this report, these constraints are always satisfied using only six PF coils¹ external to the TF coil cage, as requested by WP-PMI. With respect to the SND, a number of modifications were implemented. In particular, for the XD and SFD the bottom part of the TF coils was deformed to bring the divertor PF coils in specific positions to ensure flux expansion and a second order null, respectively; for the SXD the bottom outer part of the TF coil was stretched outward to allow for an outer strike point at large major radii; for the DND an up/down symmetrization of the coils was needed.

The original layout in 2014 included 18 toroidal field coils, which were later reduced to 16 due to engineering considerations related with the port size for remote handling driven by the baseline DEMO design. In order to maintain the ripple constrains, this required making the TF coils larger and shifting their outer limb farther away from the plasma. In addition, the baseline elongation went from 1.55 to 1.65 and the major radius from $R=8.76\text{m}$ to $R=8.94\text{m}$. A partial redesign of the coils was completed in 2017 and a full redesign in 2018.

¹ The six PF coils are numbered clockwise from the top left and called P1, P2, ...

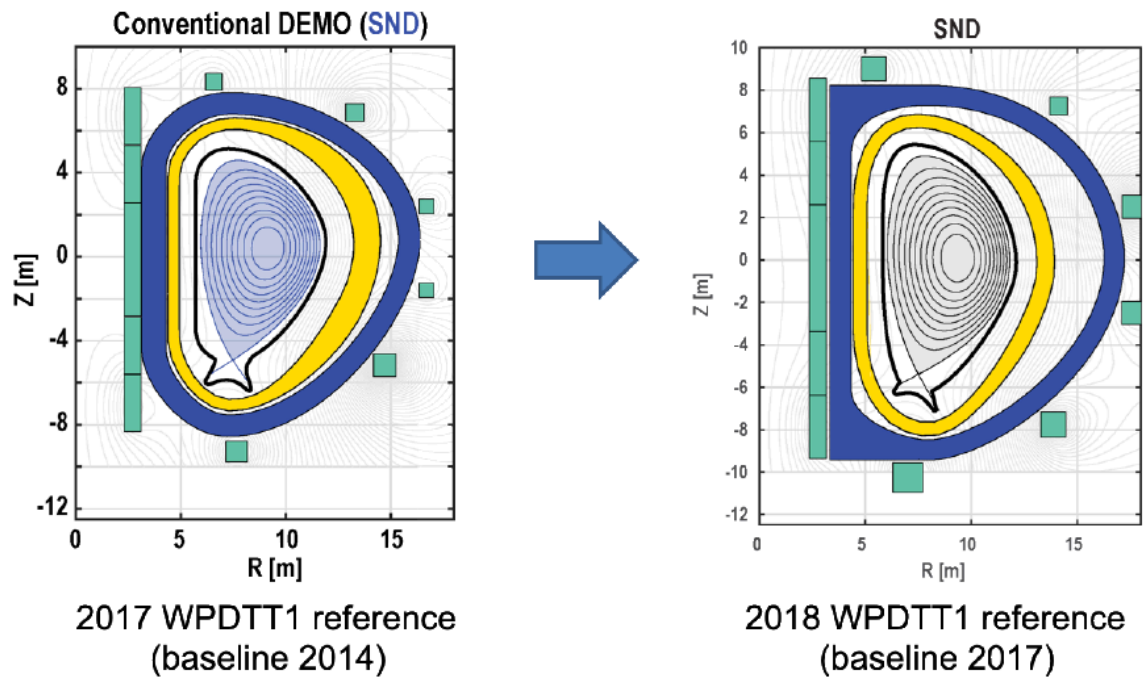
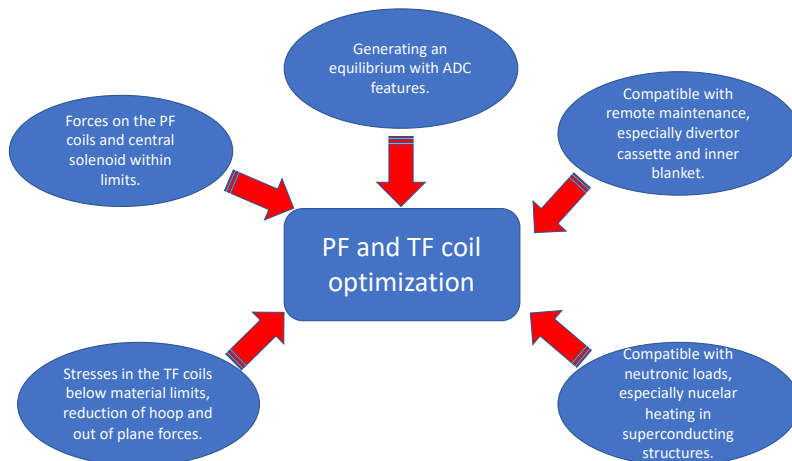


Figure 2: Change in the equilibrium and coil layout.

During the last two years, it was evident that a new redefinition of the coil layout was necessary in order to take into account different conflicting elements entering the problem: not only forces on the coils, but also limiting the stresses in the TF coils, allowing enough port space for remote maintenance, avoiding too big gaps between the plasma and the passive structures and PF coils, and ensuring that neutronic loads are not excessive (this last element will be discussed later on, but it did not enter the current redefinition of the layout).



This observation led to new 2020 designs for all the configurations. This final iterations did not lead to a complete redesign, but to adjustments in order to go in the right direction. It would be recommended to take into account all the elements above from the onset, at an early design stage, as this would probably generate a more robust optimum (moving in a space with several local maxima). As a matter of fact, two 2020 configurations were generated, one compatible with remote handling and a second one also optimized for the TF

coil stresses. Not all the analyses in these reports were carried out for all the configuration and the table below maps which analysis will be presented for which configuration.

Table 1: summary of of the analyses performed for all the configurations and for the 2018 and the two 2020 coil designs. V means performed and reported here, X not done and NN not needed.

		Physics (including pumping)	TF stress analysis	Control	Neutronics
SND	2018	V	V	V	V
	2020 (port compatible)	Already port compatible			
	2020 (morphed and port compatible)	Generated by PMI			
DND	2018	V	V	V	X
	2020 (port compatible)	Generated by PMI			
	2020 (morphed and port compatible)	Generated by PMI			
XD	2018	V	V	V	V
	2020 (port compatible)	Already port compatible			
	2020 (morphed and port compatible)	Not generated			
SXD	2018	V	X	V	X
	2020 (port compatible)	NN	X	X	V
	2020 (morphed and port compatible)	NN	V	V	X
SFD	2018	V	X	V	X
	2020 (port compatible)	NN	X	V	X
	2020 (morphed and port compatible)	NN	V	X	X
Hybrid	2020	V	V	V	X

Note that while the latest physics studies were carried out only for the 2018 configurations, the variations in the two 2020 designs are minor as far as this analysis is concerned, since the equilibrium plasma is kept as close as possible to the original.

At any rate, the procedure used for the calculations presented in this report was the following. A CREATE-NL optimization was carried out to generate an equilibrium for each configuration with acceptable forces on the coils and satisfactory magnetic topology features (flux expansion, connection length, position of the outer strike point, or of the secondary X-point, depending on the configuration). Next the configuration was processed with NOVA in order to generate a suitable TF coil, vacuum vessel and first wall, the latter compatible with the given impinging angle at the target, and intercoil structures. NOVA provided also the electromagnetic loads on the coils, and a full structural analysis of the system was carried out with ANSYS (shown in Section 4). This procedure was iterative and required a few steps to converge to acceptable conditions. More details on the procedure are available in Ambrosino et al. Fusion Engineering and Design 146 (2019) 2717–272 and in the level 3 deliverable reports of WP-DTT1.

3. Physics of the ADCs

In the last 20 years, a number of divertor solutions alternative to the standard single null configuration have been developed with the promise of easing the problem of energy and particle exhaust in reactors. We don't have the time to review these concepts or to delve into their predicted benefits, but the interested reader can have detailed information in D.D Ryutov, Phys. Plasmas 14, 064502 (2007); D.D. Ryutov and V.A. Soukhanovskii, Phys. Plasmas

22, 110901 (2015); M. Kotschenreuther, P.M. Valanju, S.M. Mahajan and J.C. Wiley, Phys. Plasmas 14, 072502 (2007); P.M. Valanju, M. Kotschenreuther, S.M. Mahajan and J. Canik, Phys. Plasmas 16, 056110 (2009); and a broad overview in H. Reimerdes et al. 2020 Nucl. Fusion 60 066030 and in F. Militello et al. Nuclear Materials and Energy 2021 (in press).

The most important concept is that it is not the individual configurations per se that provide benefits (the configuration “label”), but rather some of their features, which need to be maximized. In particular, the connection length, the flux expansion (toroidal and poloidal) and the presence of multiple X-points or the order of the null are the parameters that can be used to potentially give advantages. A non-exhaustive list is given in the following table, which shows how some of the features are actually shared by different configurations.

Feature	Potential benefit	Configuration
Longer connection length	Larger collisionality and hence easier access to high-radiation and detached regimes, lower T_{target} , more room for radial transport.	SXD; XD; SFD
Larger poloidal flux expansion	Passive stabilization of detachment front (via different mechanisms), increased connection length and wetted area.	SXD (difficult in DEMO); XD
Larger toroidal flux expansion		SXD
Multiple X-points	Splitting of energy and particle fluxes to multiple targets, Stabilization of the radiation front outside the core, in SFD increased connection length, in DND topological separation of the inner divertor.	DN; SFD

In the following table, we report the values of some of the important features of the 2018 configurations (later iterations of the equilibria did not change these quantities significantly).

Table 2: Equilibrium parameters for the different configurations.

	SN		XD		SXD		SFD		DND	
	in	out	in	out	in	out	in	out	up	
Targets	Poloidal length [m]	19.3	8.8	18.6	11.1	19.1	12.9	19.3	10.5	8.9
	$L_{\parallel}(\rho = 1\text{mm})$ [m]	209	118	234	230	251	201	499	415	114
	$L_{\parallel}(\rho = 3\text{mm})$ [m]	191	100	205	202	223	174	348	260	96
	$f_{x,t}$	6.4	3.5	7.8	13.6	8.30	2.42	13.28	10.3	3.38
	R_t/R_x	0.87	1.11	0.83	1.07	0.83	1.45	0.78	1.21	1.10
	Angle at target [Deg.]	1.50	1.56	1.52	1.49	1.51	1.57	1.50	1.55	1.50

Here L_{\parallel} is the connection length and $f_{x,t}$ is the poloidal flux expansion and R_t/R_x is the ratio of the target to X-point radial position, measuring the toroidal flux expansion. Note that the connection length depends on the radial position in the SOL and has different values from the midplane to inner and midplane to outer target. Furthermore, rigorously our SXD divertor lacks poloidal flux expansion (it is lower than the SND), which is one of the nominal features of this configuration. This is because it is extremely difficult to provide both toroidal and poloidal flux expansion with only six external PF coils, and this can be seen as an intrinsic limitation of this configuration in reactor relevant designs. Our SXD is therefore more of a “long leg divertor” than an archetypal “Super-X”.

Another important observation is that the increase of the connection length is observed in the XD, SXD and SFD, but for the latter it is concentrated at the X-point, where the poloidal field is low, while for the XD and SXD this increase is mostly in the divertor leg.

The discussion so far, and in literature in general, is typically concerned about the magnetic topology and structure of the equilibrium and how this can affect the exhaust. However, the equilibrium only provides the backbone of the problem, with the plasma dynamics (and the perpendicular transport in particular) playing a potentially major, yet often neglected, role. Turbulence can well be affected by the magnetic geometry and different ADCs could be characterized by significantly different transport features. This is an important and unexplored area of research, which we have contributed developing by stimulating, sponsoring and carrying out the first turbulent simulations of ADCs in the world (as far as we are aware).

Finally, experimental results in several machines [see e.g. Soukhanovskii Plasma Phys. Control. Fusion 59 (2017) 064005; Theiler et al 2017 Nucl. Fusion 57 072008; Reimerdes et al. Nucl. Fusion 57 (2017) 126007] have produced ambiguous results about the physics of ADCs so far. The experimental findings reported are sometimes conflicting with the theoretical predictions and also with each other. It is important to notice that a lot of care should be used

when interpreting these results, as the extrapolation from current devices to reactors is neither trivial nor straightforward. A full Tungsten environment with large impurity seeding can significantly change the physics of detachment with respect to Carbon machines carrying out fueling ramps (recycling is different, and so is the lowest temperature at the target). Additionally, the sheer size of DEMO will induce several changes in exhaust physics, especially considering the possibility of automatic closure and plasma opacity. The target plasma temperature and density will not be that different from current devices, so that the mean free path will not vary much, but the ratio between the mean free path and the divertor length scale will be massively different, so that effects such as inner/outer target cross talk or impurity segregation might be quite different. Additionally, opacity can provide an additional “blanket” for the plasma that would keep it warmer than otherwise, thus hindering detachment. Finally, non-optimized wall and divertor shapes can lead to local interactions that might muddle the results by inducing recycling or impurity release in an uncontrolled way (or at least in a way that is not compatible with the ideal divertor operations).

In the following we present the findings of the physics analysis of the ADC configurations we developed. Multifluid calculations can provide an analysis of the loads to the target, investigating the power transmission mechanisms from the plasma to neutrals and photons (not bound to the magnetic field and therefore distributing their energy on a larger surface). The turbulence simulations can give some insight on the modifications of the perpendicular transport associated with the ADCs. The two sets of analysis are complementary since the former assume a fixed transport coefficient, while the latter do not include the neutral physics that is so crucial to describe detached states. In a way, neither is fully self-consistent and a future aim would be to merge the two approaches to have a complete description of the problem. On the other hand, a reductionist approach can give some insight on likely trends as long as caution is used in the data interpretation.

3.1 Multifluid calculations

Multifluid simulations of ADCs were part of the WP-DTT1 project since its very beginning. Initial calculations relied on a number of numerical tools and have been reported in H. Reimerdes et al. (2020) Nucl. Fusion 60 066030. These simulations were based on the early equilibria developed in the work package, but newer equilibria are still sufficiently close to the original ones to be able to compare the results.

The initial simulations were not entirely self-consistent, as they approximated the impurity radiation, necessary to dissipate the plasma energy, by artificially reducing the power crossing the separatrix. Also, the separatrix density was fixed at a given value ($2.4 \times 10^{19} \text{m}^{-3}$) and was not allowed to vary as fueling and power changed. The lack of a proper seeding and fueling scan implies that a fair comparison between the configurations is not easy. More detailed information on how these simulations were performed and on their results is available in Appendix I.

More recent calculations carried out in the 2019-2020 period took a different approach and were based on two fundamental principles: 1) standardization and documentation of the tools, of the simulations and of the analysis, all carried out with state-of-the-art tools; 2) identification of an acceptable operating space through systematic variation of the machine

parameters. A group of high level SOPLS-ITER modelers and developers was brought together to simulate the different configurations, thus providing independent calculations within a teamwork approach. The SOLPS-ITER code was chosen as it is the most used tool for divertor design, including ITER's, because it has a wide user base and is extensively developed and because it has been validated in experimental conditions as far as possible (this does not mean that its validation is complete, though, and several doubts still remain in its ability to capture neutral pressure at the target).

So called "matrix scans", inspired by the work of D. Coster, were selected as the basic tool for our exploration. These consist in systematic scans in both fueling and seeding levels (we used Argon as seeded impurity given its good radiation range in the DEMO divertor), generating hundreds of simulations in a grid that represents a wide range of possible divertor conditions (not all of which acceptable). Power scans were carried out as well for selected configurations, thus providing a third dimension to the matrix. Within the matrix scans we could identify simulations that had acceptable core and target conditions using the following criteria:

- 1) Peak heat flux at the target smaller than $10\text{MW}/\text{m}^2$;
- 2) Peak temperature in the divertor (both inner and outer) below 5 eV;
- 3) Maximum Ar concentration at the separatrix below 1%;
- 4) Maximum separatrix density below $4 \times 10^{20}\text{m}^{-3}$ (equivalent to 0.6 of the Greenwald density).

When all these criteria were simultaneously met, we included the simulation in the acceptable operating space. It is clear that these criteria are somewhat arbitrary and should just be taken as an indicative of a reasonable operating range. To give a more global view, the latter could be bound by contour lines of the quantities defining the criteria when plotted against the imposed seeding and impurity flux. While this analysis approach is useful as it provides an overview of the operational flexibility of a given configuration as a function of externally controllable parameters, we also performed a number of more detailed analyses, trying to disentangle the physics mechanisms underlying the behavior of a specific configuration. We will give details later on. It is probably worth remarking that our emphasis in these additional studies was on the understanding of how the core performance (minimum acceptable density and Ar concentration at the separatrix) can be affected by the different configurations. Our working assumption is that core impurity concentration (here Ar, He as higher Z impurities will be used for core radiation, and this is not included in our calculation) and separatrix density have to be as low as possible (a low separatrix density seems to correlate with better pedestal performance, so this quantity should be minimized).

All the configurations were constantly discussed and reviewed in weekly meetings over the course of the project by all the modelers. Most importantly, a specification document was generated early in the project with agreed and standard choices for the simulations, ranging from the flags in the code, to the resolution, to the physics parameters to be used. This maximized the comparability of the configurations and ensured that differences did not arise from mismatching or mistakenly set parameters (note that SOLPS-ITER has something like 900 input parameters, thus standardization of the inputs is essential). Note also that the input files for the different configurations were generated from the same one that the team agreed on. All the simulations (apart from the DND) were uploaded on MDSplus (a software that allows easy access to relevant SOLPS output), so that they could be analysed collectively and

also made available to the community. The full list of MDSplus reference numbers is available here:

<https://docs.google.com/spreadsheets/d/1t9IjX9e5zcznITjoNLfRBXPNaOHLqi65wSURTTQVA7c/edit#gid=456600315>

The grids for the different configurations are given below:

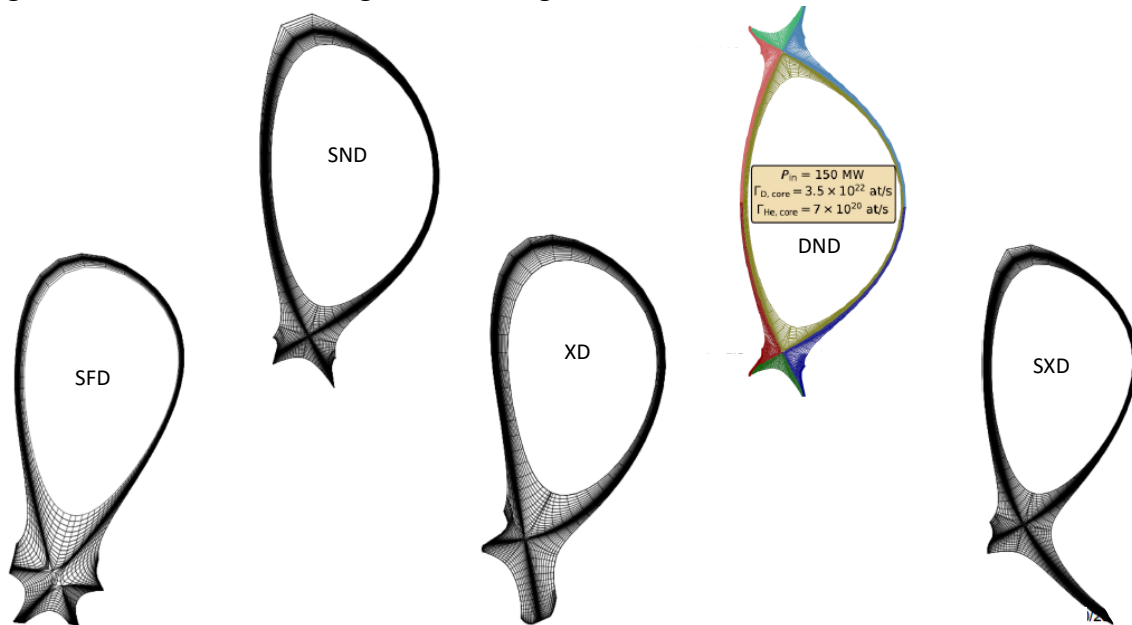


Figure 3: SOLPS grids for all ADC configurations.

An extract of the specification document, discussing all the main assumptions that were used, is given in Appendix II. In order to be able to carry out a systematic and thorough study, we approximated the neutral behavior as fluid, thus avoiding the coupling with the kinetic neutral code EIRINE which, if used, significantly increases the computational cost of the runs and leads to less stable solutions. In addition, we bundled the Ar impurities, thus simplifying their dynamics and behavior. Finally, we did not have fluid drifts in the simulations as they typically lead to more difficult convergence of the code. These are the three major approximations we employed in our study and it is important to remark that they are all likely to affect the quantitative results that we obtained. It is not excluded that they might even affect the qualitative behavior of the plasma. However, the nature of our study is comparative, so the only answer we cared about was whether one configuration was better than another. It is more difficult to think that the approximations we took can reverse the trends, i.e. they alone can lead to significant improvements in one divertor design and significant degradation of performance in the others (or vice versa).

While the Ar bundling and the absence of drifts do not have an a priori justification apart from the fact that they are systematically used in the community, the use of fluid neutrals is more reasonable (although again not completely justified). Indeed, in the DEMO divertor the collisionality will be very large, if nothing else because of the size of the divertors. This implies that the mean free path of the neutrals is small with respect to the system size (of the order of a few cm while the divertor is several meters across), and this gives credit to the fluid approximation. Indeed, the neutral density is at least 10^{20} m^{-3} in the whole divertor region, including the private flux region, and the temperature goes down to a few eV in the proximity

of the target. In all fairness, the fluid approximation would not be valid in the upstream region of the SOL and in addition it does not allow for molecular physics and correct pumping and puffing of the neutrals, which all could affect the results. While considering these effects is computationally expensive, it should be pursued in future simulations. On the other hand, the results shown here are based on what are likely to be the dominant physics mechanisms at play and it is unlikely that additional physics will change the trends described (this is a personal statement and opinion of the Project Leader), or at least no missing mechanism has been clearly identified to challenge the results.

Coming now to the results, the figures below summarize the simulations carried out and show the operating space for the different configurations. It shows the He concentration at the separatrix as a function of the fueling and seeding levels for the SND, SFD, XD and SXD at 150MW crossing the separatrix. The black, purple and yellow lines represent the boundary of the operating space given in conditions 2), 3) and 4) discussed above. Note that condition 1) is always less restrictive than condition 2) and is therefore not used. The operating space for the SND is highlighted with a red circle for reference, it is not present in the SFD and it is on the top right for the XD and SXD. Within the operational space, the separatrix He concentration is always at acceptable levels (<1%).

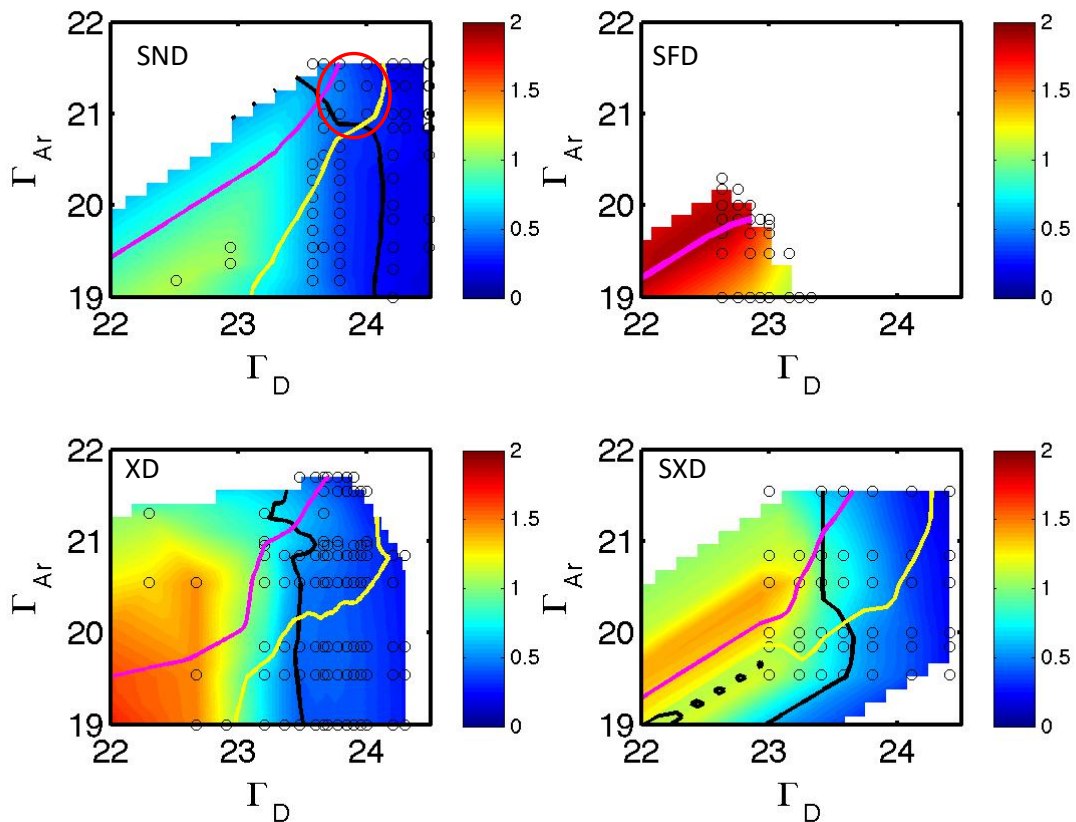


Figure 4: Comparison of the operating space in the seeding and fueling space (axes in log10 scale, expressed in particles per second). The colorplot represents the He concentration, the dots individual simulations and the curves the operational space boundary.

We can immediately notice that the margin in seeding and fueling levels is expanded in the XD and SXD configurations, so that acceptable operating conditions can be achieved with lower Ar seeding and a wider range of fueling levels. This means that the divertor

configuration is less sensitive to external perturbations in these quantities, so that fluctuations caused for example by missing pellets or temporary reductions or increase in the seeding can be absorbed without losing detachment. In other words, these figures show the gain in margin associated with the configurations. We can notice a number of other things.

First of all, we could not find an operating space for the low field side SFD minus configuration we investigated. This configuration had a midplane separatrix separation of 1mm. Several simulations were attempted in the region that is not colored, but they all failed. The fact that we did not find an operating space, however, is not necessarily implying that one does not exist. Indeed, the code inability of producing stable simulations might simply be due to numerical problems. However, the simulations that were successful exhibited an extremely high temperature ($\sim 400\text{eV}$) at strike point 4, the outermost at the low field side. This was higher than in simulations of other configurations at similar levels of seeding and fueling. On the other hand, the only reliable conclusion that we can draw from these simulations is that modelling the SFD configuration in DEMO conditions is undoubtedly challenging and these results is not as mature as those for the other ADCs.

With respect to the DND, the operating space turned out to be comparable if not smaller than the SND (see figure below) due to up/down asymmetries in the loads that will be discussed later.

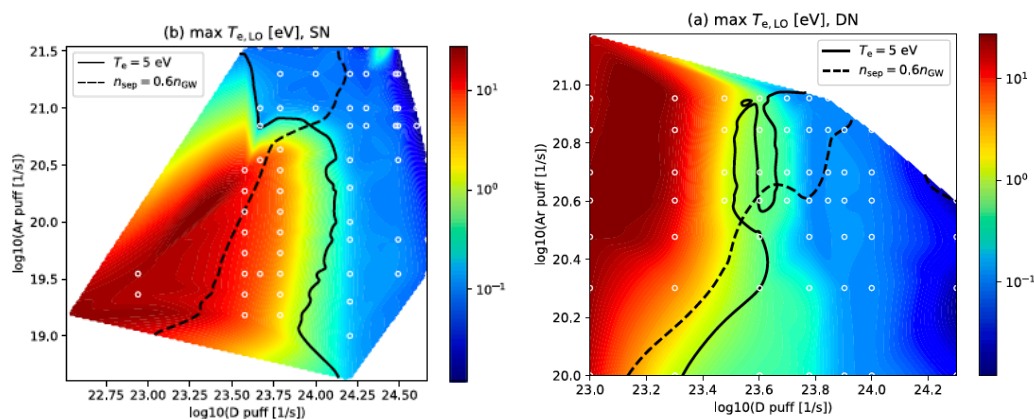


Figure 5: operating space for the DND.

Moving to quantities that are representative of the core conditions, the following figure shows the separatrix Ar concentration as a function of the separatrix density for a number of configurations (SND, XD and SXD).

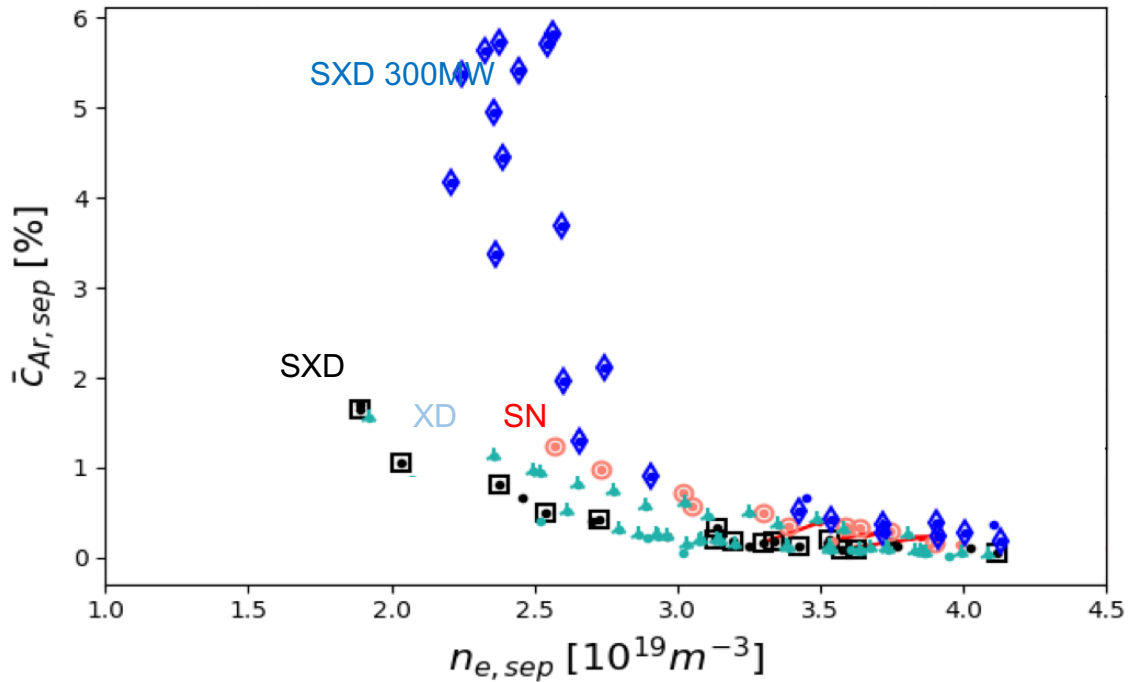


Figure 6: Comparison of core/separatrix parameters for the SND, XD, SXD and SXD at 300MW.

Here, only points in the operating space are represented, although condition 3) is somewhat relaxed and points with an Ar concentration up to 2% (which is probably still acceptable and does not change the operating space massively) are included. What we see is that for a given separatrix Ar concentration, the XD and SXD allow a $\sim 50\%$ lower separatrix densities. In the same way, for a given n_{sep} , less Ar is needed to dissipate the power. Importantly, this suggests that the SXD and XD can reach higher power crossing the separatrix because there is more margin to increase the Ar level in the machine, which is indeed what we find if we increase the P_{sep} to 300MW (blue points). While the SND has already almost exhausted its capability to radiate power at 150MW and does not have an operating space at 300MW (or at least, we could not find it), the SXD is still far from its limit and manages to access higher P_{sep} with an increased Ar level. Note that the figure above shows that the SND 150MW is comparable to the SXD at 300MW in terms of Ar concentration and separatrix density. We indeed find that the operating space for the SXD visibly shrinks with power, as shown in the figure below:

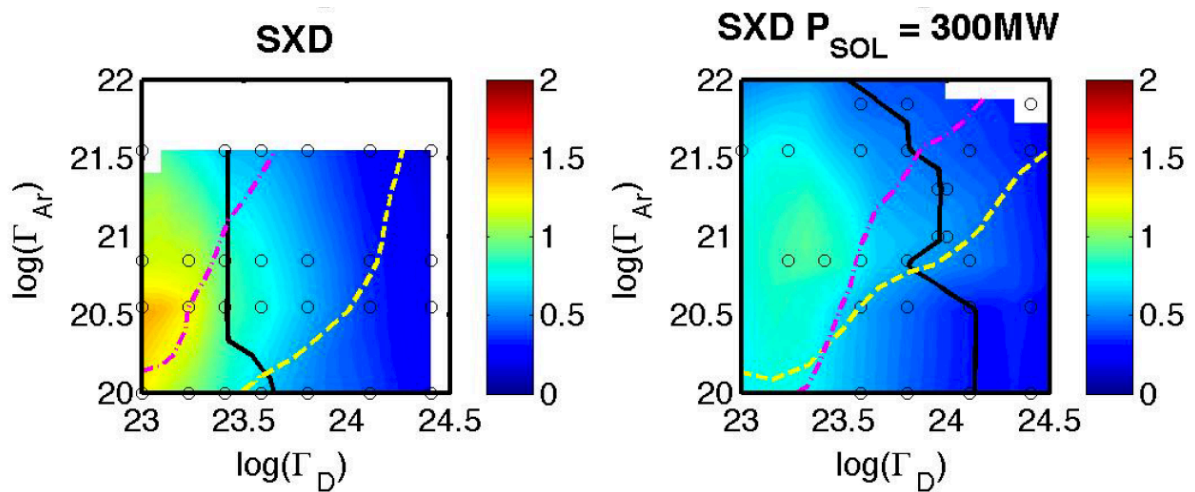


Figure 7: Comparison of the operating space for the SXD at 150MW and 300MW.

More detailed studies were carried out to understand why the SXD performs better than the SND and can achieve higher power. It was found that the radiation in the 150MW SXD is localized at the targets and it has a strong contribution from the deuterium radiation. The 150MW SND, instead, is already radiating quite intensely in the whole divertor region and even above the X-point. As the figure below shows, pushing the SXD to 300MW produces a radiation pattern that is similar to the 150MW SND and both are close to the maximum radiation capability of their respective configuration.

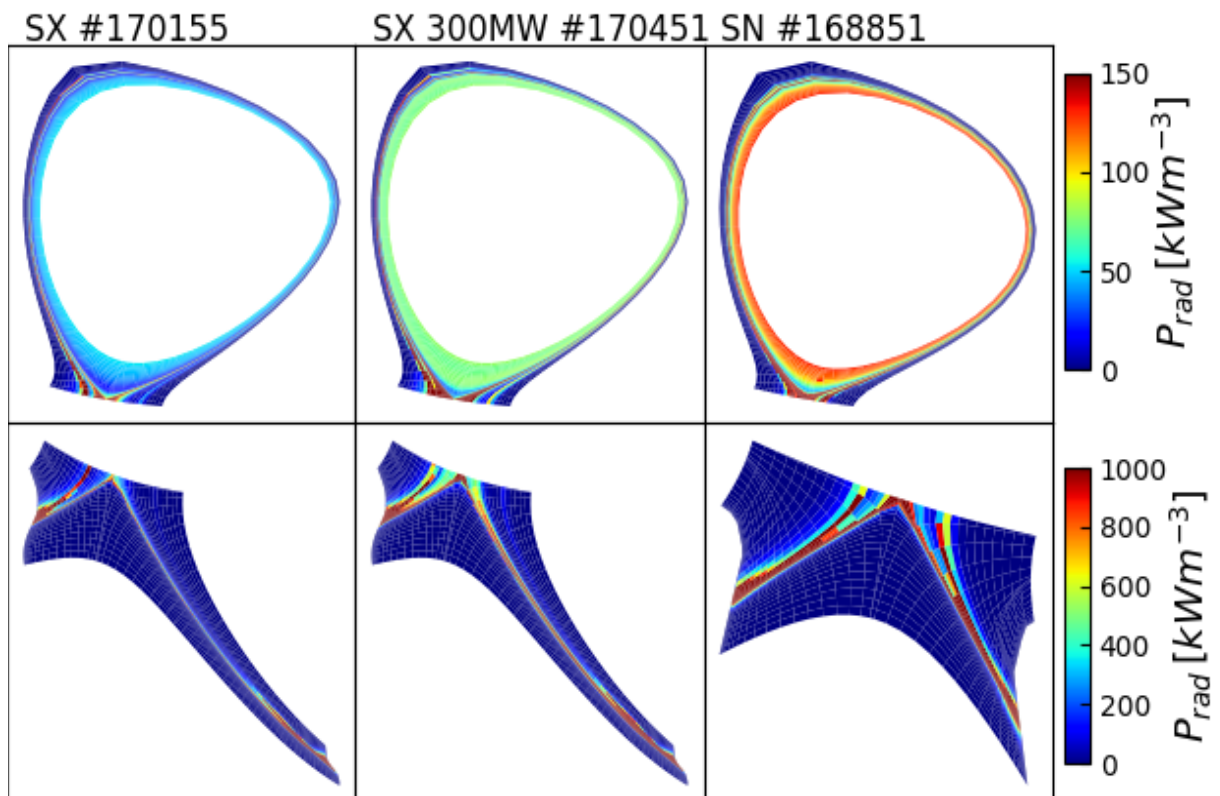


Figure 8: Comparison of the radiation pattern for the SXD at 150MW, at 300MW and the SND. Note the different colorscale for the divertor and the region above the X-point. MDSplus reference numbers are given on top of the plots.

It is also worth remarking that the SXD radiation at 150MW is shared between neutral Ar and deuterium, but the former takes over at 300MW. Interestingly, the operating space for the SXD and XD is entered by increasing the fueling rather than the deuterium level, see Fig. 3. On the other hand, for the SND Ar can play a role, as it does in the SXD 300MW (the maximum temperature boundary of the operating space is now diagonal rather than vertical). This suggests that detachment is achieved with a significant contribution from deuterium radiation in the 150MW XD and SXD, while Ar is important for both SND and 300MW SXD.

The results above can be interpreted using the Lengyel model [M.L. Reinke (2017) Nucl. Fusion 57 034004], which shows that:

$$c_z \propto \frac{q_{\parallel u}}{n_{eu}^2 L_{\parallel}}$$

where c_z is the impurity concentration required to detach, $q_{\parallel u}$ is the upstream energy density flux (proportional to the power crossing the separatrix) and L_{\parallel} is the connection length. Although the expression above is approximated, it clearly shows that increasing the connection length, as the SXD does, reduces the amount of Ar required to detach and therefore gives more margin to absorb more power [see L. Xiang et al. (2021) PPCF for more details]. Although these calculations are performed in equilibrium conditions, they are suggestive of the fact that long connection length solutions (i.e. longer than the SND) can handle power transients better. Time dependent simulations would be needed to verify this statement.

Increasing the outer connection length has risen some concerns in the past, potentially also due to the earlier results of WP-DTT1 presented in Appendix I. Indeed, those simpler simulations showed that whenever the outer L_{\parallel} was increased with respect to the inner L_{\parallel} , a strong in/out asymmetry developed, excessively loading the inner target. As a matter of fact, also two-point model arguments confirm this picture. In our simulations, we dedicated a focused effort to understand the issue of asymmetry and whether it can rule out certain configurations.

First and foremost, it is important to remind the reader that operational space presented in Figs. 3 and 6 is constrained by the maximum temperature and power reaching the divertor, both the outer *and* the inner target. This means that it is the hotter side that provides the boundary and that if we are in the operating space *both* targets are in acceptable conditions. From this, we deduce that even if asymmetries are present (and they are), they do not really matter because the whole divertor is anyway protected.

While this argument could already close the discussion, we anyway made interesting observations while investigating this problem. In particular, we found that the asymmetries in detached regimes cannot really be explained by using simple arguments (like the two-point model) because radiation physics is essential (and not considered in both the usual analytic approximations and in the simulations presented in Appendix I). To prove this point, the figure below shows how asymmetries in the SXD are driven by different fueling levels and Ar concentration (here represented as the ratio between the seeding and fueling level).

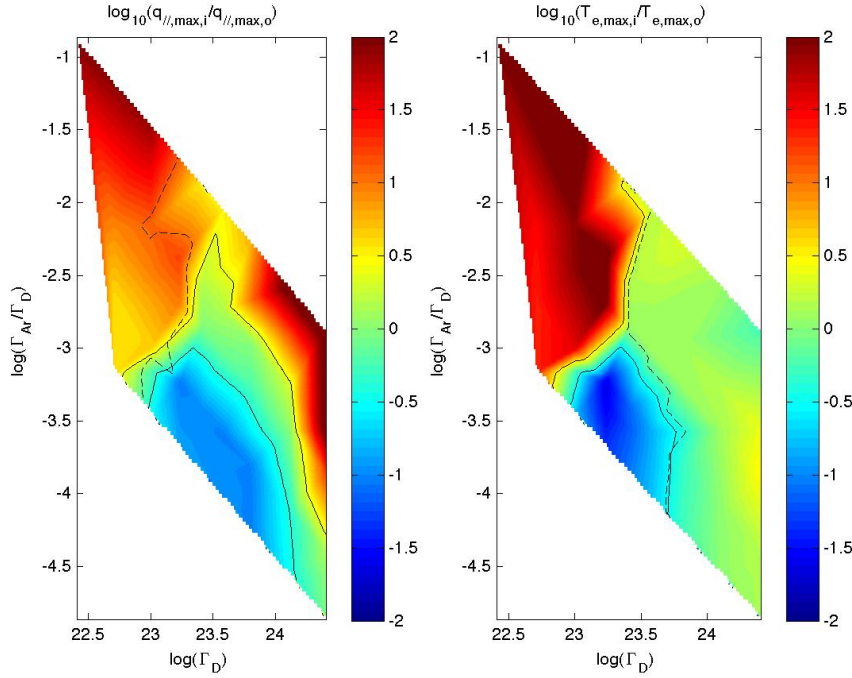


Figure 9: Asymmetry in the SXD expressed as the \log_{10} of the ratio of the inner to outer peak heat flux (left) and peak temperature (right). The solid line is the isocontour of value 1, while the dashed line is the isocontour for condition 1) (left plot) 2) (right plot).

Note that the asymmetry switches depending on the plasma condition, so that there are regions where the low field side is more loaded. Note in particular that the two point model would predict that $q_{//,max,i}/q_{//,max,o}$ is a constant factor determined by the inner to our connection length ratio. It is interesting to notice that the temperature becomes less asymmetric when it falls below 5eV (dashed line in the right plot). While this behavior is not entirely clear yet, we observed that significant parallel currents can develop in the SOL when the asymmetries are present. These are well known thermoelectric currents [see e.g. G.M. Staebler and F.L. Hinton (1989) Nucl. Fusion 29 1820] and flow from the hot to the cold target, thus redistributing the power. These, however, cannot be the explanation of the asymmetries as the latter persist even when the currents are artificially turned off (the currents are a symptom of the asymmetries rather than their cause). The important take home message here is that the asymmetries do not prevent long outer connection length solutions to be acceptable and even beneficial. However, it is probably wise to avoid increasing the $L_{//,o}/L_{//,i}$ ratio significantly beyond 1, as in this case the geometric drive for the asymmetry might not be quenched by the radiation effect.

While we found that in/out asymmetries are not preventing a solution, in the DND case up/down asymmetries proved more problematic. The following figure shows that the heat flux flowing towards the upper divertor (UO and UI) is indeed mitigated when the Ar seeding level increases at fixed n_{sep} , but the situation reverses in the lower divertor (LO and LI). Similarly, the lower divertor temperature is unacceptably hot in the lower targets (both inner and outer) and only large seeding levels restore an acceptable situation (compare with Fig. 4).

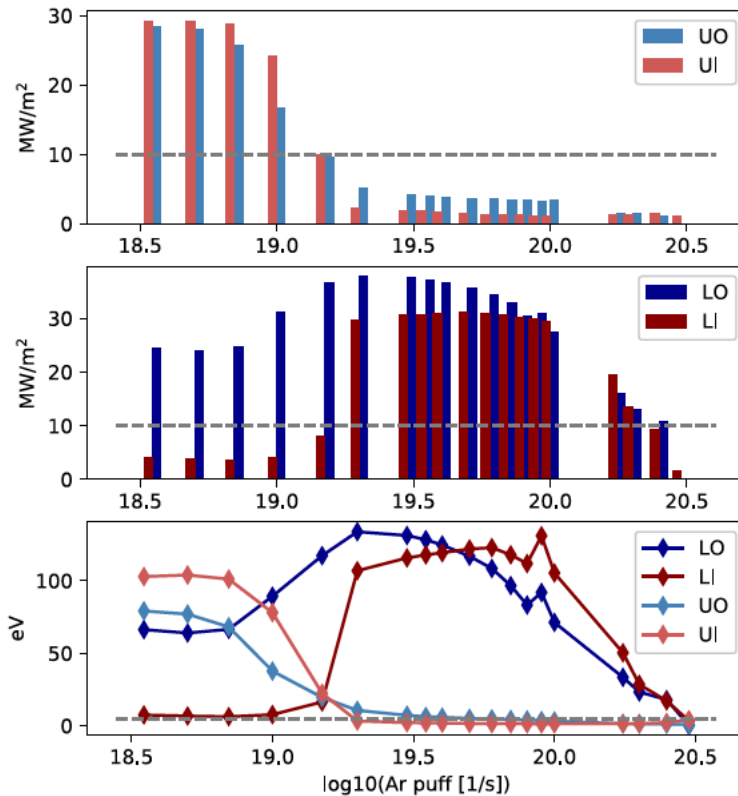


Figure 10: Heat flux reaching the upper and lower targets (top and middle panel respectively) as a function of the Ar seeding level. Peak temperature at the target (lower panel).

The interpretation of these results is that even small asymmetries in the initial magnetic configuration can lead to a feedback effect that can enhance the radiation in one divertor and reduce it in the other, so that intermediate seeding regimes display quite different conditions (the divertors in the DND are physically separated, differently from the single null solutions). This is a concerning observation because it might suggest that if seeding falls below a certain threshold (maybe transiently), it could trigger a strong asymmetry that can lead to large loads on one of the two divertors [see e.g. A S Kukushkin and S I Krasheninnikov 2019 Plasma Phys. Control. Fusion 61074001].

Also, even when the DND is in the acceptable operating space, no clear advantage with respect to the SND was observed in the simulations. The figure below shows that the impurity concentration (measured with Z_{eff}), the radiation fraction required to be in detached conditions, the neutral pressure in the PFR (a measure of pumping efficiency) and the He enrichment in the divertor (again measuring the efficiency of He pumping) are substantially comparable in both configurations.

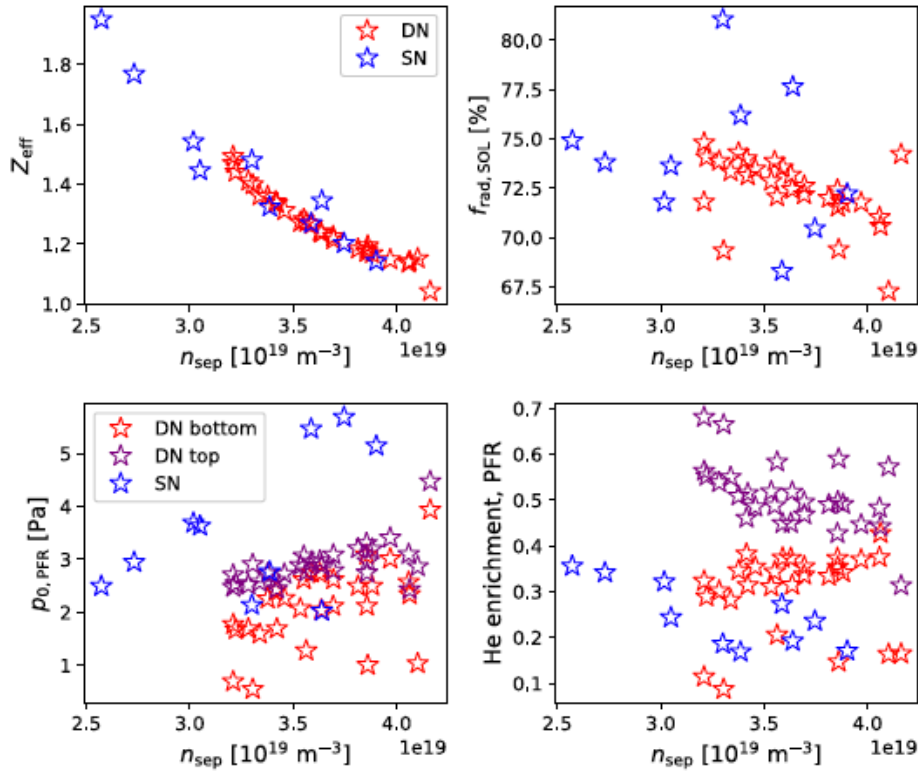


Figure 11: Parametric dependencies within the operating spaces. Shown are Z_{eff} (top left), $f_{\text{rad,SOL}}$ (top right), neutral pressure in the PFR (bottom left) and He enrichment in the PFR (bottom right) as a function of n_{sep} .

The results obtained so far do not seem to provide strong evidences to justify the use of the DND rather than the SND in DEMO, although more sophisticated modelling could possibly improve the DND performance (e.g. it is unclear what the response of the asymmetric behavior might be when drifts and kinetic modelling are considered).

As already mentioned, the SFD minus simulations performed did not lead to firm conclusions on the existence of an operating space. This might well be related with the fact that this configuration is numerically more challenging than the others, but it might also be indicative of some difficulties in the physics. It is worth noticing that SOLPS cannot perform perfect SFD simulations with a second order null, hence our decision to use a low field side SFD minus equilibrium with a midplane separatrix separation of 1 mm. As the figure below shows, the four strike points of this configuration are all active but with different plasma loads. In particular, SP4 (the outermost) has temperature of the order of 400eV and does not seem to significantly benefit from Ar or fueling increase. On the other hand, both the deuterium and Ar levels are much smaller than in the other configurations (higher values systematically lead to the code crashing).

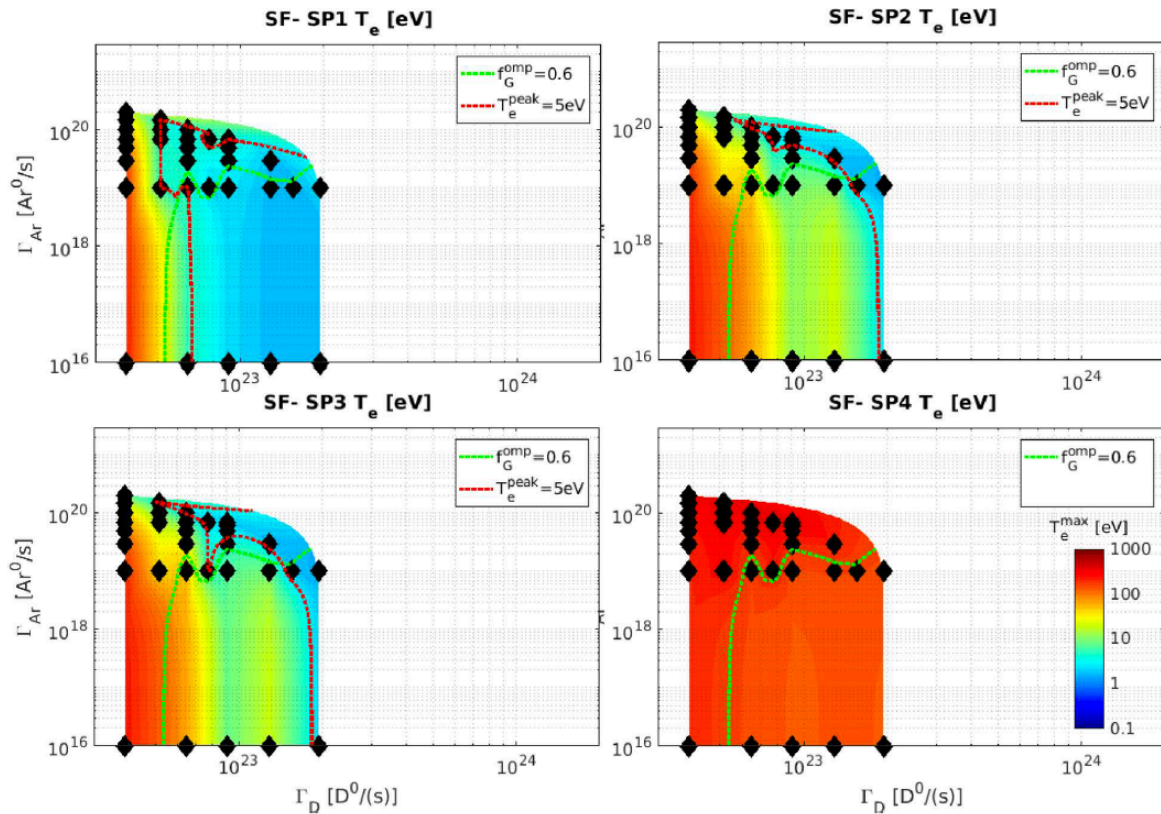


Figure 12: Response of the four strike points in the SFD minus configuration to variation of seeding and fuelling levels.

The behaviour of SP4 is not yet completely understood (its connection length is shorter than the SND's). The fact that the separation of the separatrixes was relatively small ($1/3$ of λ_q), might give room to better balance the power flowing to different strike points, so three other equilibria with 4mm, 10mm and 20mm separation were developed and are shown in the figure below:

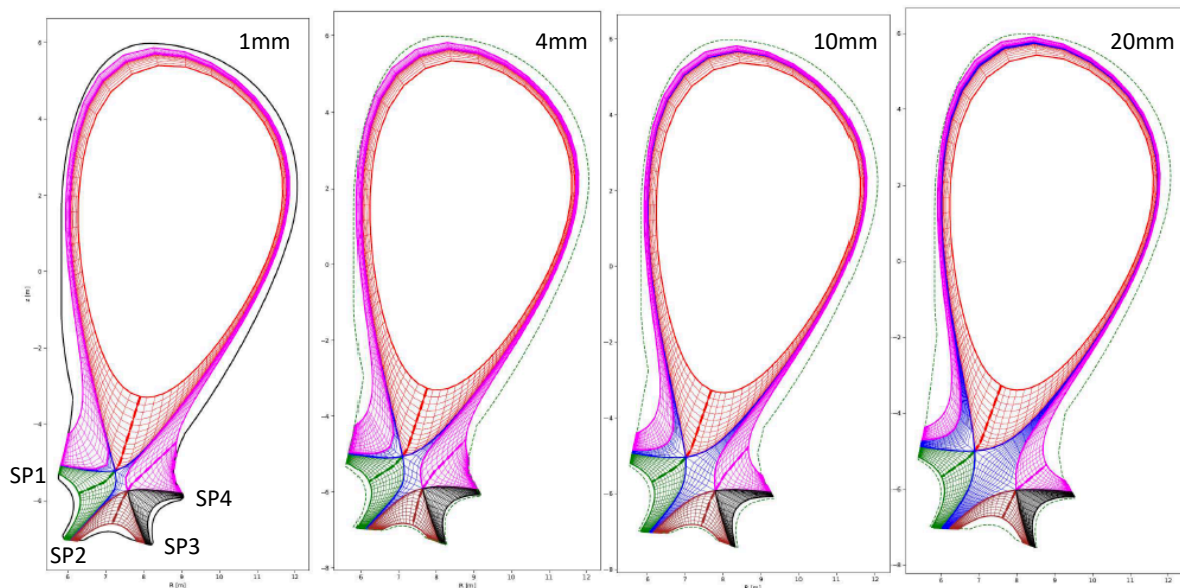


Figure 13: different SFD minus configurations with variable separatrix separation. The figure also shows the position of the four strike points.

Unfortunately, the 10mm simulations could not find an operating space either, since in this configuration SP1 and SP2 systematically remain above the acceptable wall load limit (but

SP4 is now within the threshold). At the moment of writing, no acceptable solution has been found for the SFD minus. If this exists, however, it is expected to be only in the range between 1mm and 10mm, which is narrow.

Finally, it is interesting to notice that we systematically found in all configurations that an increase of the seeding level at constant fuelling level reduced the separatrix density. This was observed also in more sophisticated kinetic simulations for ITER [], so it is likely to be a feature of highly radiating regimes. The explanation for this phenomenon is based on the reduction of the power available to ionization and a consequent decrease of the ionization sources. This is well exemplified by the following figure obtained for the SXD:

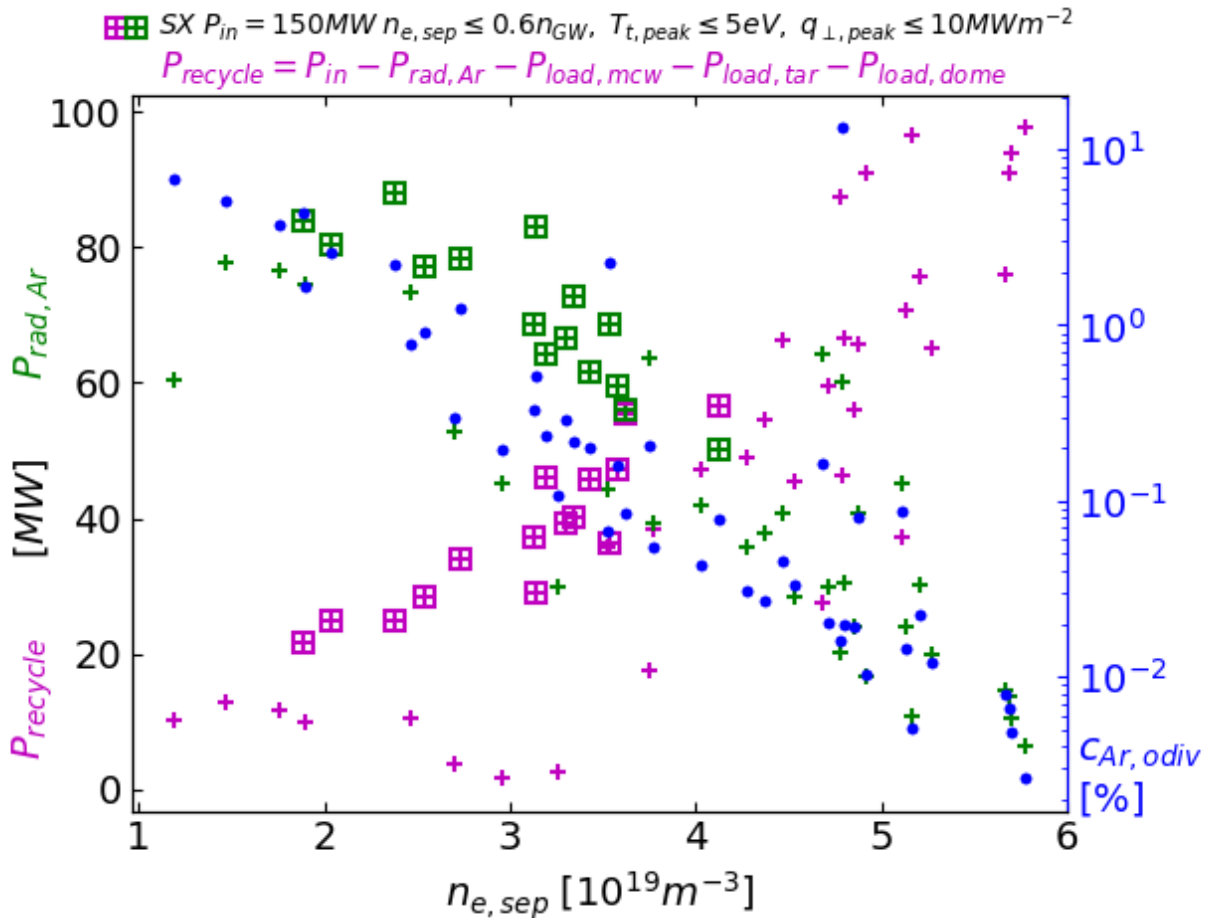


Figure 14: Power available for recycling, power radiated by Ar impurities and Ar concentration in the outer divertor as a function of the separatrix density.

Here $P_{recycle}$ is the power available for ionizing the recycled particles and it is given by the power arriving from the core minus the power transferred to the impurity and then radiated and the power reaching the walls. We see that when the separatrix density scales linearly with the power available for ionization and that the latter is larger when the power going into radiation is smaller. Finally, the figure shows that the radiated power is well correlated with the Ar concentration in the outer divertor, thus giving a quite compelling and complete picture.

3.2 Turbulence calculations

One of the biggest unknowns in exhaust physics is the role of perpendicular transport in affecting detachment and wall loads. The multifluid codes, and SOLPS is no exception, assume constant diffusion coefficients, which are extracted from experimental fits when the simulation is interpretative, but are arbitrary in predictive runs. While it is difficult to guess the coefficients in single null conditions (often one adjust the coefficient until the desired SOL width is obtained) it might be risky to do so in a comparison between ADCs.

In this project we started by assuming that all the configurations had the same heat flux decay length of 3mm and adjusted the diffusivity in order to get this (it required rescaling ITER's coefficients, as explained in Appendix I). However, this does not ensure that for a given seeding and fueling level λ_q will be comparable in all the configurations investigated. In this respect, the study presented here is a comparison between divertor design *assuming the same heat flux decay length*, which therefore only provides a partial answer. An often-used approach is to carry out sensitivity studies to assess how important are variations of the transport parameters on the final results. We could not carry these out due to lack of time, but they are highly recommended for the future.

Our approach was slightly different and aimed at having a more self-consistent answer. In particular, first principle simulations of SOL turbulence have been carried out for all the configurations investigated and, once fully converged, they could give indications on the relative importance of the perpendicular transport in each configuration as well as the poloidal distribution of the diffusion coefficients (typically the poloidal dependence is ignored in multifluid calculations, but it could be significant in long connection length ADCs).

Unfortunately, none of the codes involved in the study (GRILLIX, GBS, TOKAM3X, STORM) has the capability to carry out a 3D full geometry DEMO simulation. This is a severe limitation for the exhaust programme generally speaking, especially in the perspective of reliable reactor design and it should be addressed seriously at a EUROfusion level with a concerted and organized effort (it is unsure that any of the present-day turbulence codes will ever be able to carry out reactor relevant studies -which include thorough scans- including impurities and neutral physics). The only possibility left was to maintain the geometry of the machine but to scale it down in such a way that the normalized Larmor radius, ρ^* , was equivalent to TCV's. Larger simulations would lead to unacceptable losses in resolution or prohibitive computational costs. It is worth stressing that this is the best that current 3D fluid codes can provide at the moment. The table below discusses the feasibility of the 3D simulations with respect to different machines, operating modes and plasma parameters.

Table 3: Feasibility of 3D turbulence simulations (without neutrals) for different machines at different machine parameters.

	Machine ref	q_*	m_e / m_i	β	v_e	v_i
doable	TCV L	9.1E+02	2.7E-04	9.6E-05	4.3E+01	3.3E-01
	MAST-U L	4.2E+02	2.7E-04	3.2E-04	2.2E+01	1.9E-01
	MAST-U H	3.8E+02	2.7E-04	2.4E-04	1.0E+01	9.4E-02
expensive	CMOD L	2.5E+03	2.7E-04	7.5E-05	6.4E+01	7.5E-01
	CMOD H	2.5E+03	2.7E-04	1.3E-05	9.8E+00	1.2E-01
	AUG L	3.1E+03	2.7E-04	5.5E-05	3.8E+01	4.2E-01
	AUG H	3.0E+03	2.7E-04	7.2E-05	4.2E+01	4.8E-01
currently out of scope	JET L	5.9E+03	2.7E-04	2.9E-05	5.3E+01	5.5E-01
	JET H	4.7E+03	2.7E-04	8.7E-05	3.9E+01	5.2E-01
	ITER H	1.4E+04	2.2E-04	7.2E-05	7.4E+01	1.0E+00
	DEMO H	3.3E+04	2.2E-04	3.0E-05	1.6E+02	1.9E+00

Despite the limitations, the simulations presented here are the first to investigate 3D turbulence in ADCs worldwide (at the PL's knowledge) and this therefore marks a great success of the team.

The figure below shows the qualitative behavior of the turbulence in the four configurations investigated (SN, XD, SXD and SFD).

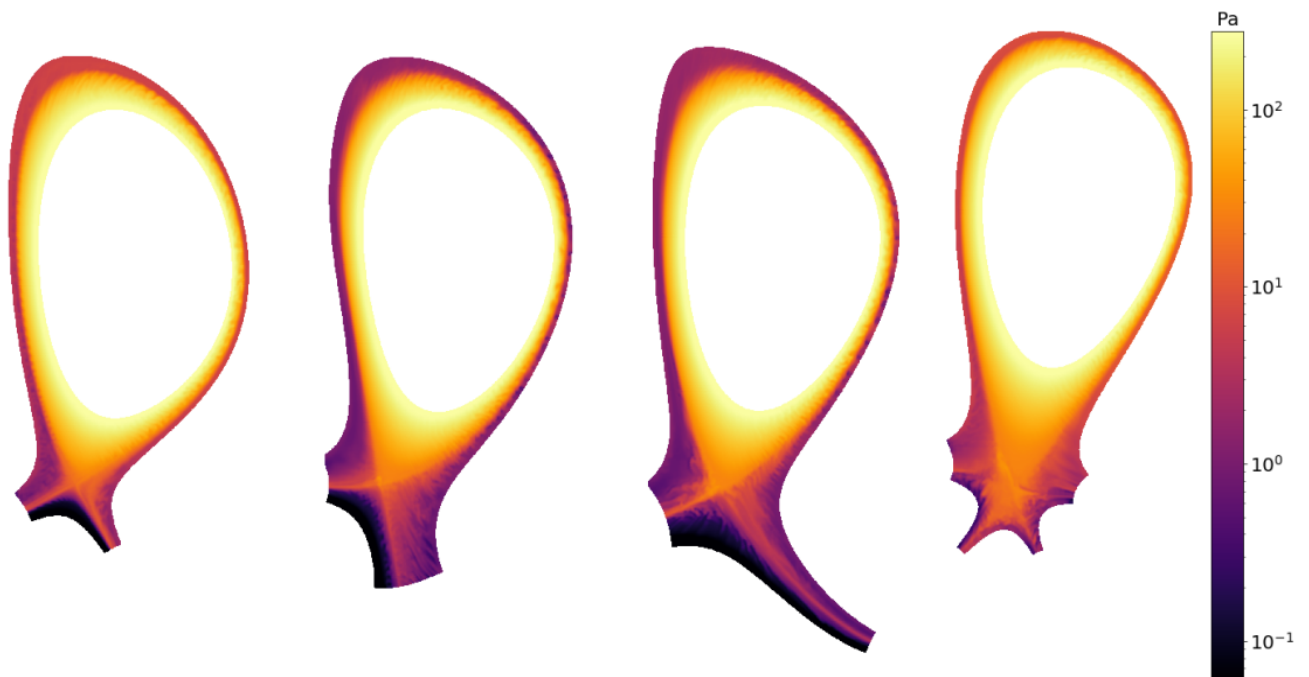


Figure 15: Snapshots of the pressure (in log scale) associated with the turbulent fluctuations for all the investigated configurations (Obtained with GRILLIX).

It is already evident that qualitative differences are present and, in particular, more prominent turbulent structures are visible in all the ADCs.

This is confirmed by closer analysis, which shows mushrooming structures in the PFR of the SFD. Also, investigations with GBS demonstrated that a turbulent electrostatic mode in the X-

point region can redistribute the power and the particles on all the SFD strike points, thus providing an effective mechanism to mitigate the loads on individual strike points [more details in M. Giacomini et al., Nucl. Fusion 60:024001 (2020)]. GBS analysis has shown that in analytic TCV like equilibria the convective cell associated with this mode is present and stronger than in SND configurations (possibly because of the weaker magnetic shear in the region). This could have repercussions on how the diffusion coefficients are fixed in multifluid simulations, if the existence of this phenomenon is confirmed for larger machines.

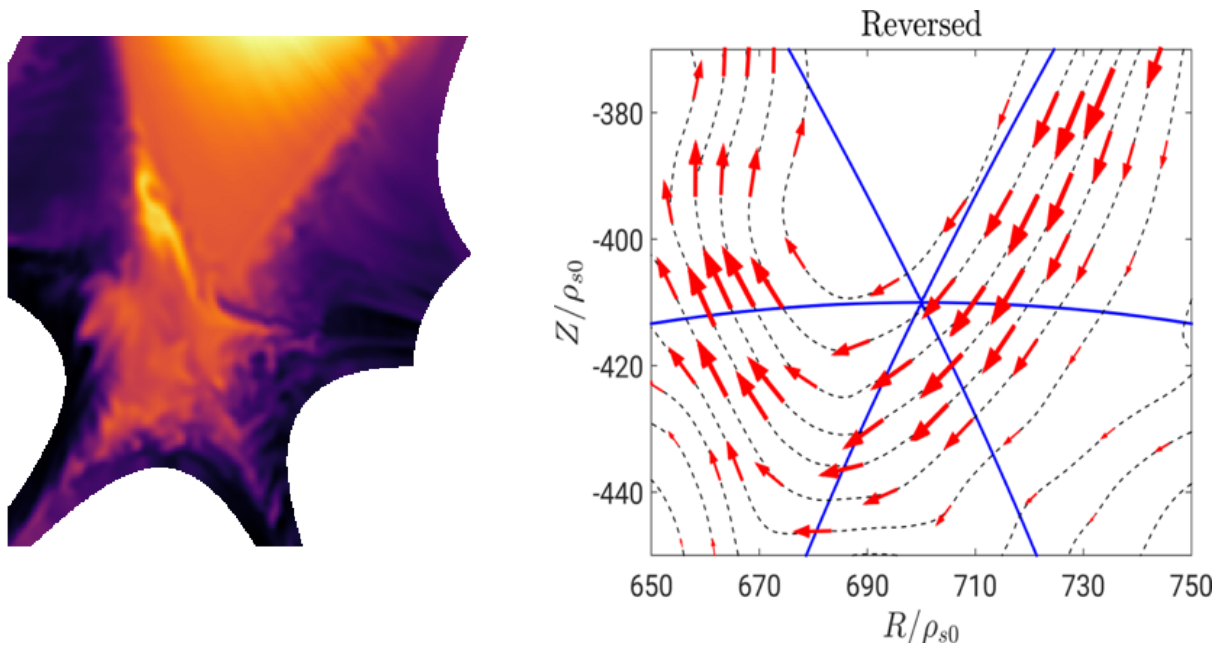


Figure 16: Left: mushrooming structures in the SFD X-point region (GRILLIX, DEMO geometry). Right: ExB flow pattern and convective cell in the X-point region of the analytic SFD equilibrium (GBS, TCV parameters).

As an aside, GBS has carried out a scan in the topology of the SFD, and compared it with the SND (again, with analytic equilibria and in TCV conditions). The result, presented in the figure below, shows that individual strike points receive less heat flux than SND case in the ideal or SFD plus cases but SP2 or SP3 can be quite loaded in the HFS and LFS SFD minus cases.

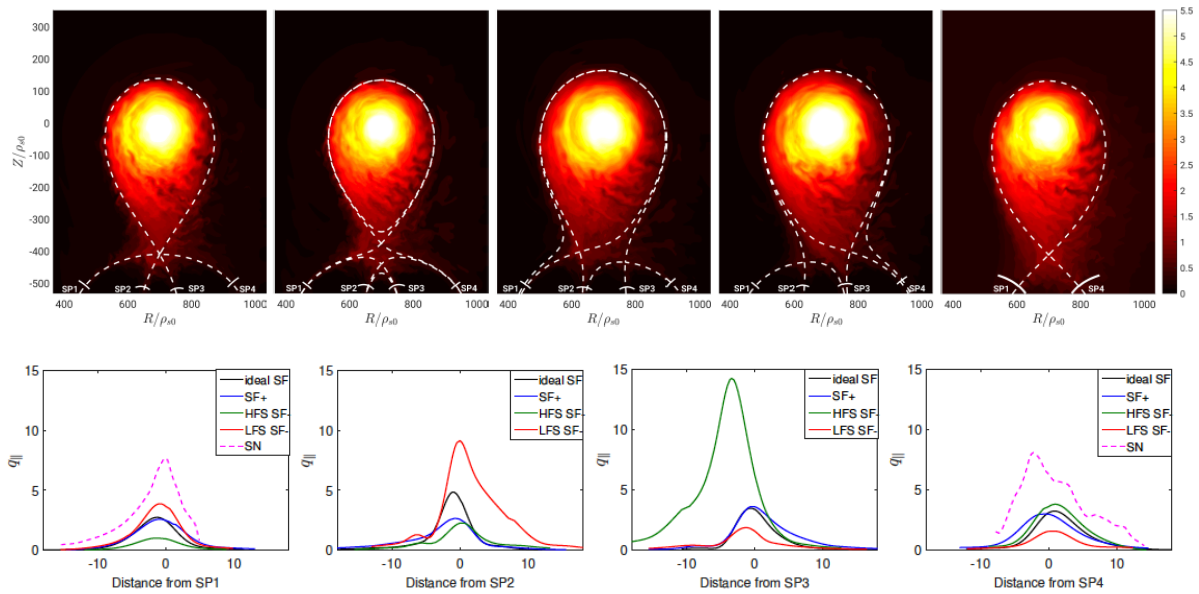


Figure 17: Scan in topology carried out with GBS. Ideal, SFD plus, SFD minus HFS, SFD minus LFS and SND are compared. In the lower row, the energy loads on individual strike points are displayed.

Obviously, these results would require further investigation in machines of larger scales and in different plasma regimes before their validity can be confirmed for DEMO or reactors, as they might rely on the existence of a sizable X-point convective cell.

The SXD also displays a peculiar behavior in the outer divertor leg region, where turbulent structures seem to be quite active. This might be due to the poloidal inclination of the leg and its length, which could remove stabilization mechanisms for divertor localized instabilities (see e.g. Walkden et al., 24th PSI, 2021). A more violent turbulence in the outer divertor leg could be beneficial as it would lead to easier detachment access and better spreading of the loads without affecting the upstream conditions and main wall erosion. Even though this phenomenon is not fully quantified, it seems to be reproducible with different codes and in slightly different geometries, as the figure below shows.

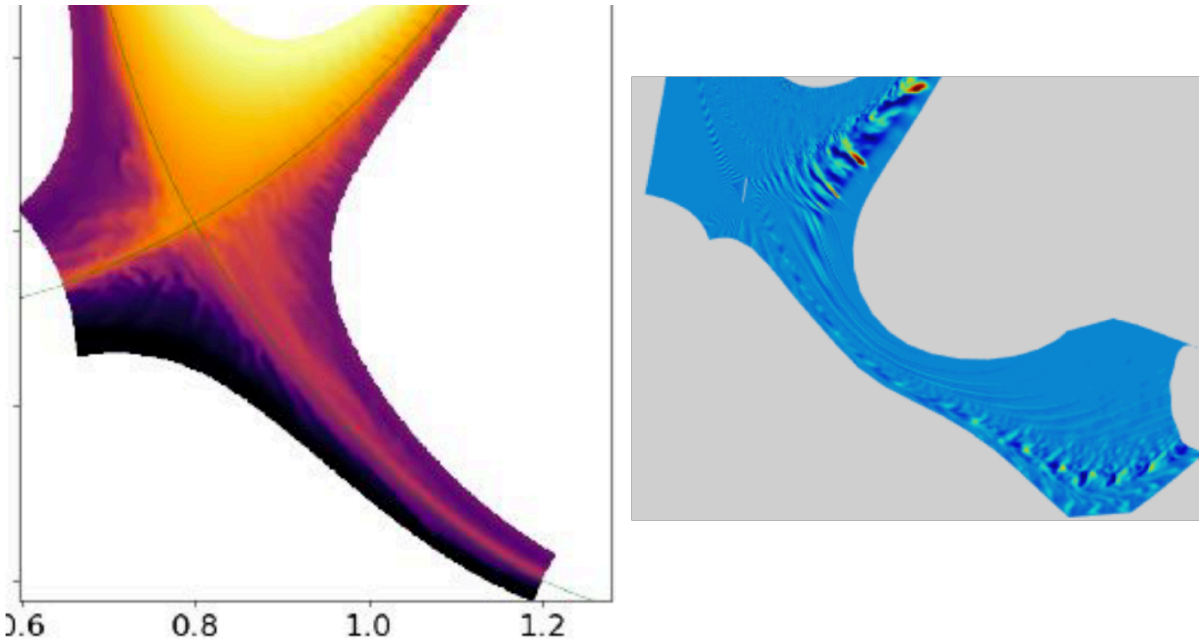


Figure 18: Zoom in the X-point region of the SXD for simulations of DEMO with Grillix (left) and MAST-U with STORM (right). Both figures show pressure, for Grillix the total, for STORM the perturbation (i.e. the equilibrium is removed).

Finally, the intermittency of the turbulence was investigated using the GRILLIX DEMO simulations. Clear differences between the turbulence patterns at the LFS target were visible and broader profiles were found for the ADCs than for the SND.

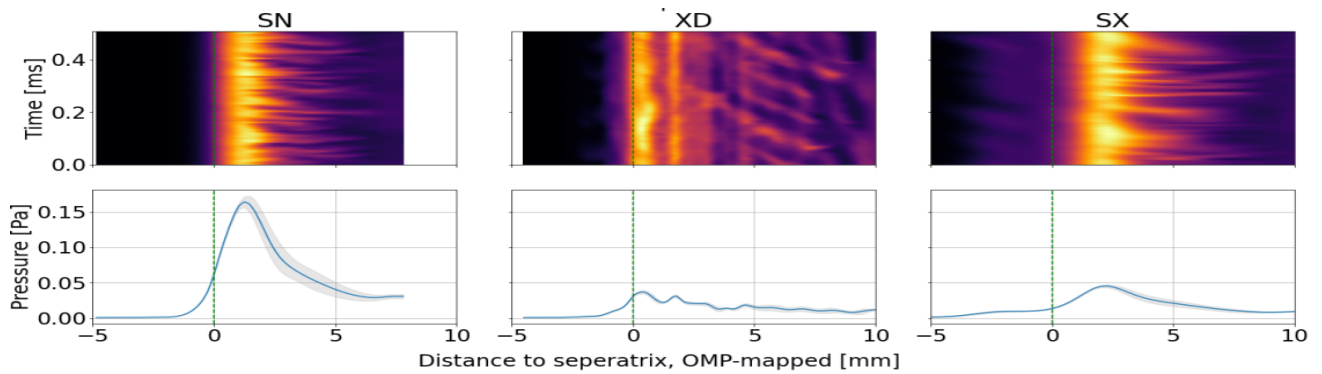


Figure 19: Pressure profiles at outboard target plate for SND (left), XD (centre) and SXD (right) configuration in dependence on distance to separatrix. Top row shows temporal evolution of pressure and bottom row averaged profile with its fluctuation level indicate by the grey area.

These simulations do not include neutral physics, which might change the results. This can also explain the discrepancies in pressure with respect to the multifluid calculations, which find target values of the order or 1-10Pa, much higher than those reported here.

To conclude this section, the simulations performed suggest that it is likely that SOL and divertor turbulence could be significantly different in ADCs than in SND. This, in turn could affect the properties of the divertor, in particular detachment access and stability as well as maximum heat loads tolerable and main wall loads. While the simulations carried out are only the first step in the right direction, it is emphasised that this physics mechanism should receive more attention in the future as it could be quite relevant (possibly we should use

larger D and χ in ADCs than in SND for a fair comparison). So far, all ADCs have shown broader profiles and stronger perpendicular transport than the SND, although it is unclear if these beneficial features will persist in larger scale simulations with neutrals included, and for the moment these studies seem to be behind the horizon.

4. Integration in the machine

As already mentioned in Section 2, the necessity to deform the toroidal field coils to accommodate the features of the ADCs has impactful consequences in several respects. In this Section, these repercussions are discussed. While different in their details, ADCs configurations (apart from the DND) tend to lead to the following modifications:

- 1) the TF coils are deformed from an ideal bend free D-shape to allow for the specific divertor and strike point features (larger poloidal or toroidal flux expansion or secondary null in the proximity of the main);
- 2) some PF coils move farther away from the plasma in order to remain outside the TF coils;
- 3) some PF coils need to be in inconvenient positions in order to provide beneficial ADCs features.

The degree of additional complexity in the TF and PF coils is dependent on the specific design, and while no general statement can be made, it is likely that the issues above will appear in most ADC configurations.

In the following subsections, we discuss how points 1)-3) reflect on the engineering of the machine. In particular, we will treat structural loads on the TF coils, control issues, feasibility of remote handling and finally neutronics studies. As usual and in the spirit of this project, all the calculations have to be intended as initial and still requiring refinements and optimization. In all cases, strict procedure aimed at a fair comparison were enforced.

4.1 Structural calculations of the TF coils

Finite elements structural calculations were carried out with ANSYS following a procedure analogous to that followed by PPPT's WP-MAG, with which WP-DTT1/ADC was regularly discussing. Unless otherwise specified, the procedure used for the calculations, as well as the approximation used was thoroughly documented in a specification document uploaded on IDM and that can be found on this link: <https://idm.euro-fusion.org/?uid=2NRTBE>. For the sake of brevity, we will not review all the specifications and focus on the results. However, it is worth mentioning a couple of important technical and methodological points before moving on.

Gravity loads were neglected, and the focus was on the effect of the electromagnetic (EM) loads. These can be divided into hoop forces, describing the expansion of a closed current carrying conductor, and out-of-plane forces, generated by the interaction between the TF coil current and the poloidal magnetic field induced by the PF coils. The hoop forces can be minimized by producing a constant tension design known as Princeton D-shape [R. Moses, W.C. Young, 6th Symposium on Engineering Problems in Fusion Research, (1975)]. Neither

the initial ADCs nor the SND design were optimized in this respect, and the shape of the TF coils had to be modified over time to be capable to withstand the EM forces.

The TF coil description consists of two bodies: the casing and the winding pack. The former is the primary structural component of the TF coil and houses the latter, responsible for carrying the currents that generate the toroidal field, within it. The interface between the winding pack and the casing allowed for sliding. Detailed calculations include the full description of the winding pack, including insulator and jackets, and while performed by WP-MAG for the baseline design, they were not carried out by WP-DTT1/ADC. Instead, the analysis was performed using a simplified winding pack geometry composed by six layers with smeared material properties meshed with hexahedral elements, while the case and the filler use tetrahedral elements to improve the contact behavior (a friction coefficient of 0.3 has been chosen between the casing and the filler, which can slide), see figure below.

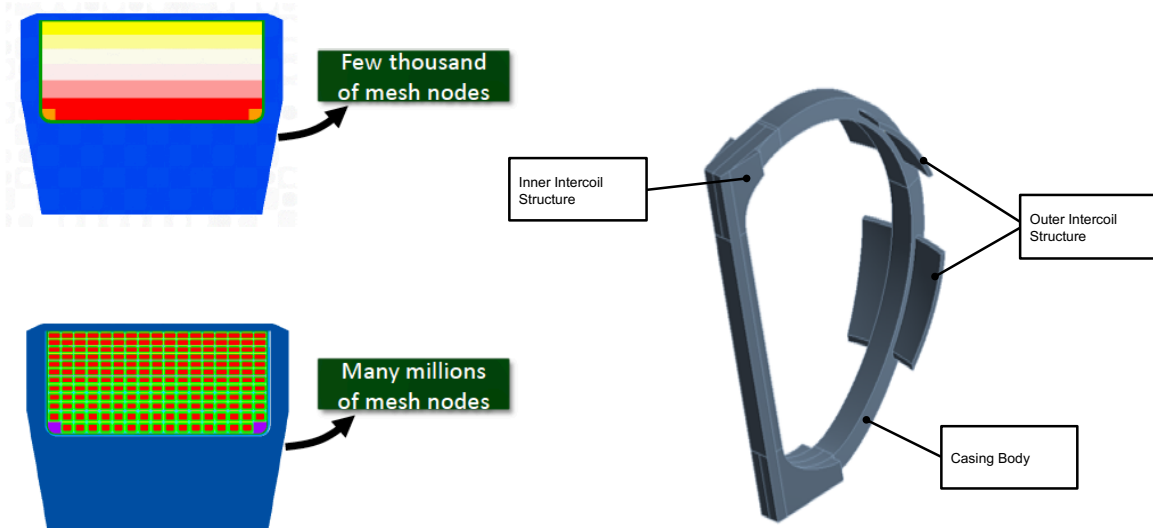


Figure 20: (left) cross section of the winding pack and smearing; (right) casing and intercoil structures.

In terms of failure mode and limits, stress linearization was used to assess the designs where the peak static stress intensity appears to be problematic [ITER report "Magnet Structural Design Criteria Part 1: Main Structural Components and Welds", (2012)]. The stress intensity calculated using NB-3113.1 in ITER report above was used in the analysis and compared against Tresca Yield Criterion. This is a stricter constraint than the more forgiving Von Mises criterion sometimes used in similar calculations. The allowable stress value, S_m , is set to 2/3 of the material's yield strength at a temperature of 4K, which is 1000 MPa for the EC1 strengthened austenitic steel we consider. According to the RCC-MRx rules:

- 1) the primary membrane stress, P_m , must be such that $P_m < \alpha S_m$;
- 2) the primary membrane plus bending stress, P_{mb} , must be such that $P_{mb} < 1.3 \alpha S_m$;
- 3) the primary membrane plus bending plus peak stress P_{mbp} , must be such that $P_{mbp} < 1.5 \alpha S_m$.

High and low field side parts of the TF coil have different limits, so that for the former $\alpha=1$ and for the latter $\alpha=3/4$, reflecting the fact that the inner section is forged and the outer cast. This results in:

Table 4: maximum acceptable stresses on HFS and LFS limbs depending on the criterion used.

	Maximum acceptable stress HFS limb (MPa)	Maximum acceptable stress LFS limb (MPa)
P_m	666.7	500.0
P_{mb}	866.7	650.0
P_{mbp}	1000.0	750.0

The linearization of the stresses took place along the worst-case path through the casing cross section, while avoiding artificial hotspots. The procedure was therefore akin to ITER's and WP-MAG (a remarkable difference is that the ITER limits are *less* stringent than the ones used here).

Moving now to the results of the analysis, we start with early calculations in order to demonstrate how the approach evolved over the years. In particular, we focus now on calculations performed in 2019 and based on the 2018 equilibria discussed in Section 2. A stress map for the different configurations is given in the figure below.

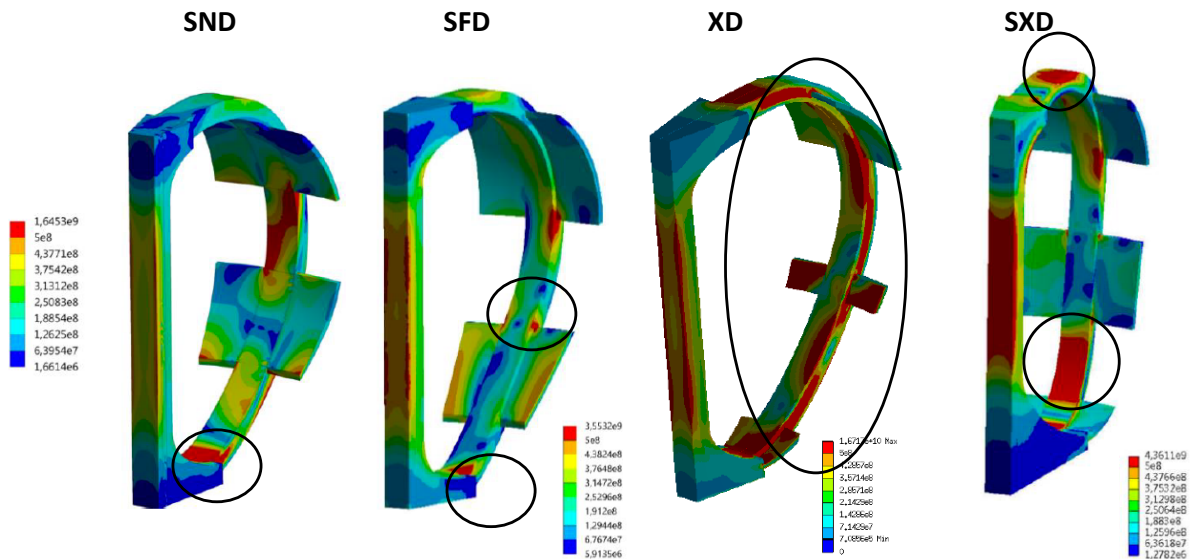


Figure 21: Stress map for the different 2018 configurations (in Pa). Note that the maximum of the colormap is based on the outer limb peak threshold of 500MPa, which is the most conservative limit. Hence several areas present acceptable stresses despite being red. The black ellipses identify areas where stresses are unacceptably high.

In all the calculations, the SND was used as a reference. It is important to remark that the baseline DEMO design is in a much more advanced design phase than the ADCs presented here. For the sake of comparison, we have therefore simplified the more refined SND DEMO engineering design to the level of our ADC configurations. With this in mind, our structural calculations, show stresses against cooldown (from ambient temperature to 4 K) and EM forces several tens of percent above threshold at the connection between inner and outer limb of the lower part of the TF coil. While these numbers are given to compare with our

current ADCs designs, these stresses are likely to be significantly reduced by more detailed engineering, and thus are not cause for concern.

For the SFD, we identified two issues where inner and outer segments meet and at the connection between the intercoil structures and the casing just below the equatorial port. In both cases, the stresses exceed one of the thresholds, but these conditions were less severe than for the SND, with the equatorial port failing only by a couple of percent, see Figure 21. These peaks appear at sharp corners, which could be smoothed with fillets in more refined designs, and thus only cause moderate concern. On the other hand, the current design is probably underestimating the stresses in the TF coil, since the intercoil structures used have an unacceptable poloidal extension. Indeed, a major issue for the SFD is the accessibility of the divertor region for installation and remote handling operations. More details will be given in Section 4.3 Remote Handling .

The preliminary structural calculations for the XD were performed considering a minimal poloidal extension for outer intercoil structures. The results suggested that a significant redesign was needed, as at the moment they show several difficulties. As shown in figure Figure 21, stresses in the outer limb of the TF coils exceed thresholds systematically and can sometimes be significantly above acceptable limits. This is largely due to the fact that port size was maximised in this configuration, leading to relatively short intercoil structures and a lack of support and rigidity. While the equatorial and lower ports could be reduced to increase the strength of this design, the upper port cannot be further shrunk because it already presents challenges in terms of safe extraction of the inner blanket structures, which would require complex kinematics. In addition to the fact that the upper port should not be enlarged to avoid weakening of the structure, there is no physical space due to the proximity of PF1 and PF2, so that blanket handling is difficult. These, however, seem to be issues connected with the current design rather than intrinsic to the XD configuration.

The need for the SXD to extend the outer divertor leg to major radii poses a challenge to coil design, as it implies a significant deviation from the TF D-shape (if one wants to use space efficiently and keep cost contained). Regions of sharp curvature in the lower part of the TF coil are problematic, with stresses just exceeding the threshold although only by a few percent. In the upper part of the coil, where the inner and outer limb connect, stresses are above the allowed value, but comparable to those found in the SND. As this is a preliminary design, we expect that more sophisticated engineering of the TF coil could improve the situation, although care must be taken on the intrinsic difficulties associated with the SXD.

Important observations emerged from the structural calculations. The forces acting on a current coil in a tokamak are of two kinds:

- 1) hoop forces which tend to expand the coil and are due to the magnetic pressure acting on it (like a pressurized container);
- 2) out of plane forces due to the interaction between the background magnetic field and the currents flowing in the coil to generate its field (for a TF coil the poloidal field generate by the PF coils interacts with the poloidal currents flowing in the winding pack.

The stresses resulting from the hoop force can be minimized by designing coils with a shape that is as bend free as possible. Having a constant tension and reducing the shear stresses can be achieved using the Princeton D-shape already discussed above [R. Moses, W.C. Young, 6th Symposium on Engineering Problems in Fusion Research, (1975)]. This is the tokamak equivalent of taking a circular cross section for a high-pressure canister. Due to the fact that the toroidal magnetic field decays as $1/R$, where R is the major radius of the tokamak, the coil is not circular but rather D shaped. This immediately shows why deviating from ideal designs leads to an increase of the stresses observed in our calculations, see also figure below for a comparison.

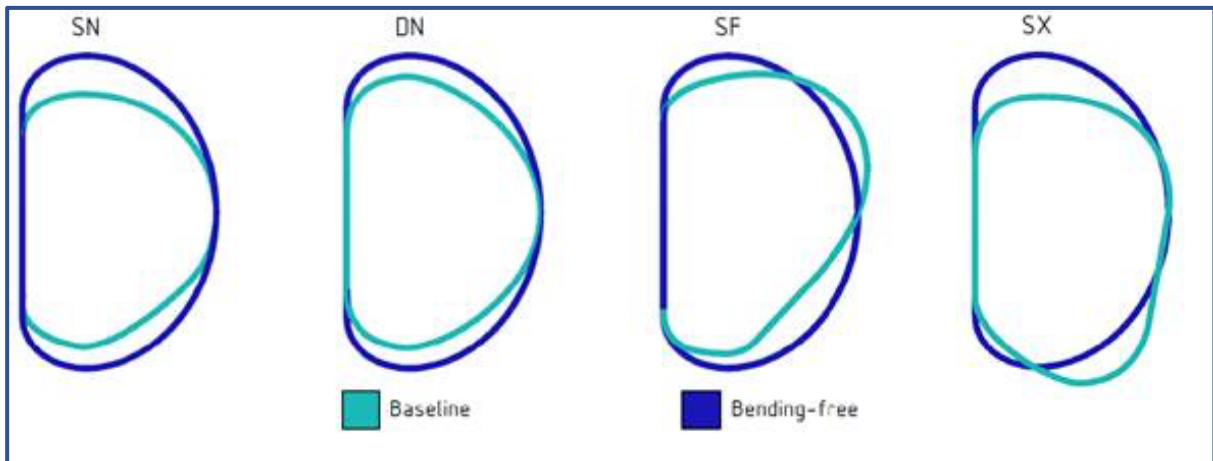


Figure 22: comparison between 2018 designs (including PPPT's SND) and an ideal bend free shape.

A back of the envelop calculation shows the severity of this problem. The magnetic pressure is given by $p=B^2/\mu_0 \sim 15\text{MPa}$, while tensile stresses on a coil of radius r and thickness t would give a minimum stress $\sigma=pr/t \sim 200\text{MPa}$ for current DEMO parameters (compare with the maximum acceptable values in Table 4).

Out of plane forces can have a significant impact on the total stress level, as shown in the figure below:

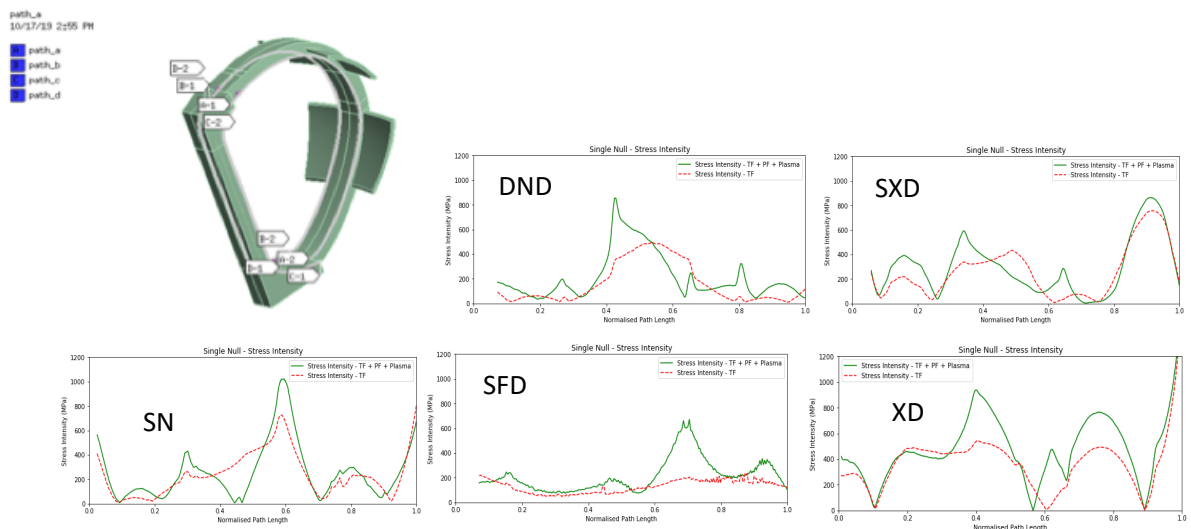


Figure 23: Stresses along a representative poloidal path in the TF coils of the different configurations with only hoop forces (dashed lines) and with full loads (solid lines).

Here, the dashed lines represent the stresses on a representative poloidal path in the coil due to the hoop forces only, while the solid lines include also the hoop forces. It is clear that locally the out of plane forces can be quite significant and can bring a solution beyond acceptable levels.

In order to make the design more resilient to both kinds of forces, two solutions were considered. The first, aimed at reducing the hoop forces, was implemented by F. Chiappa and C. Bachman of PPPT and consisted in using morphological transformations (mech morphing) that led to more D-shaped coils. Fundamentally, this led to an additional optimization criterion for the TF coil and generated a family of different coil designs. This method was incorporated into the WP-DTT1/ADC tools and various TF shapes were then analysed for the In-Plane loads using a beam solver. The second solution dealt with the out of plane forces, which tend to deform the coils outside their plane. Therefore, reinforcing the intercoil structures to provide more rigidity can help maintaining the stress level within limits. The solution proposed is to use an intercoil structure similar to the one employed by IDTT, which is based on a box design, see figure below:

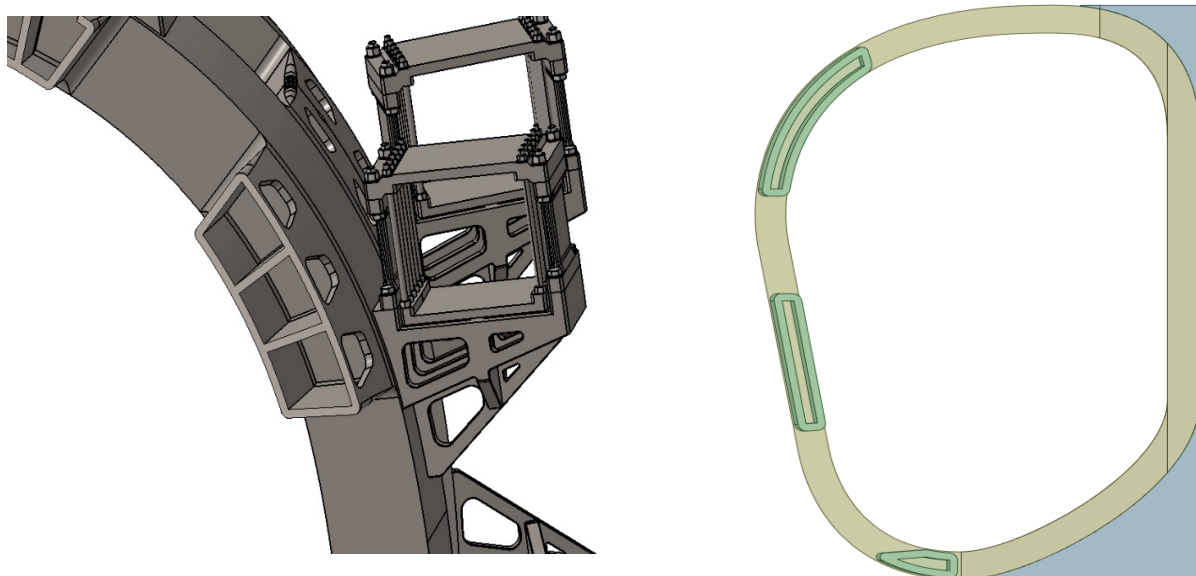
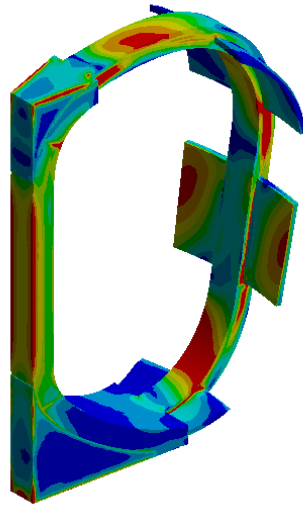


Figure 24: IDTT outer intercoil structures with the box design (left) and its application for the ADC SXD.

This design is based on structures that distribute load on a wider area and aims to avoid stress concentrations, as demonstrated by the figure below, which compares the simple and box intercoil structures:

B: SX RM Max
 Stress Intensity
 Type: Stress Intensity
 Unit: Pa
 Time: 2
 07/05/2020 16:05

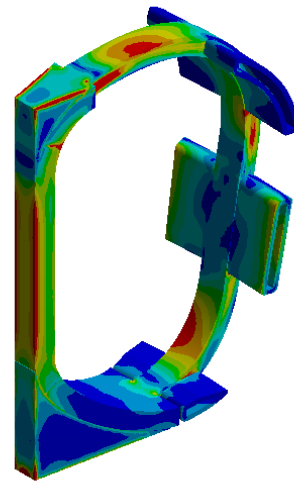
4.3165e9 Max
 6.6e8
 5.7766e8
 4.9533e8
 4.1299e8
 3.3065e8
 2.4831e8
 1.6598e8
 8.364e7
1.3025e6 Min



(a)

J: SX RM Max DTT like OIS
 Stress Intensity
 Type: Stress Intensity
 Unit: Pa
 Time: 2
 07/05/2020 15:59

4.5762e9 Max
 6.6e8
 5.7762e8
 4.9524e8
 4.1285e8
 3.3047e8
 2.4809e8
 1.6571e8
 8.3326e7
9.4456e5 Min



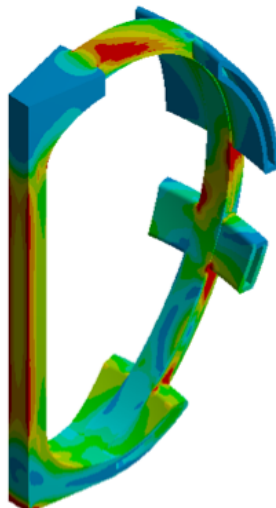
(b)

Figure 25: comparison of the stress maps with simple (left) and box (right) intercoil structures.

The stress is reduced in the majority of the areas of interest, however, the reduction in the upper port region is minimal, suggesting another solution is required to reduce the stress in this location. Combining the new intercoil design and the mesh morphing approach, a significant improvement with respect to the original 2018 designs is obtained. The full calculation was performed for the SFD and SXD and the associated stress maps are shown in the figure below.

W: sf idtt
 Equivalent Stress
 Type: Equivalent (von-Mises) Stress
 Unit: Pa
 Time: 2
 31/07/2020 16:05

1.5109e+10 Max
 5e8
 4.2857e8
 3.5714e8
 2.8571e8
 2.1429e8
 1.4286e8
 7.1429e7
1.0483e6 Min
 0



K: sx i-dtt m d
 Equivalent Stress 2
 Type: Equivalent (von-Mises) Stress
 Unit: Pa
 Time: 2
 31/07/2020 16:31

1.3361e+10 Max
 5e8
 4.2857e8
 3.5714e8
 2.8571e8
 2.1429e8
 1.4286e8
 7.1429e7
1.7919e6 Min
 Automatic

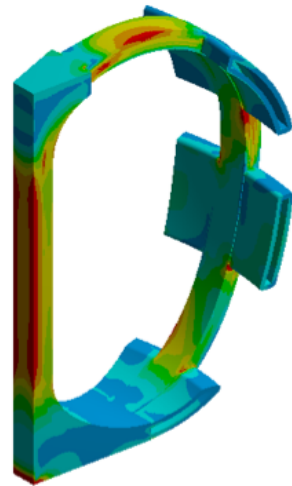


Figure 26: Stress map for the 2020 SFD (left) and 2020 SXD (right) once mesh morphing, box intercoil structures and Von Mises stresses are applied. With respect to the 2018 designs, the new ones shown here have also been modified to incorporate remote handling considerations.

The new 2020 designs shown above represent a visible improvement with respect to the 2018 ones shown in Figure 22. It is also worth mentioning that these coils have not yet undergone a thorough optimization and are still much less detailed than the baseline ones, so there might be potential for improvement (e.g. fillets, better intercoil structures,...) – but also negative surprises cannot be excluded. As we will see in Section 4.3, the 2020 designs shown here have been modified in order to take into account remote handling considerations and

are therefore more sophisticated than the 2018 ones. At any rate, the 2020 SFD is still unlikely to pass either the Stress Intensity or von Mises failure criteria (used by PPPT) due to the outboard through wall stress limit of 500MPa. The results for the 2020 SFD are better than for the SFD and it may pass the von Mises failure criteria when the stress is linearised through the wall (as per the ADC analysis specification). However, for a conceptual design using simplified geometry, passing a linearised stress criteria for the von Mises and failing Stress Intensity will likely create challenges further down the design process. Hence, while visible improvement has been achieved, a robust solution is not yet at hand and more work will be needed on the engineering side.

To conclude, we need to discuss two technical but important points: convergence of the simulations and boundary conditions. For the former, a number of tests were carried out, which showed that the stress state is indeed converged with respect to mesh refinements. The total number of finite elements, globally, but also in the winding pack and in the casing separately. The electromagnetic loads applied to the winding pack were calculated using the code Nova. Nova solves the Grad-Shafranov equation for a discrete number of filaments representing the plasma, PF, CS and TF coils. The number of filaments required to model the electromagnetic forces was investigated by comparing the stress intensity at 3 paths in the plasma facing surface of the casing, and an optimal solution was thus identified.

In the analyses presented above, the boundary conditions for the TF coils simulated the periodic behavior between individual elements. In reality, the inner leg of the TF coils (the “nose”) can slide with respect to each other and we carried out a series of stress analyses allowing for the possibility of separation. Indeed, the ITER Magnet Structural Design Criteria demonstrates the impact of such a sliding contact and the separation which follows. However, our results show that the differences between the two approaches are small, as far as equivalent stresses are concerned, thus giving us confidence in our simplified approach. The figure below shows the stress intensity along a path around the coil, comparing the case with and without “nose” sliding.

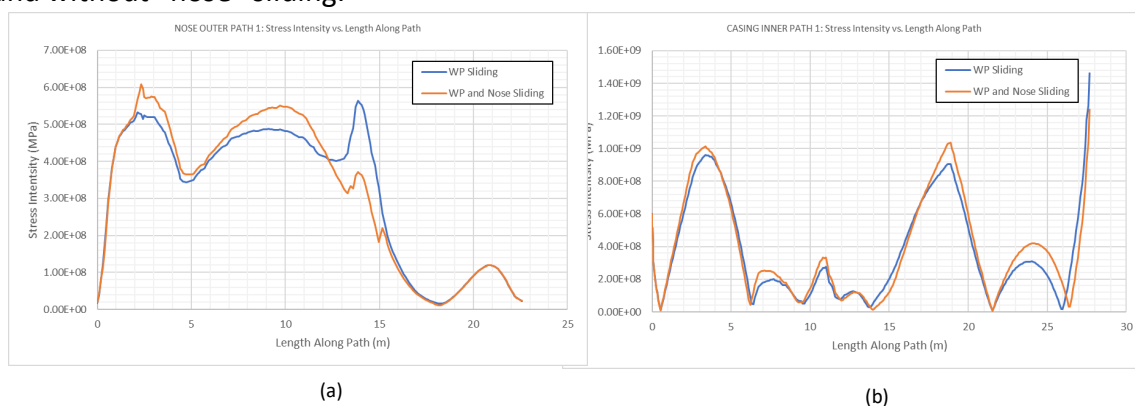


Figure 27: Stress intensity along a poloidal path inside the HFS (left) and LFS (right) limb of the TF coil. In all the cases presented so far, the winding pack slides but the “nose” does not (blue curve). Results with also the “nose” sliding are in red.

These results show that while a difference is present in the HFS part of the coil, it is not such that the simplified results qualitatively change. Therefore, it is recommended that when a design is shown to achieve the stress criteria without nose sliding method, it should then be re-assessed with nose sliding. Also, introduction of a gravity support is recommended when

a solution appears to be available because this might lead to additional stresses especially in the presence of nose sliding.

4.2 Control

We move now to the controllability of the plasma with respect to vertical displacements and also the capability of the control system to recover from unwanted displacements. The analysis is based on two major concepts. First, a diverted plasma is naturally prone to vertical instabilities, which tend to move the whole confined region due to the attraction between the plasma current and the PF coils currents. The growth rate of this instability therefore needs to be evaluated and compared between the different configurations. Second, assuming that the plasma centroid has already been displaced for some reason (a number of plasma phenomena can do this, from L-H and H-L transition to minor disruptions to ELMs), it is important to evaluate how much power the control system would require to bring the plasma back in its original place. The problem is therefore divided into a passive and an active controllability of the different configurations.

The analyses were carried out in three different phases of the plasma discharge, loosely representing the flat top (FT) discussed in Section 2, an increased l_i flat top (FT_li1) and the start of ramp down (SRD). These are the parameters used:

1. Flat top with reference plasma parameters ($I_{pl} = 19.07MA$, $\beta_p = 1.141$, $l_i = 0.8$)
2. Flat top with high l_i ($I_{pl} = 19.07MA$, $\beta_p = 1.141$, $l_i = 1$)
3. Start of Ramp Down ($I_{pl} = 19.07MA$, $\beta_p = 0.1$, $l_i = 1$)

The SRD is the most critical part of the scenario for the vertical stability performance, characterized by high internal inductance ($l_i = 1$), low poloidal beta ($\beta_{pol} = 0.1$), assuming full plasma current and flat top plasma nominal elongation. The analysis shows that all ADCs have growth rates and stability margins comparable to the SND, see table below:

Table 5: Comparison of the growth rate and stability margin for all the ADC configurations.

Configurations	Scenario snapshot	γ [s^{-1}]	m_s
SN	FT	2.3	0.65
	FT_li1	4.2	0.66
	SRD	6.3	0.46
DN	FT	6.24	0.4
	FT_li1	5.84	0.48
	SRD	14.27	0.24
SX	FT	2.11	0.64
	FT_li1	4.04	0.59
	SRD	7.3	0.34
XD	FT	1.66	0.97
	FT_li1	3.75	0.66
	SRD	6.73	0.4
SF	FT	1.73	1.1
	FT_li1	3.12	0.77
	SRD	5.36	0.51

Note that the DND is the only configuration to have a relatively larger growth rate due to the larger distance between the plasma and the passive stabilizing structures due to the double divertor. The numbers presented above show that the passive stability of the ADCs is not a cause of major concerns.

On the other hand, ADCs are much more sensitive to the SND to changes in the equilibrium configuration, leading to displacements of the plasma centroid that are significant. The figure below shows the impact of an arbitrary change of l_i and β poloidal:

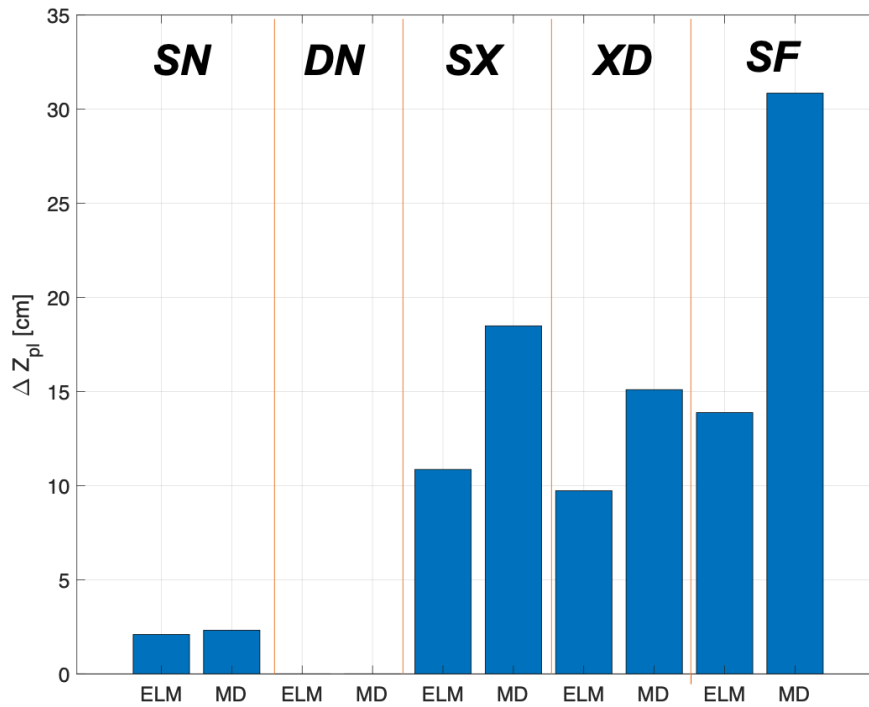


Figure 28: vertical displacement of the plasma centroid for the different configurations in the 2018 configuration. The definition of the "ELM" and "MD" displacement are given in the main text.

While it is still unclear which kind of macroscopic perturbations could affect the plasma, its stability was probed using two different variations of the equilibrium parameters: "ELM" was associated with $\Delta I_i = 0.1$ and $\Delta \beta_{pol} = -0.1$ and "MD" with a $\Delta I_i = -0.1$ and $\Delta \beta_{pol} = -0.1$. In both cases, these variations correspond to roughly 10% of the equilibrium values. While no precise physics meaning should be attached to these perturbations, they loosely represent a big ELM and a minor disruption.

The perturbations affect the global shape of the plasma, not just its centroid. This results in movements of the strike points and a change in the plasma wall gap that is sometimes pretty large. This is quantified by the table below, which describes how much the plasma moves in different places.

Table 6: displacement of different positions due to the ELM and MD perturbations for the 2018 configurations.

	Top of the plasma [cm]	Equatorial plane [cm]	Plasma current centroid [cm]	Xpoint [cm]	Inner leg at targer [cm]	Outer leg at targer [cm]
SN	2	12	2	9	17	18
DN	--	13	--	8	15	18
SX	25	16	18	25	34	42
XD	12	14	15	26	25	39
SF	18	16	30	--	--	--

The shape of the plasma is therefore significantly affected in the different configurations, but not all of them in the same way. For example, the biggest concern for the SXD is the motion of the plasma closer to the upper wall, which might induce a local increase of loads. The

motion of the strike points is less concerning due to the large size of the SXD divertor, which can be designed to accommodate these excursions. For the XD the situation is better because the shape modifications in the upper part of the plasma are comparable with the SND and the strike point variation remains within the divertor target, potentially also providing a positive sweeping effect. The SFD, however, proves to be very difficult to control due to very large variations in the position of the plasma centroid (the SFD is naturally more elongated than the other configurations) and the topological variations at the X-point shown in the figure below:

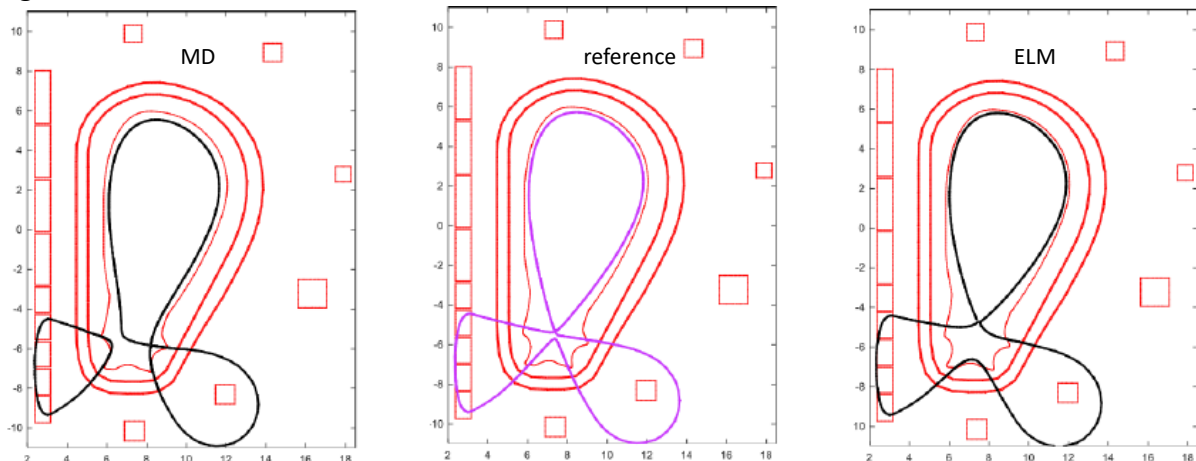


Figure 29: shape and topological variations for the 2018 SFD configuration due to ELM and MD perturbations.

The figure shows that the strike points of the SFD have significant displacements and a redesign of the divertor would be needed to accommodate them. What is more concerning, though is the fact that this configuration heavily relies on a precise topological configuration and this is easily destroyed by equilibrium modifications. While the ideal SFD is never going to be possible, it is expected that the equilibrium will be in either a SFD plus or minus configuration. But also in this case, small variations might lead to sudden loads on one of the strike points, as the modelling presented in Section 3.1 seems to suggest. The level of precision required in the alignment can be quantified by the size of the heat flux channel, which is of the order of 1mm-5mm at the outer midplane, and therefore present severe challenges in a 9m device. Similar, if not identical, consideration apply to the DND, which needs to maintain a distance between the separatrixes below λ_q in order to efficiently redistribute the power. While quasi up/down symmetric, and therefore less subject to vertical centroid displacements, the DND is actually quite sensitive to perturbations that are not up/down symmetric (not considered here, but it is recommended that this assessment is done in the near future).

In general, what the SFD and DND share is the fact that these concepts rely on a secondary X-point that has to be rather precisely positioned and controlled in order to provide benefits. This induces an additional control parameter, and one that is very sensitive by its own nature. While SFD plus solutions might be more resilient than SFD minus in this respect, care should be placed in ensuring that topological variations such as the one shown in Figure 29 never occur during operations, which might be a significant element of risk. Overall, the viability of the configurations that require on secondary nulls is probably linked to their precise and reliable controllability.

Moving back to the centroid displacements, it is evident from Figure 28 that the displacements associated with the ADCs is quite large and much bigger than for the SND. The reason for this is twofold: the external control coils are further away from the plasma due to the ADC TF coil deformations and the non-optimized passive stabilizing structures are less effective as they too are farther away. Before discussing possible ways of mitigating these problems, it is appropriate to assess whether these displacements could be handled by a control system.

Active stabilization was initially designed with stringent and conservative constraints:

- 1) It employed only two existing external coils (P3 and P4) for the SFD and XD while four (P2, P3, P4 and P5) for the SND, SXD and DND;
- 2) The voltage required to return the plasma to its original state was assumed to be 10 times larger than the minimum voltage V_0 that can stop at $t \rightarrow \infty$ the vertical instability resulting from the assumed displacement;
- 3) The displacement was instantaneous, and the control system started acting only when it reached its nominal value;

As a rule of thumb, the power request associated with $5V_0$ is a good estimation of the real power request given by a feedback vertical control system while that associated with $10V_0$ defines the upper bound for real power request. In addition, for the SXD, SFD and XD configurations the circuits are not optimized due to the asymmetry in the positions of the PF coils.

These resulted in very large power requests for the control system, which are detailed below:

Table 7: Power required to bring back a displaced plasma depending on the configuration, discharge phase and amount of displacement. These calculations were done for the 2018 configurations with only external coils (P2-P4 for the SND, SXD and DND and P3,P4 for the others) and a voltage 10 times the minimum required to stabilize a perturbation at $t \rightarrow \infty$.

Configurations	Scenario snapshot	Power request [MW] VDE 5cm	Power request [MW] VDE 10cm	Power request [MW] VDE 15cm
SN	FT	30.31	121.25	272.81
	FT_li1	114.72	458.9	>1000
	SRD	342.27	>1000	>1000
DN	FT	205.44	821.74	>1000
	FT_li1	172.02	688.06	>1000
	SRD	>1000	>1000	>1000
SX	FT	44.99	179.97	404.93
	FT_li1	187.89	751.55	>1000
	SRD	975.84	>1000	>1000
XD	FT	57.11	228.43	513.98
	FT_li1	315.95	>1000	>1000
	SRD	>1000	>1000	>1000
SF	FT	124.45	497.81	>1000
	FT_li1	345.02	>1000	>1000
	SRD	>1000	>1000	>1000

These power requests are very large for the SND and clearly unmanageable for the ADCs, especially considering the high sensitivity of these configurations. Also, it is worth noticing that the SRD phase is by far the most critical in all cases.

In order to mitigate the control problem three different solutions were investigated:

- 1) Optimization of the PF coil position to reduce the distance between the plasma centroid and the magnetic axis (balancing);
- 2) Introduction of stabilizing plates;
- 3) Addition of internal PF coils for vertical stabilization.

Here an example showing the modifications for the SXD is presented:

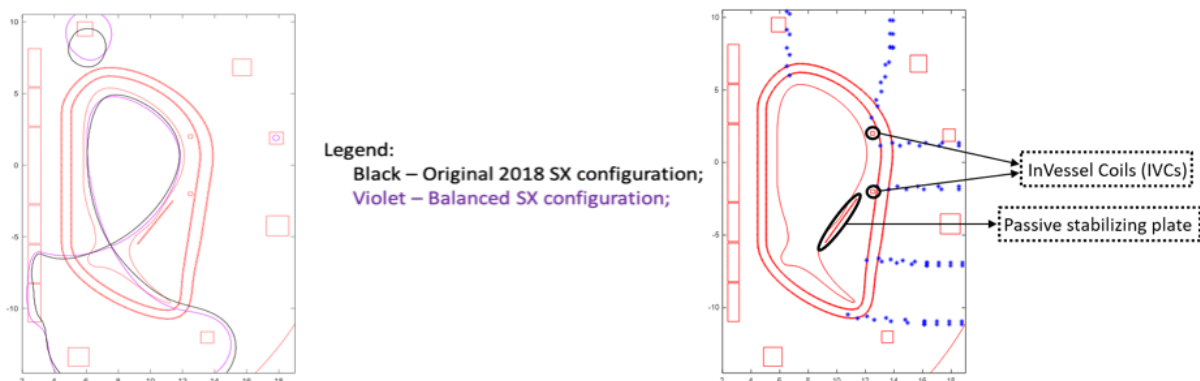


Figure 30: Solutions to improve the controllability of the solutions. Balancing the equilibrium (left) or adding internal coils and stabilizing plates (right)

The first solution was already carried out for the 2018 SND configuration, but not for the ADCs. Both the internal coils and the stabilizing plates add engineering complexity and necessarily come at a cost. It is neither trivial nor obviously possible to operate with internal coils in a reactor environment and space should be traded with other machine critical

components such as the blanket (note, for example, that the designs presented here are preliminary and the stabilizing plate is encroaching the breeding blanket, which will need to be fixed in a later stage of the design – here the stabilizing plate is introduced as a proof of principle analysis).

The balancing of the SXD was only partially successful with a reduction of the centroid/axis distance from 13cm to 9cm. With balancing (for the SXD and XD) and stabilizing plates, the passive stability of the ADCs improves, as shown in the following table (compare with Table 5):

Table 8: Comparison of the growth rate and stability margin for the balanced ADC configurations with and without stabilizing plates.

Configurations	Scenario snapshot	2019 Without stabilizing plate		With stabilizing plate	
		γ [s^{-1}]	m_s	γ [s^{-1}]	m_s
SXD	FT	2.11	0.64	1.93	1.25
	FT_li1	4.04	0.59	2.01	1.19
	SRD	7.3	0.34	4.17	0.75
XD	FT	1.66	0.97	1.46	1.30
	FT_li1	3.75	0.66	1.16	1.44
	SRD	6.73	0.4	3.33	0.77
SFD	FT	1.73	1.1	1.16	1.39

A small improvement is observed, but the problem was already marginally important to begin with. The vertical displacement during an ELM or MD perturbation, however, significantly improves with stabilizing plates for the SXD (~65% reduction) and the XD (~35% reduction), while it remains problematic for the SFD (~25% reduction and starting from higher values):

Table 9: effect of balancing and stabilizing plates on vertical centroid position for different configurations and perturbations applied.

Configuration	ΔZ_0 [cm] Without stability plates	ΔZ_0 [cm] With stability plates and shape optimization	Perturbation applied
SXD	11	4	ELM
	-18	-7	MD
XD	10	6	ELM
	-15	-11	MD
SFD	14	10	ELM
	-30	-23	MD

The associated power required to recover from the displacement has changed as well, also because the control circuit for the ADCs was also improved and now includes four PF coils (P2, P3, P4 and P5) rather than just two (compare with Table 7).

Table 10: Power required to bring back a displaced plasma depending on the configuration, discharge phase and amount of displacement. These calculations were done for the 2020 port compatible configurations (apart from the SXD that was in the mesh morphed configuration) with only external coils (P2-P4) and a voltage 10 times the minimum required to stabilize a perturbation at $t \rightarrow \infty$.

Configuration	Scenario snapshot	Power request [MW] VDE 5cm (With SP/without SP)	Power request [MW] VDE 10cm (With SP/without SP)	Power request [MW] VDE 15cm (With SP/without SP)
SXD	FT	126/196	505/783	>1000
	FT_li1	195/345	780/>1000	>1000
	SRD	914/>1000	>1000	>1000
XD	FT	38/45	152/180	342/407
	FT_li1	32/38	129/154	291/348
	SRD	278/362	>1000	>1000
SFD	FT	25/26	100/105	226/237

While the figures for the power are now significantly lower and closer to the original SND for both the XD and SFD, one has to remember that the ADCs are more susceptible to perturbations than the SND. Overall, however, the improvement was visible. For the SXD the situation is actually worse than before, and the reason is that the TF coils become bigger due to the mesh morphing optimization. Some of the PF coils had to be moved by $\sim 0.5\text{m}$ and this degraded the coupling of the control system with the plasma, see figure below:

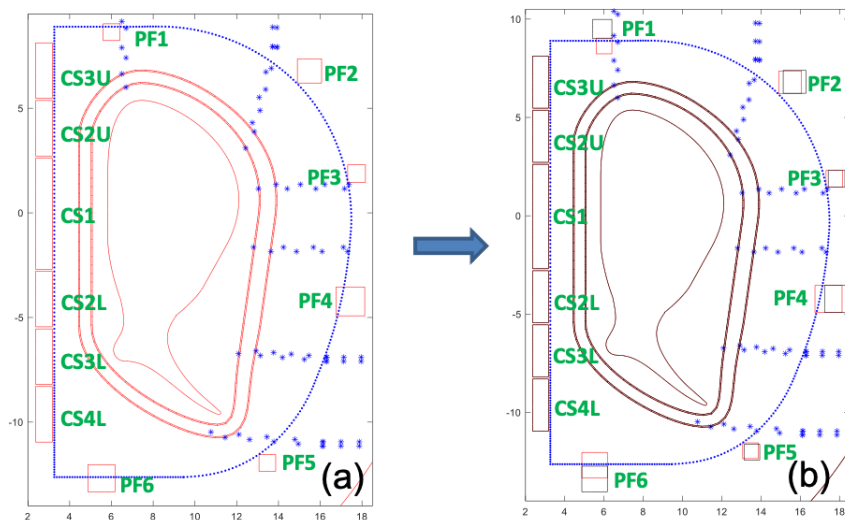


Figure 31: (left) 2018 coil system for the SXD configuration compatible with ports location (blue stars), but without mesh morphing (the blue dots represent the morphed TF coil). (right) Comparison among original (red) and modified PF coil systems (black).

From the point of view of the coil geometry, apart from the SXD, the control figures given in Table 10 do not include mesh morphing, but only corrections to the 2018 configurations to accommodate suitable remote handling ports. The mesh morphing we applied to the SXD tends to make the TF coils larger, so it is possible that the increase of power requested will affect all the ADC configurations as well as the baseline SND. Note also that the control circuits that we used are not up/down balanced. By optimizing the number of turns in the imbalance circuit for each coil, the requested power could be decreased. In our case, this was not

possible since our analysis did not take into account of the turn division of the PF coils, but it should be considered for future work.

What can really change the game, however, are internal coils. A control system based on them would have power requests more than two orders of magnitude lower, as shown in the following table:

Table 11: Power required to bring back a displaced plasma depending on the configuration, discharge phase and amount of displacement. These calculations were done for the 2020 configurations with two internal coils and a voltage 10 times the minimum required to stabilize a perturbation at $t \rightarrow \infty$.

Configurations		Scenario snapshot	Power request [MW] VDE 5cm	Power request [MW] VDE 10cm	Power request [MW] VDE 15cm
SXD	With Stability plate	FT	0.9	3.6	8.1
		FT_li1	1.1	4.4	9.9
		SRD	2.0	8.1	18.2
	Without Stability plate	FT	1.1	4.2	9.5
		FT_li1	1.3	5.1	11.6
		SRD	2.4	9.5	21.9
XD	With Stability plate	FT	0.6	2.5	5.6
		FT_li1	0.5	2.1	4.8
		SRD	1.5	6.1	13.6
	Without Stability plate	FT	0.7	2.7	6.2
		FT_li1	0.6	2.3	5.3
		SRD	1.7	6.7	15.1
SFD	With Stability plate	FT	0.7	2.6	5.9
	Without Stability plate	FT	0.5	2.0	4.5

Clearly, stabilization of the ADCs would become feasible by including internal coils, but other considerations might enter on the viability of this solution, so this will need to be an integrated decision. It is worth noticing that stabilizing plates give almost no advantage when coupled with internal coils.

Finally, one of the reasons why the ADCs were more subject to displacements was that the passive stabilizing structures were farther away from the plasma than in the SND case. Another option that was not yet tried would be to design better internal wall structures, more closely fitting the equilibrium shape.

4.3 Remote Handling

Structural calculations show that strengthening the inercoid structures is advantageous, but their poloidal extension is naturally limited by the access ports. There is therefore tension

between ensuring good remote handling (installation and removal) and rigidity of the TF coil cage. It is therefore important to include from an early stage in the design considerations on how to manipulate the breeding blanket segments and the divertor cassette, which are the two most critical removable components. Also, ensuring proper pumping of the Helium ashes requires clear pathways to the pumps, which are typically located in the lower port, and divertor modifications.

In 2019, each 2018 ADC configuration was reviewed by the remote handling team, which gave recommendations on how to modify the designs. Remote handling studies were not directly part of WP-DTT1/ADC as was funded by PPPT's KDII3 activity. However, for its importance, several discussions and interactions occurred over the years and this generate a single engineering team that worked together. The following re-engineering of the configurations was carried out by the WP-DTT1/ADC team and hence we give a brief overview of the remote handling issues and their consequences here.

For the SFD, the 2018 design underestimated the stresses in the TF coils, since the intercoil structures used had an unacceptable poloidal extension. Indeed, a major issue for the SFD is the accessibility of the divertor region for installation and remote handling operations. The *a posteriori* assessment showed that the 2018 configuration was not compatible with the divertor cassette removal as the intercoil structures encroached into the lower port. Also, the upper port was too narrow, and the inner blanket removal would not be possible.

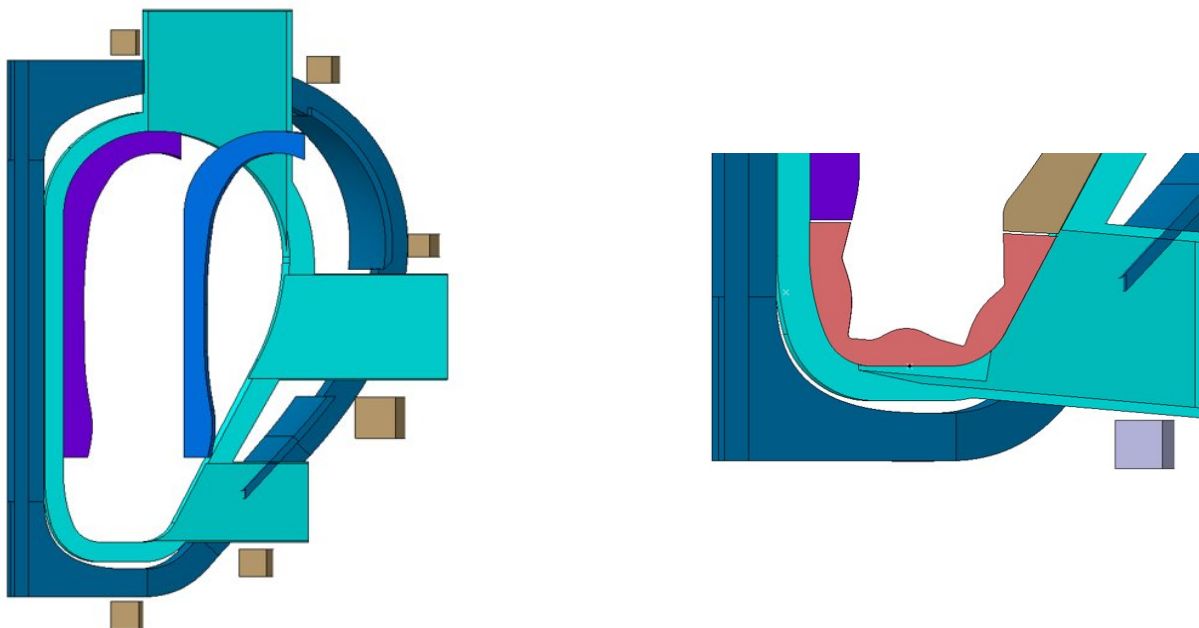


Figure 32: Remote handling problems for the 2018 SFD configuration. The upper port would not allow extraction of the inner blanket (left) and the intercoil structures would encroach the lower port and prevent the extraction of the divertor cassette (right).

This has led to a redesign of the coils and the structural calculations presented in Figure 26 and detailed in the figure below:

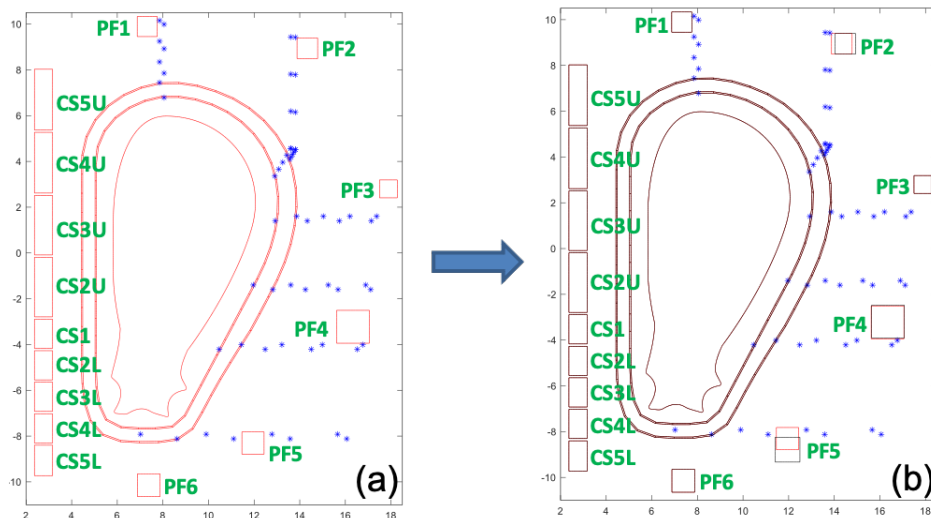


Figure 33:(left) PF coil system for the 2018 SFD configuration not compatible with ports location (blue stars). (right) Comparison between the 2018 (red) and modified 2020 morphed coil systems (black).

In general, a fundamental complexity and weakness of the SFD is the need to bring PF5 and PF6 close to the bottom low field side part of the TF coil while remaining sufficiently separated to efficiently generate the hexapole null. This creates problems of space for the lower port and therefore of accessibility of the divertor.

For the XD, the equatorial and lower port could be reduced to increase the rigidity of this design, but the upper port cannot be further shrunk because it already presents challenges in terms of safe extraction of the inner blanket structures, which would require complex kinematics. In addition to the fact that the upper port should not be enlarged to avoid weakening of the structure, there is no physical space due to the proximity of PF1 and PF2, so that blanket handling is difficult. These, however, seem to be issues connected with the current design rather than intrinsic to the XD configuration. In general, while feasible, the inner blanket and divertor cassette removal present complex kinematics (see Figure 34), which require rotations of the structures. While the 2018 configuration was not port optimized, considering the XD as an option for DEMO would require a more detailed analysis.

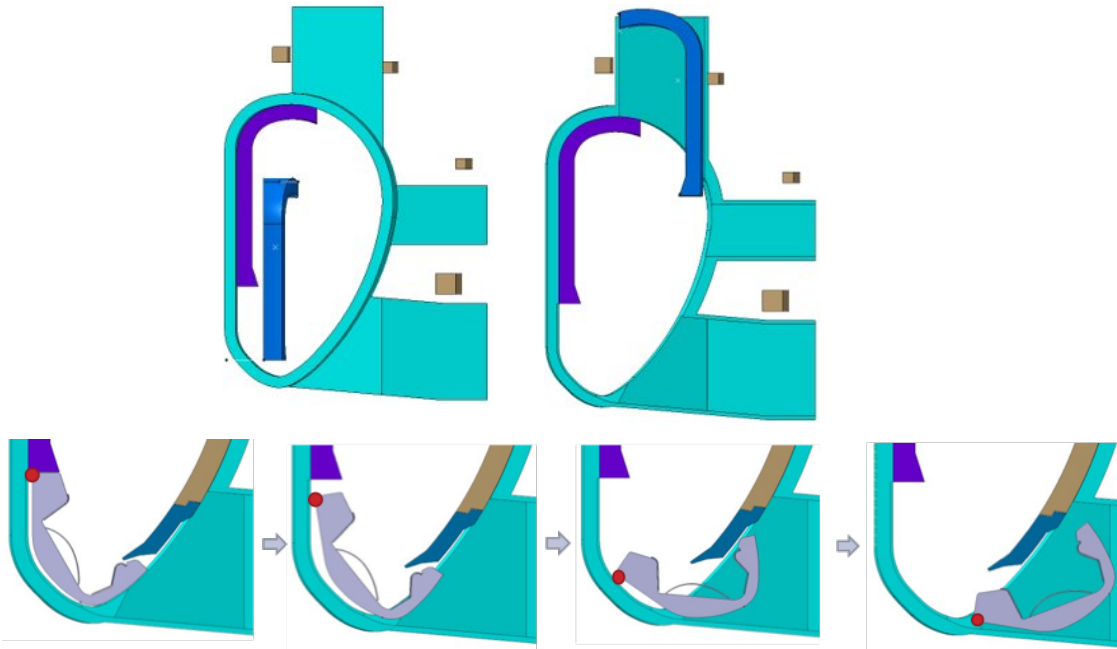


Figure 34: possible kinematics for the divertor and inner blanket extractions in the 2018 XD configuration.

Moving to the SXD, all ports in the 2018 configuration provided almost adequate access to both the blankets and the divertor, as long as the divertor cassettes are properly shaped. Only minor modifications were therefore required in the 2020 designs. A possible extraction solution for the divertor cassette is shown below:

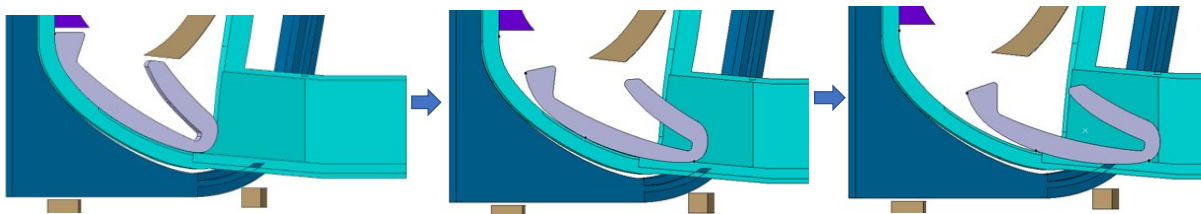


Figure 35: possible extraction solution for the SXD divertor cassette.

As a matter of fact, the upper port could be slightly reduced on its high field side to reduce the stresses on the TF coils, with consequences on blanket handling extraction that can probably be handled. The modification of the SXD in 2020 were mainly driven by the need to reduce the stresses in the coils and Figure 31 shows how this affected the configuration (ports are shown there).

As a result of these observations, new 2020 configuration were designed, improving the 2018 ones. The changes implemented in the ports can be seen in the figure below:

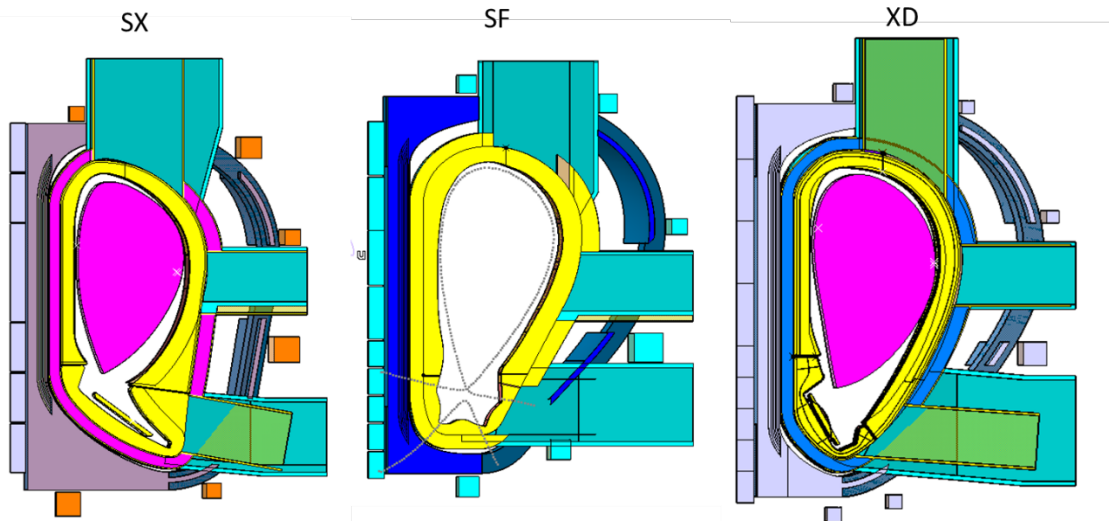


Figure 36: comparison between the 2018 and 2020 port compatible port layout.

Overall, the remote handling compatible 2020 configurations for all the ADCs are shown below and compared with the SND.

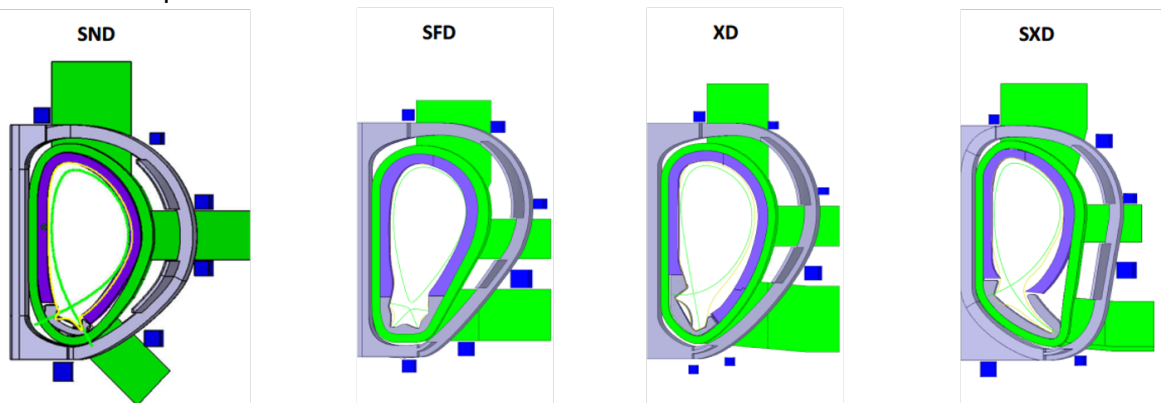


Figure 37: 2020 port compatible ADCs compared with the SND. The 3D builds show the layout of the coils, ports, divertor and blankets.

An interesting observation that is common to the ADCs examined is that the lower port needs to be close to horizontal due to the need of positioning PF5 in particular positions to generate the ADCs' characteristic features.

4.4 Pumping

Moving now to pumping, the analysis was performed using the Monte Carlo code DIVGAS [S. Varoutis et al., Nucl. Materials and Energy, vol. 19, pp. 120-123, (2019)], which allows to track the dynamics of the atomic deuterium, helium and argon in the divertor region. The solution of the Boltzmann kinetic equation for the neutral particles is reproduced by simulating the collisions and the ballistic flight of model particles, which statistically mimic the behaviour of real atoms. This approach allows to evaluate the pumping efficiency required to remove the incoming flux but also to optimize the position of the pumping opening as well as assessing its influence on the neutral flow behaviour in the private flux region (PFR).

For each DIVGAS pumping simulation a given divertor geometry should be provided. The code then launches particles from given surfaces (e.g. the divertor legs or arbitrary regions in the

PFR), see Figure 38. In this model, the neutral particles penetrate the private flux region (PFR) through a virtual line called “Interface A” below the separatrix and neutrals can either flow downwards towards the pumping ports or flow backwards towards the separatrix, leaving the flow domain. Each pumping port includes an adsorbing surface with a given capture coefficient ξ (i.e the probability of a particle to be pumped from there). Consequently, ξ takes values between $0 \leq \xi \leq 1$. The capture coefficient indicates the efficiency of the vacuum pump solution and based on the current technological level, the maximum realistic value, which can be achieved is 0.2 to 0.3. If the particle is not finally exhausted at the pumping port, then it undergoes a diffuse reflection, assuming that the temperature at the entrance to the pumping port is equal to 696 K.

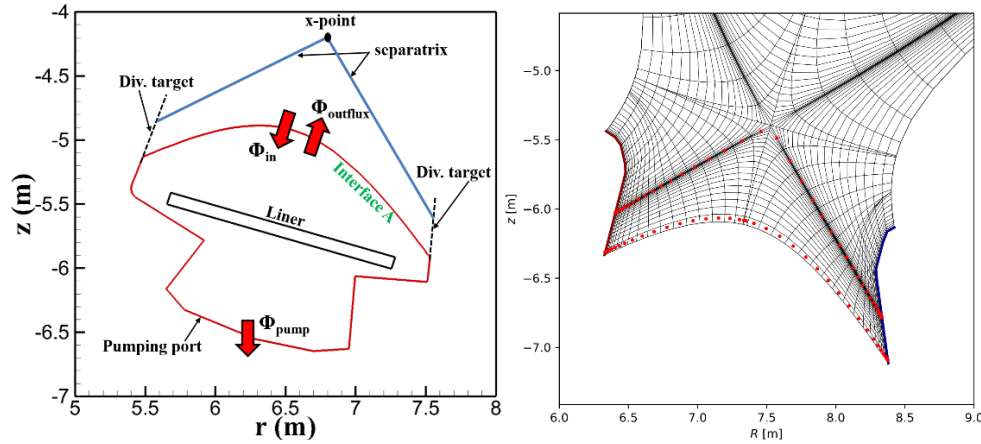


Figure 38: (left) Indicative 2D numerical model extracted from a 3D CAD file for the case of SND divertor. The area bounded by the green curve is the computational domain of DIVGAS. (right) Locations inside the plasma simulation domain, from which the neutral input data have been extracted (depicted as red dots). These are either given by SOLPS runs or imposed.

The simulations performed assume a gas mixture consisting of atomic deuterium (D), helium (He) and argon (Ar), based on a predefined density n_0 and temperature T_0 for each specie and provided by the SOLPS plasma simulations along the prescribed interface A (see right panel of Figure 38) or imposed in an *ad hoc* way (both approaches were used). The quantities n_0 and T_0 define the incoming neutral flux Φ_{in} for each species, as shown in Figure 38, while the remaining particle fluxes $\Phi_{outflux}$ and Φ_{pump} are the output of the DIVGAS simulation. The particle flux Φ_{in} is calculated by assuming Maxwellian distribution of incoming neutrals using the expression:

$$\Phi_{in} = \frac{1}{4} S n_0 \sqrt{\frac{8k_B T_0}{\pi m}},$$

where S is the length of the line segment (in 2D) or the area of the surface (in 3D), from which neutrals are injected in the private flux region, k_B the Boltzmann constant and m is the molecular mass. The above assumption of Maxwellian distribution does not include the effect of charge exchange process, which, if considered, would result in lower values of incoming neutral particle fluxes Φ_{in} .

Another important input parameter, which is used mainly for post-processing and comparison purposes in the total puffing (or generation in the case of helium) rate Φ_{puff} for each specie. This value will be compared with the estimated pumped flux Φ_{pump} obtained by DIVGAS simulations to assess pumping efficiency since in steady-steady operation both values should be equal, namely $\Phi_{puff} = \Phi_{pump}$. By applying indirectly this particle balance, it is possible to extract the number of pumping ports needed to exhaust the injected puff rate for

each specie. In other words, Φ_{puff} consists of the pumping requirement for a given divertor configuration. For helium the pumping requirement is chosen to be equal to $7.0 \times 10^{20} \text{ (s}^{-1}\text{)}$, which corresponds to the total helium flux produced in the DEMO reference conditions with 2 GW fusion power.

In a DIVGAS simulations, ionization, dissociation and recombination processes are not considered (although the physical models exist), while the wall recombination of atomic deuterium to molecular deuterium (dynamic evolution) is included. Within this gas-surface interaction process, deuterium atoms when impacting the wall are recombined to deuterium molecules based on a given recombination probability equal to 0.4 for the case of tungsten wall. The rest of the deuterium atoms are backscattered from the wall with Maxwellian distribution based on the wall temperature. For the targets the wall temperature is equal to $T_{\text{targets}}=1160\text{K}$ (0.1eV), while for the rest of divertor walls the temperature is equal to $T_{\text{wall}}=696\text{K}$ (0.06eV). More details on how the code works are available in this specification document on IDM: <https://idm.euro-fusion.org/?uid=2MRRE3>.

Initial calculations for deuterium and helium only were performed by assuming a given neutral pressure in the divertor entrance, so that the analysis could start without waiting for the multifluid results. These calculations only give a rough idea of how the different ADC geometry can affect pumping, but they cannot be considered as realistic assessments. In particular, the particles were launched from the divertor legs (see upper panels of Figure 39) with a temperature of 1eV and a pressure between 1Pa and 5Pa.

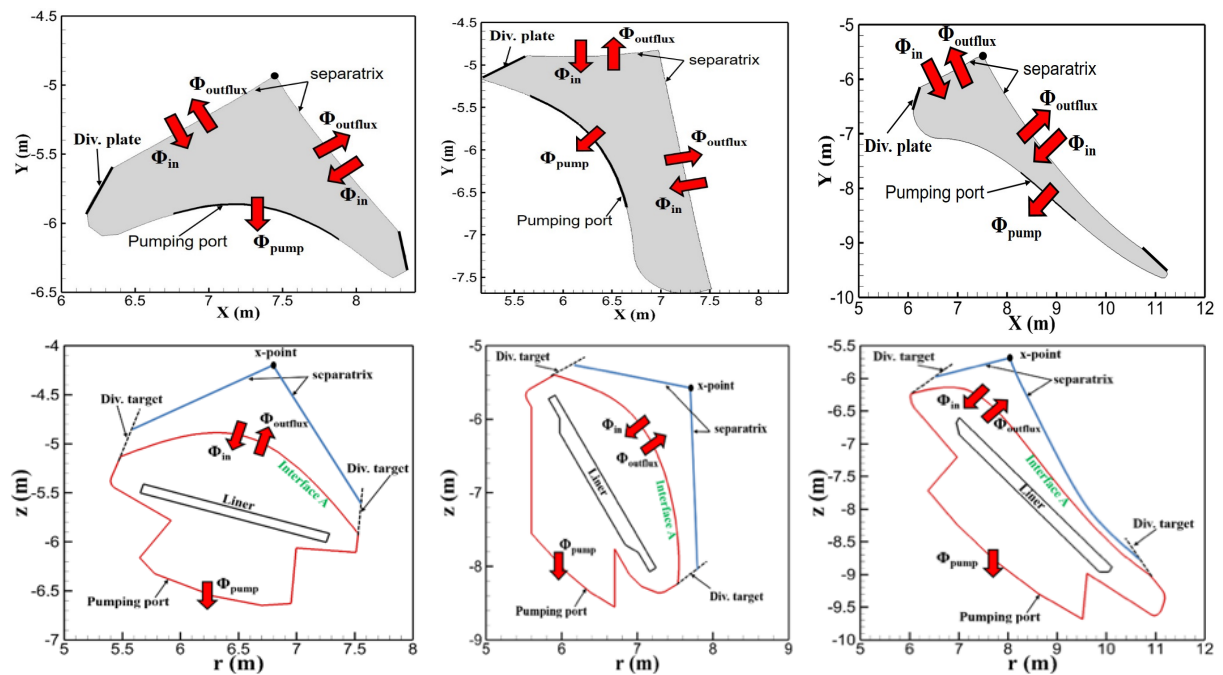


Figure 39: computational domains of DIVGAS for the imposed input parameters (upper panels) and SOLPS provided input parameters (lower panels). From left to right, the SND, XD and SXD configurations are shown.

The specific input data were the following:

Table 12: Incoming particle flux Φ_{in} ($\text{s}^{-1}\text{m}^{-1}$) for the considered divertor configurations and boundary conditions at the separatrix.

	SND	XD	SXD
--	-----	----	-----

	D	He	D	He	D	He
$P_0=1$ Pa, $T_0=1$ eV	4.61E+22	3.23E+21	6.90E+22	4.84E+21	1.10E+23	7.70E+21
$P_0=5$ Pa, $T_0=1$ eV	2.305e+23	1.615e+22	3.45e+23	2.42e+22	5.5e+23	1.54e+21
$P_0=10$ Pa, $T_0=1$ eV	4.61E+23	3.23E+22	6.90E+23	4.84E+22	1.10E+24	7.70E+22

The results of the simulations are given below and compared against the pumping requirement (dashed line):

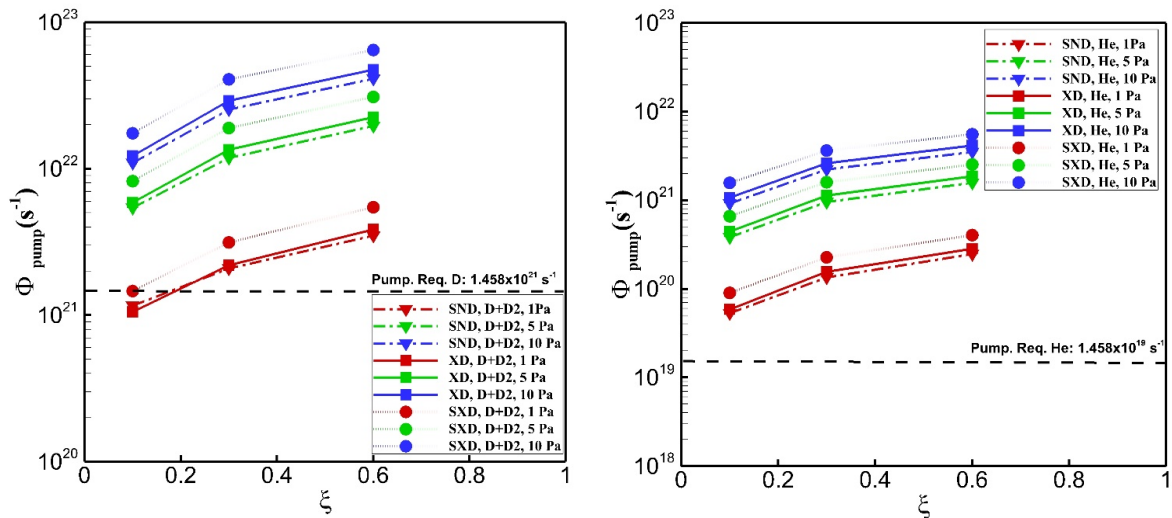


Figure 40: Considering one divertor cassette, pumped flux in terms of the capture coefficient ξ for (left) atomic and molecular deuterium and (right) helium for all separatrix pressures and configurations considered.

Not surprisingly, higher pumping efficiencies and divertor pressures lead to larger pumped fluxes. The differences between the different configurations are not very large and all the designs ensure acceptable pumping levels of both helium and deuterium.

More recent calculations were performed using as an input the fluxes obtained in the SOLPS simulations discussed in Section 2 and were therefore more self-consistent. The three simulations chosen are shown with a red circle in their operating space in the figure below:

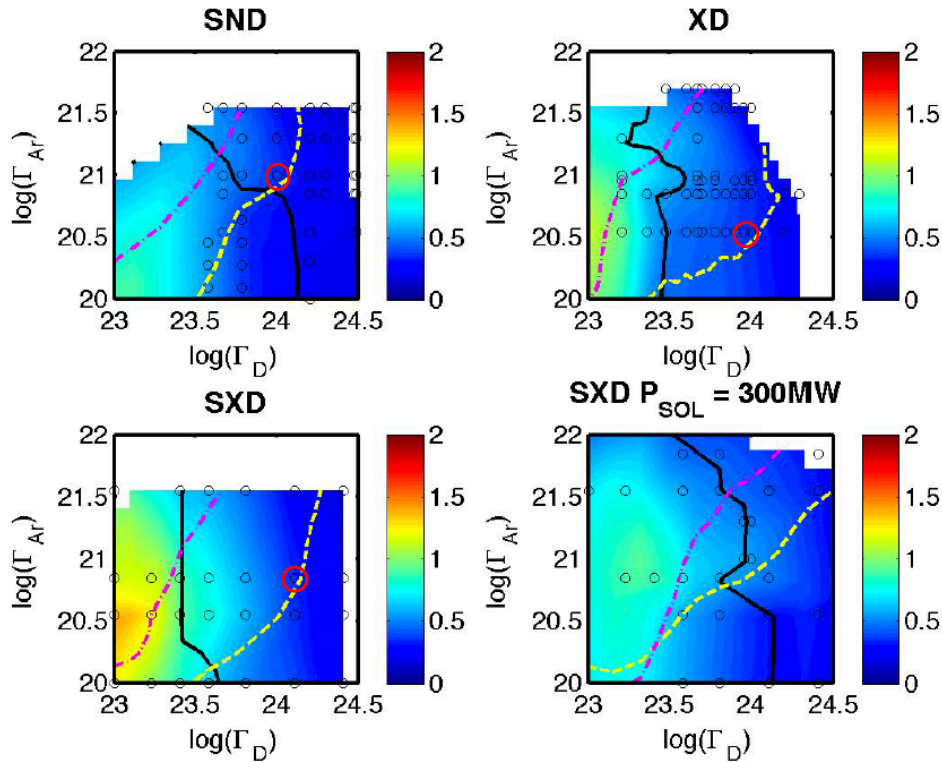


Figure 41: the red circles indicate the SOLPS simulations used as an input of the DIVGAS modelling.

No SFD assessment was possible due to the fact that no converged SOLPS run in the operating space was identified.

In this case, also the interface surface was moved deeper into the PFR so that plasma/neutral interaction effects were minimized, and emphasis was given to the neutral dynamics in the subdivertor structures (see lower panel of Figure 39).

These simulations were performed including also Argon, and the total input fluxes were:

	SN	X	SX
D	1.21E+24	7.05E+23	1.32E+24
He	2.83E+20	1.41E+20	3.12E+20
Ar	1.18E+21	2.72E+20	6.91E+20

Figure 42: Total incoming particle flux Φ_{in} ($m^{-2}s^{-1}$) for the considered divertor configurations and boundary conditions.

The results, shown in the figure below, show that pumping can be problematic in all configurations, including the SND, and that the SXD gives a marginal benefit with respect to the other options.

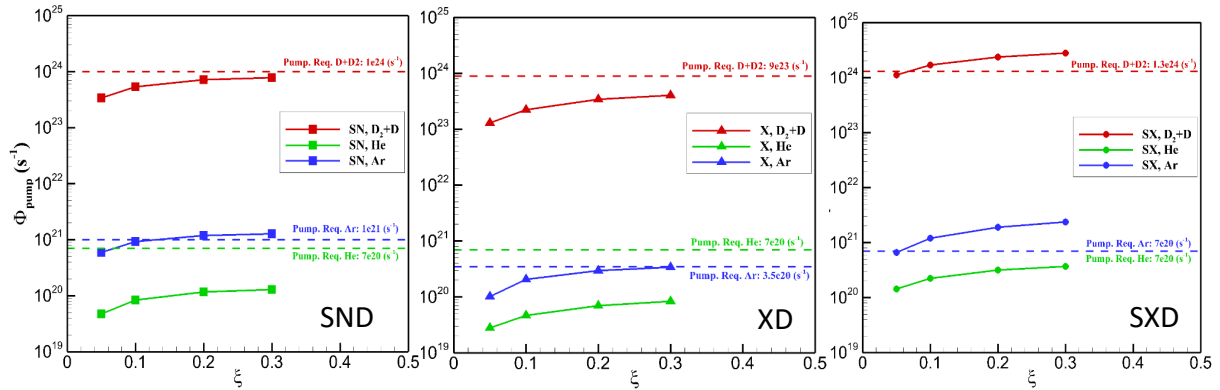


Figure 43: pumped flux in the SND (left) XD (centre) and SXD (right). These simulations are based on SOLPS input and employ a liner in front of the port and include subdivertor structures. The dashed lines represent the pumping requirement.

In particular, the SND does not reach the pumping requirements for deuterium or helium, but the argon pumping is acceptable if ξ is above 0.1. For the XD, no species can be pumped efficiently, while for the SXD only helium is problematic. However, note that these results should not be interpreted too literally, as the SOLPS simulations cannot assure a reliable estimate of the neutral pressure at the divertor. This is a long-standing deficiency of the code, which is exacerbated when a fluid model for the neutrals is employed, like in our case. As a consequence, the only reasonable conclusion comes from the comparison between the different configurations rather than from the absolute values obtained. In this case, the SXD seems to give an advantage because of its large surface and because it has a higher incoming flux in the PFR.

The DIVGAS simulations also provide velocity maps for the neutrals simulated. Figure 44 shows the flow patterns in the different configurations for $\xi=0.1$ and $\xi=0.3$. It is clearly seen from the streamlines that in steady-state conditions, the net flow of neutrals is divided in two parts, the first and smallest part describes the neutrals moving towards the pumping opening, while the remaining and biggest part describes the neutrals moving towards the X-point. This behavior is almost independent from the boundary conditions and the divertor configuration. This is justified from the fact that the outflux of neutrals is always orders of magnitude higher than the corresponding pumped flux. For all the divertor configurations considered, the neutral outflux weakly depends on the capture coefficient ξ (in all simulations the outflux of deuterium is 3-4 order of magnitude higher than for the gas impurities).

As it is seen, in all divertor cases the pressure of the mixture maintains its highest values in a narrow area close to the strike points. As the neutrals enter the sub-divertor area the pressure drops rapidly and remains almost homogeneous.

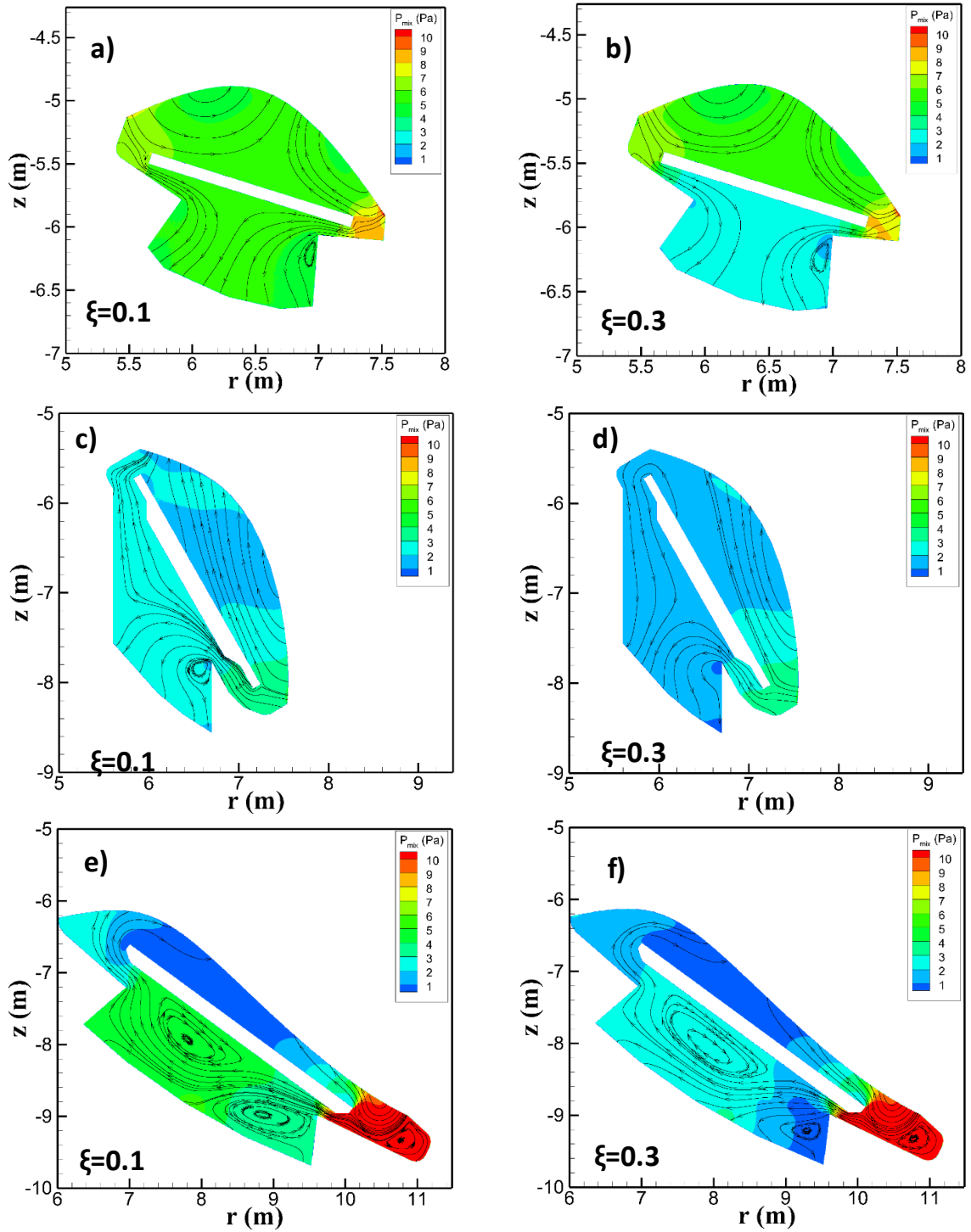


Figure 44: velocity maps for the different configurations for two different values of the pumping efficiency for SND (top row), XD (middle row) and SXD (bottom row).

As it is expected, in all divertor concepts the increase in the capture coefficient is followed by a decrease in the neutral gas pressure. Moreover, the behavior of the overall gas mixture is mainly driven by the atomic and molecular deuterium particle transport. For all divertor configurations as ξ is increased from 0.1 to 0.3 the pressure is decreased by a factor of about 3, with the pressure in the X divertor being always significantly lower comparing to that in SN and SX divertors.

In the case of the SXD divertor, the existence of vortices inside the sub-divertor area is observed. More specifically, two vortices appear below the liner and close to the pumping opening, which mainly intercept the path of neutrals toward the pump. However, for the SND and XD, the size of vortices is significantly smaller, and they do not influence the particle path. Moreover, in the case of SXD divertor, due to the fact that the pressure in LFS strike point is much higher than in the HFS strike point, the resulted flow of the mixture shows that the particles move below the liner from LFS to HFS without having the chance to be pumped out.

4.5 Neutronics

Neutronics studies were initiated in 2020 to ensure that the ADCs could sustain the elevated neutronic fluxes that DEMO will generate without affecting the tritium breeding ratio (TBR). Extensive work was done by the neutronics team in a short amount of time, leading to a comprehensive review of the effects of irradiation.

The neutron generated by DT fusion reactions has a particularly high energy, equal to 14.1 MeV. By nature of its neutral charge, the neutron is highly penetrating and at these energies far exceeds the threshold of most threshold reactions. This is significantly different from a typical fission reactor spectrum, where neutrons are born with 1-2 MeV and therefore presents a new set of challenges. The implications of fusion neutrons and their interactions with the materials in the fusion reactor are far reaching. Our analysis covers a range of nuclear responses, both specific to the divertor and the wider reactor.

It is important that the neutronics assessment is factored in as early in the design as possible. The starting point for the assessment is a CAD description of the problem, which only this year has become available for each ADC configuration at a level suitable for radiation transport analysis. If the neutronics analysis is delayed and underlying issues are found, shielding options may be required which by this stage may be prohibited because of, for example, space constraints. Failing that, maintenance operations have to be revised in turn having potentially significant ramifications for operations.

The CAD models provided to the neutronics team included only components up to the vacuum vessel and the TF/PF coils. However, for an assessment of the ex-vessel region, it was necessary to complete the model including the cryostat and bioshield (see Figure 45 for an example of the additions). The results presented here are preliminary, and they should be repeated when more detailed CAD will be available.

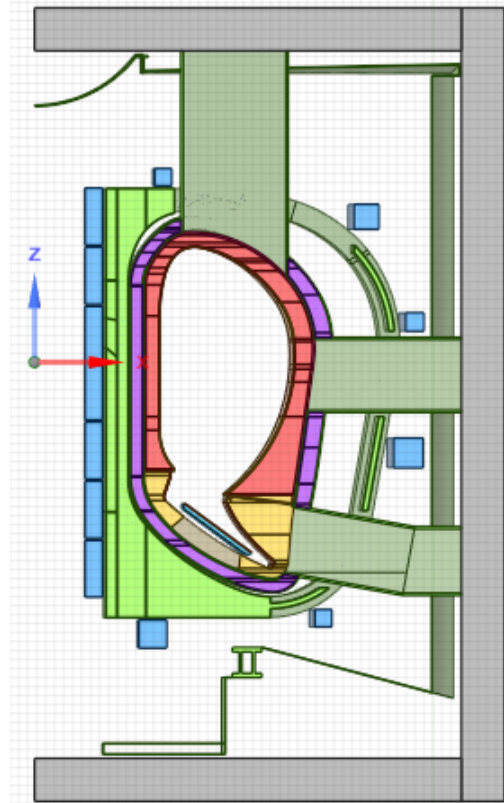
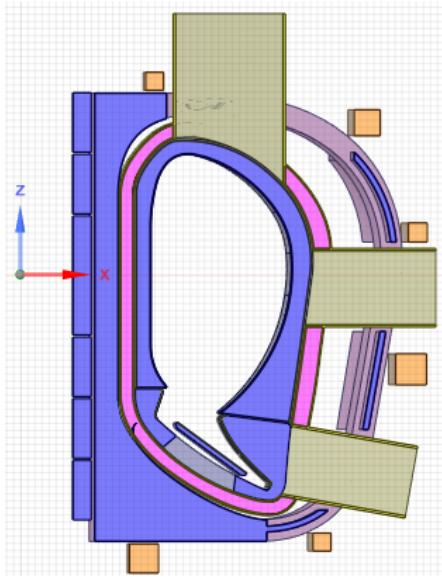


Figure 45: Original CAD model for the 2020 port compatible configuration for the SXD (left) and extended CAD model with cryostat and bioshield (right).

All neutron and photon transport calculations have been performed using MCNP6v1 [D. Pelowitz et al., "MCNP6 Users Manual – Code Version 1.0, LA-CP-13-00634 Rev 0] and MCNP6v2 [C. J. Werner et al., "MCNP User's Manual Code Version 6.2," Los Alamos Natl. Lab., 2017]. The nuclear data library JEFF-3.3 [NEA, "Joint Evaluated Fission and Fusion (JEFF) Nuclear Data Library JEFF-3.3," 2017] has been used in accordance with the instructions for nuclear analysis document [U. Fischer, "Guidelines for Neutronics Analyses." EFDA_D_2L8TR9, 2018]. Where data is not available for particular isotopes, FENDL3.1 [R. A. Forrest and et al, "FENDL-3 Library: Final Report.," INDC(NDS)-0645, 2013. [Online]. Available: <https://www-nds.iaea.org/publications/indc/indc-nds-0645/>] is used.

In order for the analysis to be carried out, a neutron source has to be defined. In all cases, DEMO operational power of 1998 MW is assumed giving a source normalisation applied to all calculations of 7.094×10^{20} neutrons s^{-1} . This was a standard procedure used also for the DEMO baseline and produced the distributions shown in the figure below:

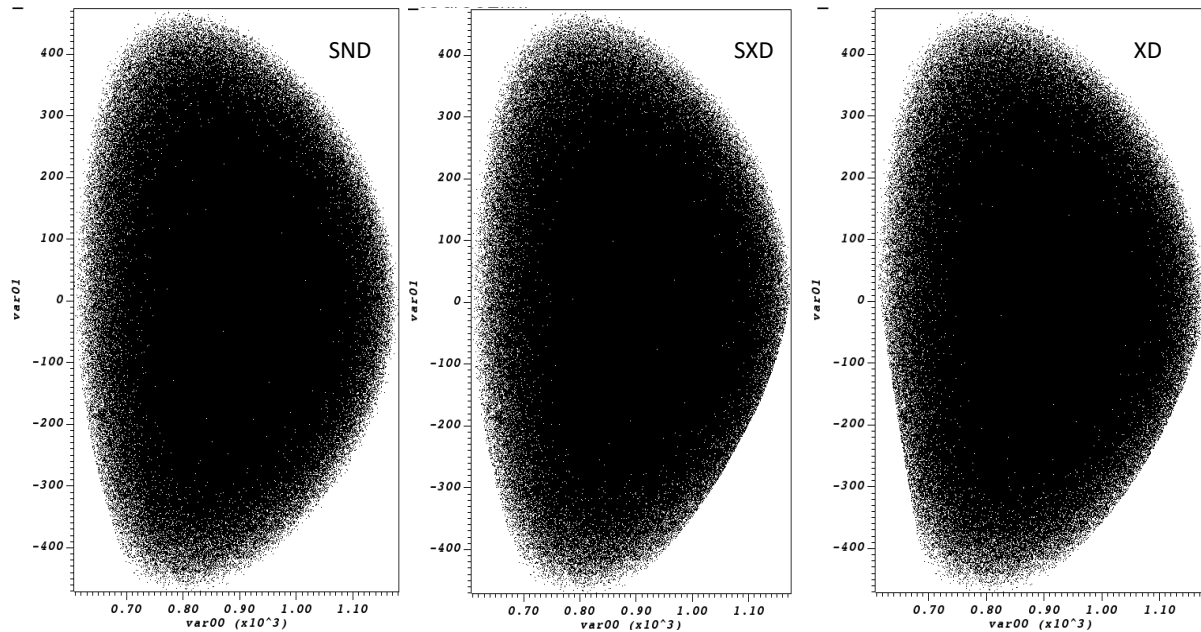


Figure 46: distribution of the neutron point sources in the plasma cross section for the SND (left), SXD (centre) and XD (right).

Not surprisingly, the distributions are similar to each other as the core plasmas was chosen to be as similar as possible by design.

Given the preliminary nature of the assessment, a number of simplifying assumptions have been taken and are described below:

- All components are homogenised;
- The blanket consists of a single homogenisation of breeder zone (BZ), Manifold and back plate;
- All ports are completely open;
- No void fraction in the cassette which would account for openings and penetrations for pipe structures for example.

Since the emphasis of our work is on the comparison between different configurations, these approximations were considered acceptable.

The CAD to MCNP conversion process requires some simplifications of the geometry. The MCNP geometry consists of 1460 geometry cells, of which 1171 are tokamak components and the rest are void space between the components and surrounding the tokamak. 1692 surfaces are employed to define the boundaries of these cells. The consistency of the CAD and MCNP representations was checked by comparing the volumes of the cells, finding good agreement. The result of the simplification for the XD is shown in Figure 47 as an example.

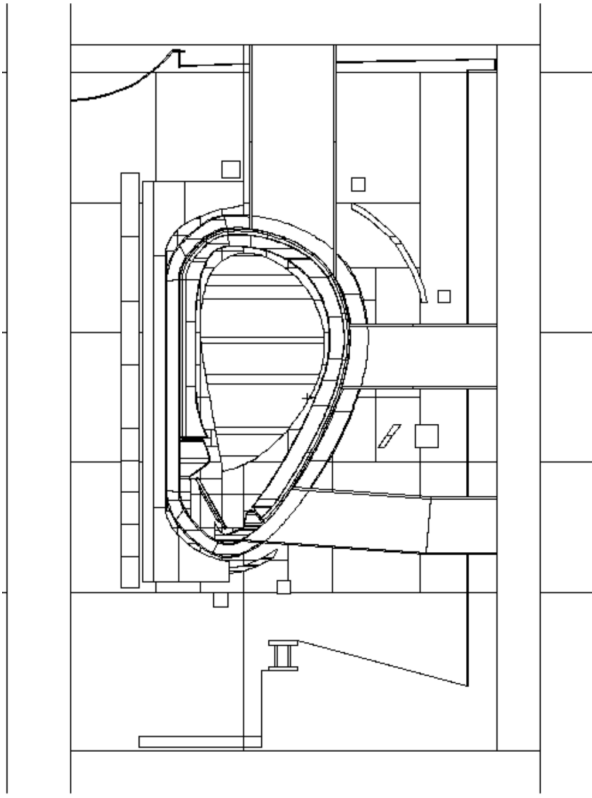


Figure 47: MCNP representation of the XD geometry.

Also, the model was checked for geometry errors such as interferences by running a lost particle test.

The MCNP material definitions for all components of the ADCs have been prepared in accordance with the IDM documents “Guidelines for Neutronic Analyses” [U. Fischer, “Guidelines for Neutronics Analyses.” EFDA_D_2L8TR9, 2018] and “Material compositions for PPPT neutronics and activation analyses” [U. Fischer and Y. Qiu, “Material_compositions_for_PPPT_neutronic_2MM3A6_v1_2.”] which are recommended in neutronic analyses and calculations. The same material definitions of components have been applied to all the models considering the different divertor configurations. The list of materials, their composition, atomic densities, volume fractions as well as assignment to individual components can be found on IDM in the detailed 2020 WP-DTT1/ADC Activity E5 report (section 6).

Coming now to the results, a neutron flux map was generated for the configurations investigated and shown in Figure 48. A few observations can be made. First of all, for all the configurations there is a probably excessive streaming towards the vacuum vessel through the pumping ports, which should be reduced by including more shielding (a liner was added also for pumping purposes, but it does not yet sufficiently efficient).

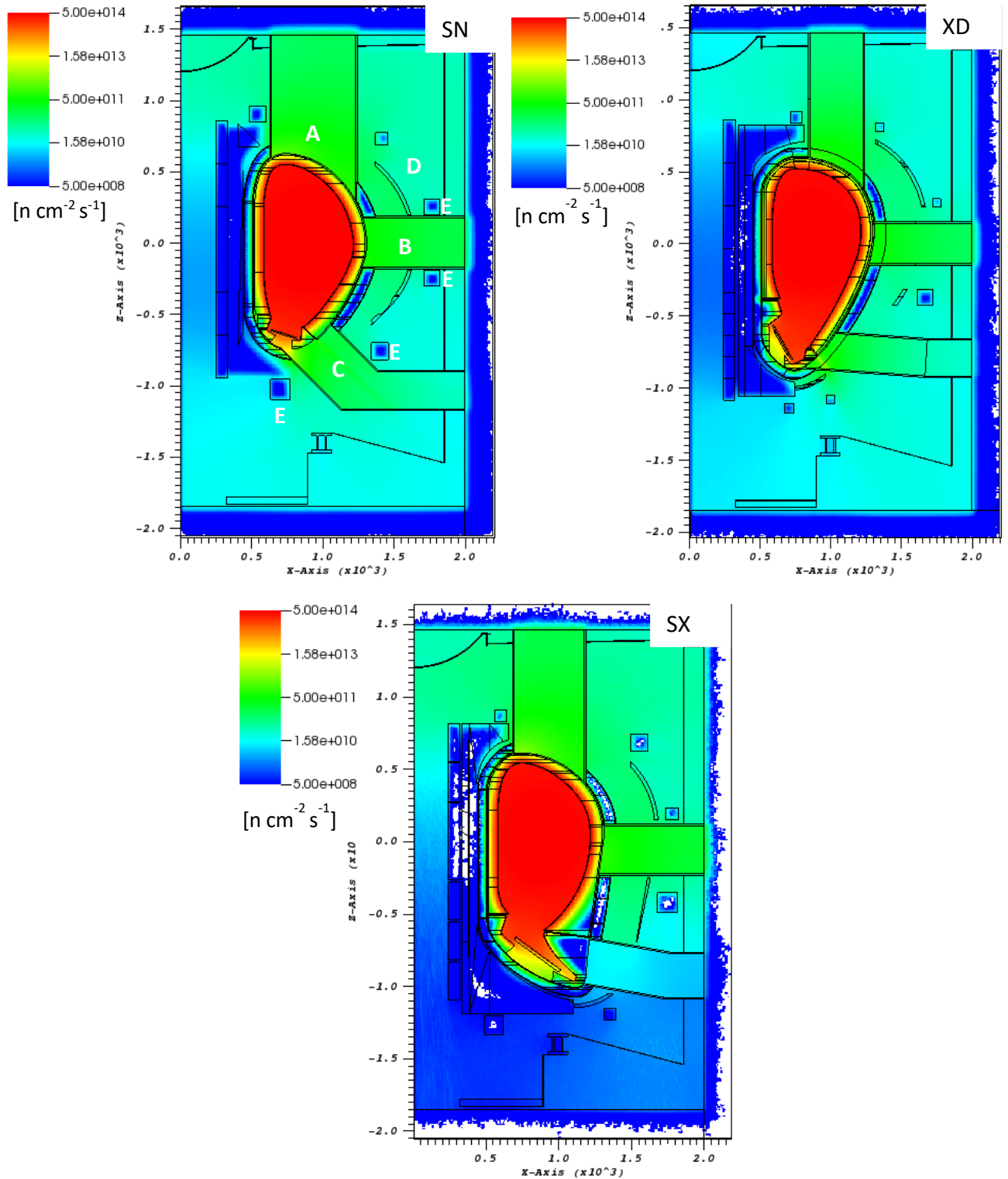


Figure 48: Neutron flux for the 2020 port compatible ADC configurations.

In terms of resulting nuclear heating in the divertor, the total loads are of the order of a few MW: 3.95MW for the SND, 4.73MW for the SXD and 4.59MW for the XD. Each of the models have a homogenized description of all divertor components which gives improved nuclear shielding performance. In particular, the cassette is described as 56% Eurofer and 44% water. In reality, there will be many openings through the cassette and indeed all divertor

components to allow space for pipe cooling channels for example. Calculations with heterogeneous materials are expected to give a slightly lower load. The results obtained are in line with the volume of the divertor in each configuration and are therefore not surprising. More important is therefore the nuclear heating density. A map for this quantity is given in the figure below:

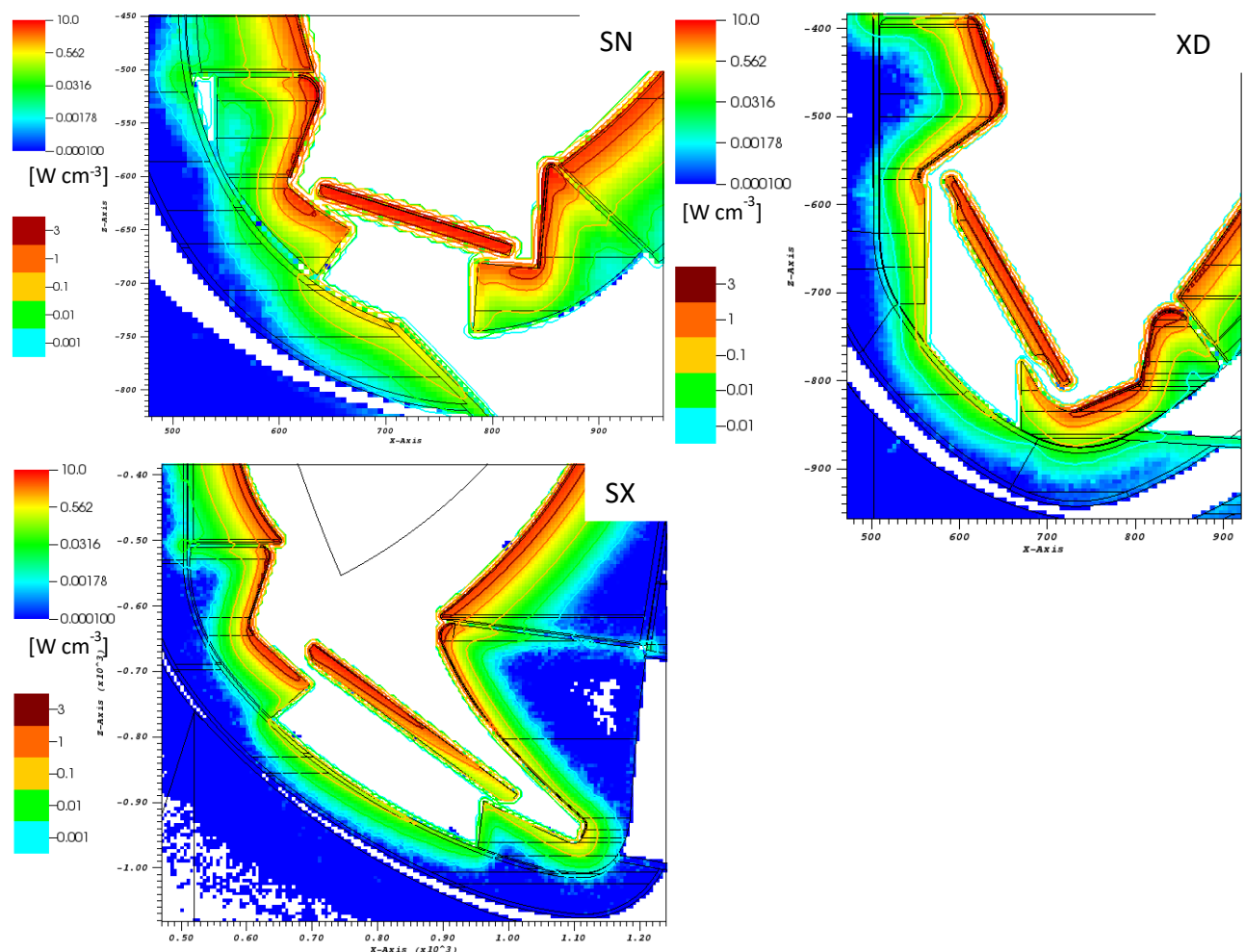


Figure 49: Nuclear heating density for the three divertor configurations.

Note that the target value for the vacuum vessel is $0.3\text{--}0.5 \text{ W cm}^{-3}$. The SND presents the higher values in the vacuum vessel, with a peak at 0.33 W cm^{-3} , which however lies within the bounds. For the XD the peak value in the VV is 0.05 W cm^{-3} , and for the SX, 0.09 W cm^{-3} .

The nuclear heat density in the TF coils is a critical quantity that must be kept below the limit of $5 \times 10^{-5} \text{ W cm}^{-3}$. The TF coils in DEMO will be superconducting, cooled using liquid helium to temperatures of 4K and maintaining these temperatures is critical to their operation. The best way to present this is as maps with the loads normalized to the critical value, which are presented in Figure 50. To focus on the TF coil load, loads through paths in the TF coil casing and winding pack are shown in Figure 51 and give a more direct overview of which are the poloidal sections that are beyond the threshold.

The lower port shielding in the SXD configuration gives lower heat density in the coil for segments 5 and 6. Around the equatorial region, the XD performs the best owing to the small

port dimensions, which also holds true at the upper port level. The limit is also plotted showing that for all inboard poloidal segments, the configurations are below the limits. For all outboard segments, however, the limit is systematically exceeded with one exception, the poloidal segments next to the lower port in the SX. Due to its importance, this issue should require attention going forward.

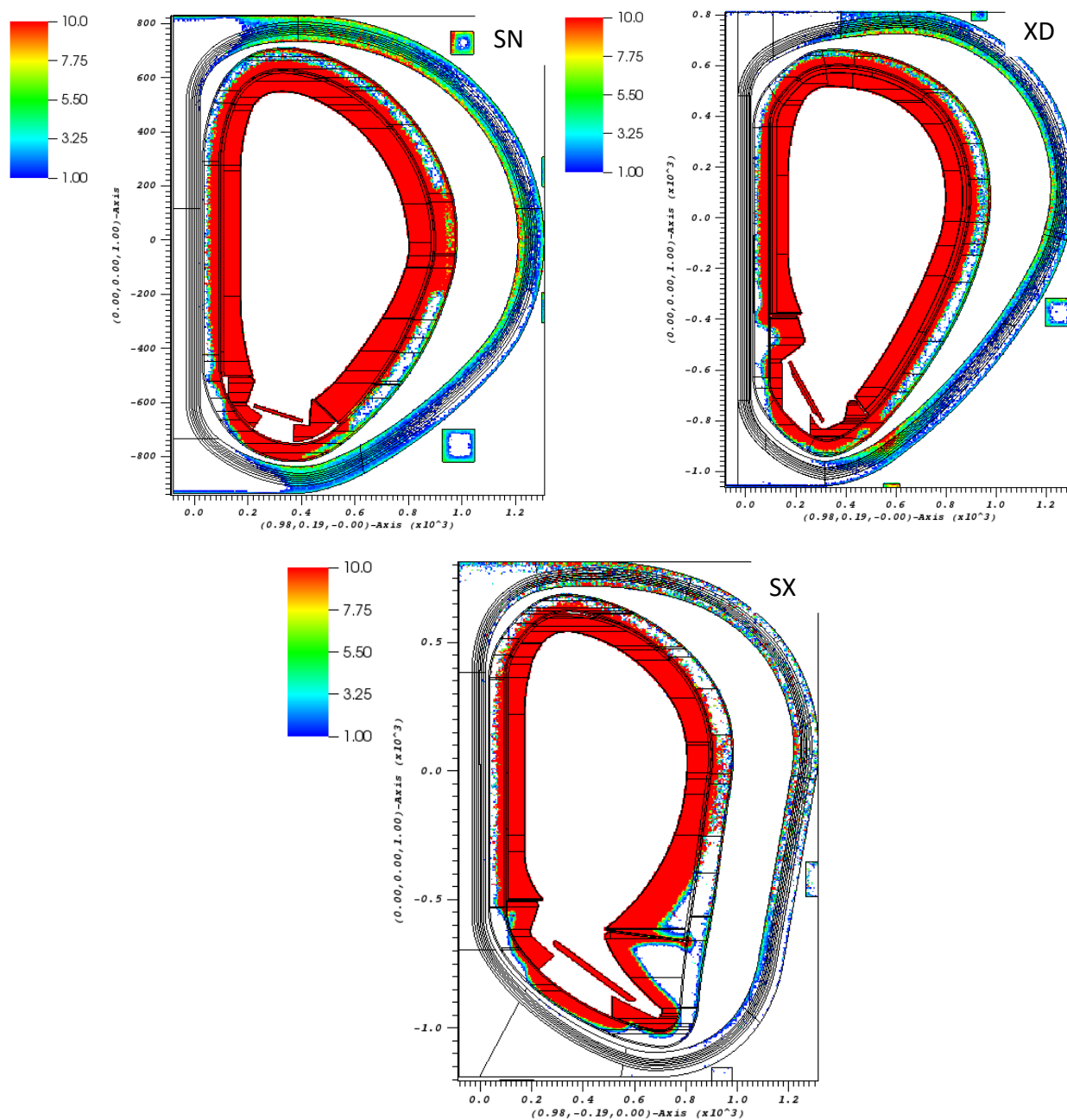


Figure 50: nuclear heating density map normalised to the critical value $5 \times 10^{-5} \text{Wcm}^{-3}$ for the three different configurations examined.

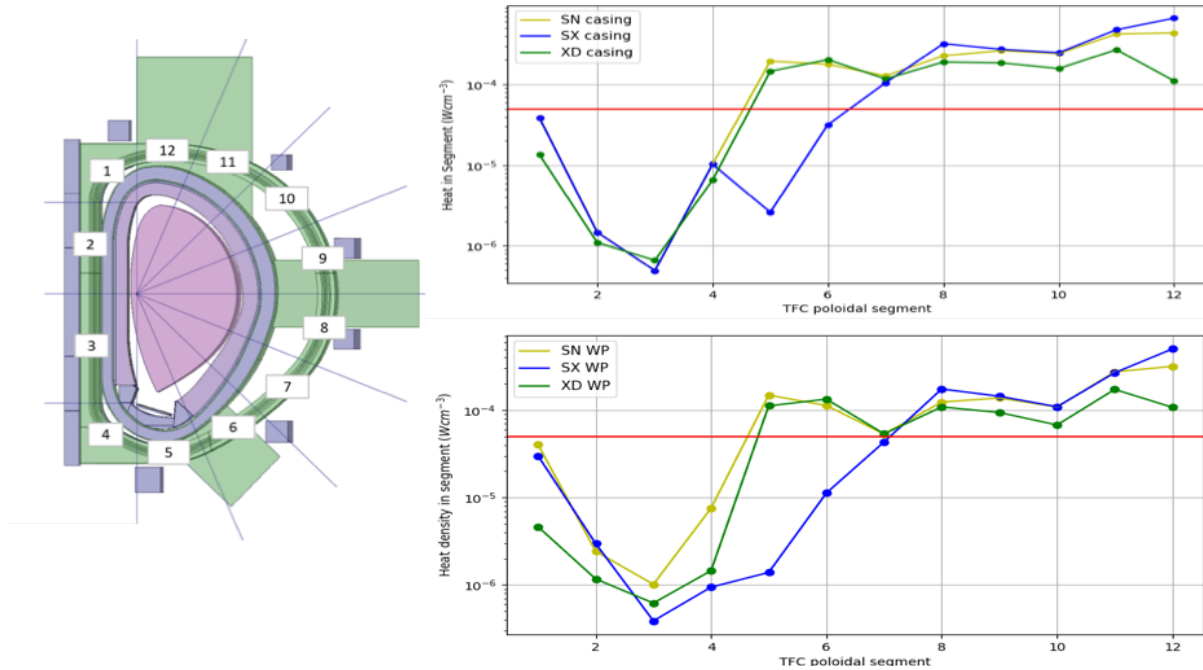


Figure 51: nuclear heating density through the TF coil casing (upper panel) and winding pack (lower panel). The red line shows the maximum load acceptable. The segment definition is given by the cross section of the tokamak on the left.

Two other important nuclear related quantities are the neutron induced damage accumulated by the materials (DPAs) and the helium production in the surrounding structures, which can affect the possibility to cutting/re-welding them. The limit to the DPA/FPY (DPA per Full Power Year) in Eurofer is 6 DPA over 1.5 FPY, therefore we can assume a limit of 4 DPA/FPY for the plots shown. In each case, the highest DPA values are recorded on the dome and on the part of the two vertical targets which sit almost below the dome. Our results show that the limit is exceeded only in the dome body of the SND, but the other configurations are close to this limit.

Table 13: DPA/FPY values for the different configurations in different areas of the divertor. The acceptable limit is 4DPA/FPY.

	DPA/FPY		
	SND	SXD	XD
Liner Body	4.14	3.94	3.36
Inner Vertical Target	2.85	3.14	0.65
Outer Vertical Target	2.99	0.34	1.16

Note, however that large uncertainties are attached with the estimates for the DPAs and different nuclear data libraries can give incompatible results. The table above should therefore be interpreted mainly for comparative purposes. With respect to helium formation, this does not raise concerns at the moment.

Finally, since the reactor needs to be self-sufficient in terms of tritium production, we need to maintain its breeding ratio (TBR) above one and avoid degrading it with the ADC designs. As can be seen from Table 14, the TBR in all the configurations is satisfactory and only slightly affected in the ADCs.

Table 14: Tritium production rate and total breeding ratio for the different configurations.

	Tritium Production Rate (#/s)						Tritium Breeding Ratio					
	SN		SX		XD		SN		SX		XD	
	TPR	Rel. Error	TPR	Rel. Error	TPR	Rel. Error	Total	Rel. Error	Total	Rel. Error	Total	Rel. Error
Total	5.12E+19	0.07%	5.03E+19	0.11%	5.03E+19	0.01%	1.15	0.07%	1.13	0.11%	1.13	0.01%
Li6	3.73E+18	0.05%	1.33E+19	0.03%	4.91E+18	0.01%						
Li7	1.06E+15	0.01%	4.55E+15	0.02%	3.02E+16	0.01%						

In future analysis, it would be a priority to capture more accurately the components/shielding in the port plugs which were left open apart from the presence of the blanket modules/divertor filling the openings. Also, quantities such as dose to insulation and the fast neutron fluence should be assessed in a more detailed analysis. These also have hard limits to prevent damage to the magnets. Like with the nuclear heating, these quantities need to be closely monitored and work with other teams is essential to reduce the loads early in the design stage.

5. The ADC continuum and Hybrid solution

Since it is the features of the different configurations that characterize them, and since such features are mostly in common, all the ADCs and the baseline configurations can be seen as part of a continuum of solutions, from more extreme to milder. In other words, between the SND and the SXD there is an infinity of configurations obtained by gradually shifting the outer strike point outwards. Naturally, this leads to a change of the overall performance and it is still unclear if this happens smoothly or it undergoes more sudden transitions (the analysis in this Section seems to suggest the former). It is worthwhile noticing that all the configurations can be topologically transformed into each other: the DND into the SND by gradually increasing the separation between the separatrixes, the SND and the XD by reducing the target poloidal field, and so on and so forth. Exploring this continuum could allow finding sweet spots where engineering is feasible, and margin is increased.

It is therefore not correct to attach to any configuration the absolute labels of “Super-X”, “Snowflake”, and so on. The studies presented in this report are particular incarnations of these abstract concepts and it is not excluded that different and better ones can be obtained with more thorough analyses and optimizations. In other words, it would be incorrect to say that our results provide the definitive answer on the “X-Divertor”, but only that they describe the particular physics and engineering of the X-Divertor configuration we have examined.

It is therefore conceivable to find a middle ground between a better physics solution (e.g. one that can handle the power with more margin) and more complex engineering. In this respect, the safest approach would be to start from the SND and move towards the most similar ADCs, which undoubtedly are the XD and the SXD, which just increase the flux expansion through different means. The SFD and the DND induce in the problem a secondary X-point and therefore more complex physics in terms of redistribution of power among the divertor legs, different drift effects, and X-point benefits related with the magnetic shear that are not yet completely understood (the SFD plus might be an exception to this, as it is more similar to the SND than the other configurations).

It was therefore decided to attempt to develop a new “hybrid” solution between the SND and the SXD in order to explore the continuum philosophy. This was done by redesigning the SND in such a way that its strike point was midway between its original value and the SXD’s, see Figure 52.

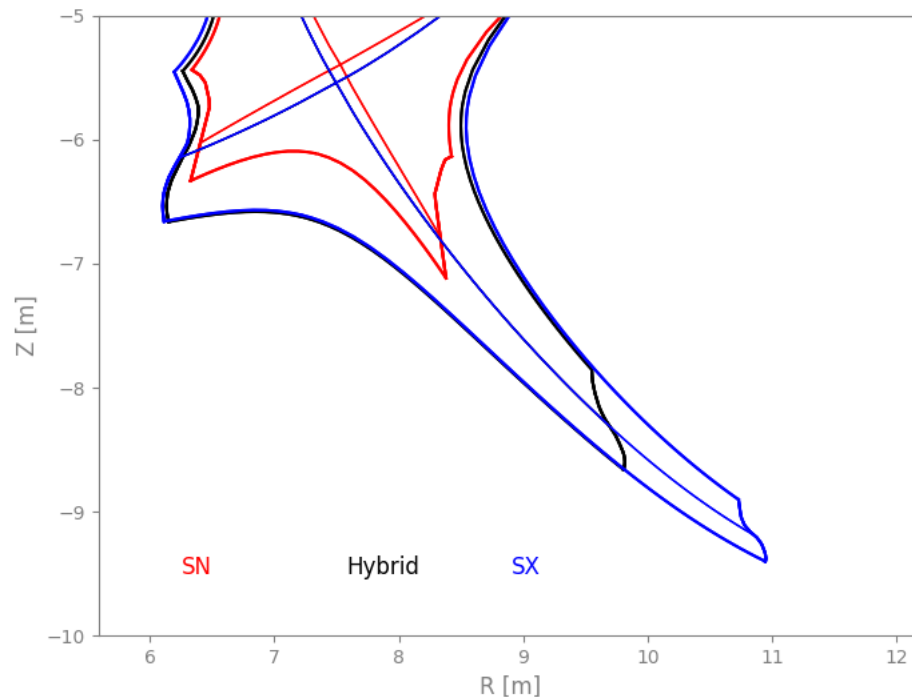


Figure 52: comparison between the divertors of the SND, hybrid and SXD configurations.

This also led to a poloidal flux expansion in between the two cases (smaller than for the SND but larger than the SXD). Importantly, while the poloidal and toroidal flux expansion change linearly between the two solutions, the outer connection length does not. Indeed, most of the connection length gain is obtained in the low poloidal magnetic field region around the X-point, which implies that the hybrid configuration has a rather long $L_{//}$, closer to the SXD than the SND (i.e. the connection length gains decrease with R). In particular, $R_t/R_x=1.3$ for the hybrid while it was 1.45 for the SXD and 1.11 for the SND. The outer poloidal flux expansion is $f_{x,t}=3.13$ to be compared with 2.4 for the SXD and 3.5 for the SND. The parallel connection length is compared between the three configurations in Figure 53.

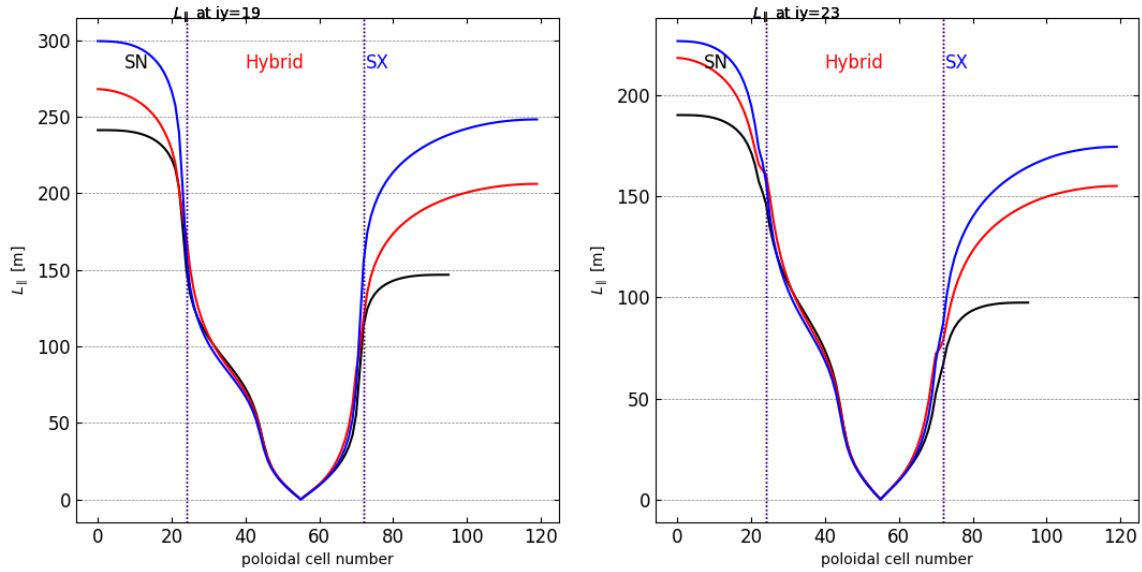


Figure 53: parallel connection length for the SND, hybrid and SXD configurations as a function of the poloidal cell number in SOLPS (equivalent to moving poloidally around the machine). The outer midplane is chosen as the reference point where $L_{||}=0$. The left and right panels show $L_{||}$ at around 1mm and 3mm from the separatrix at the outer midplane, respectively.

According to these results, we expect the hybrid to perform in between the SND and the SXD, potentially closer to the latter.

Two new equilibria and associated engineering configurations were generated for the hybrid solution. One had standard vacuum vessel shaping with an additional passive stabilizing plate compatible with the breeding blanket and the second had an optimized vacuum vessel following the curvature of the FW to bring passive structures closer to the plasma, see figure below:

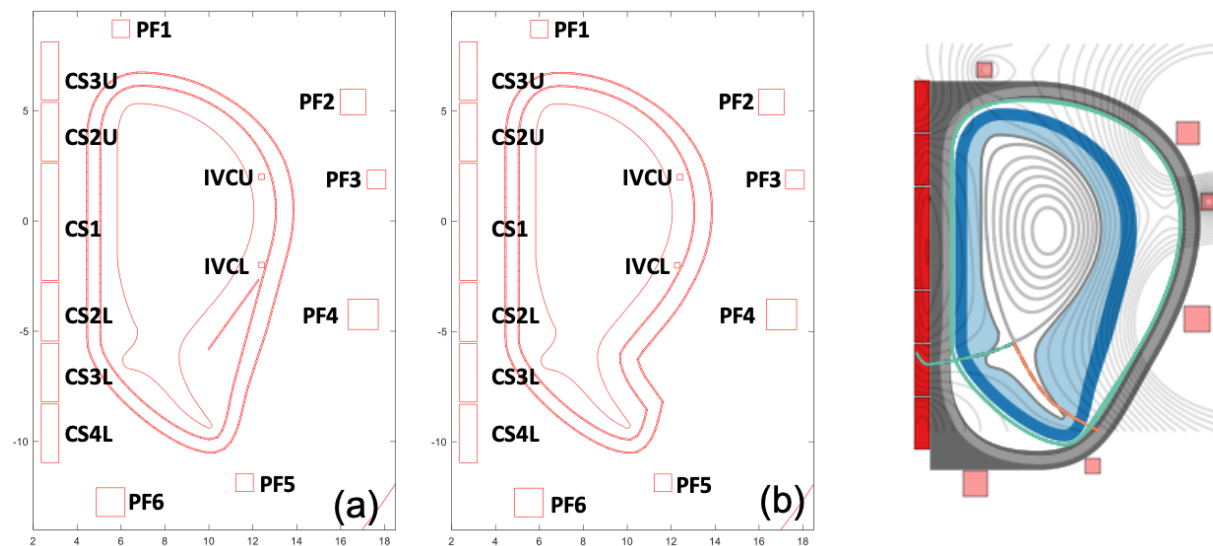


Figure 54: the two hybrid configurations considered in our analysis. On the right full cross section.

Considering the challenging control issues experienced in the baseline and ADCs, both geometries have been equipped with 2 IVCs for active control purposes.

In terms of physics, the hybrid configuration behaves as expected, having a performance roughly in between the SND and the SXD, as the figure below shows:

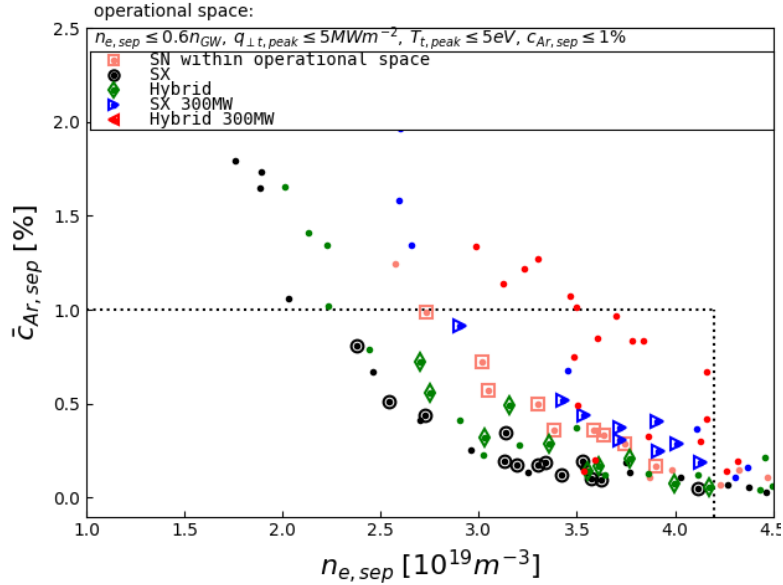


Figure 55: Core argon concentration at the separatrix as a function of the separatrix density for the SND (pink), SXD (black), hybrid (green). The full symbols are simulations in the operating space, while the individual dots represent simulations that are not in the operating space. Blue and red symbols represent the SXD and hybrid simulations at $P_{SOL}=300MW$ (only the SXD has points in the operating space).

This is also confirmed by plotting the operating spaces for 150MW crossing the separatrix. These are compared in Figure 56.

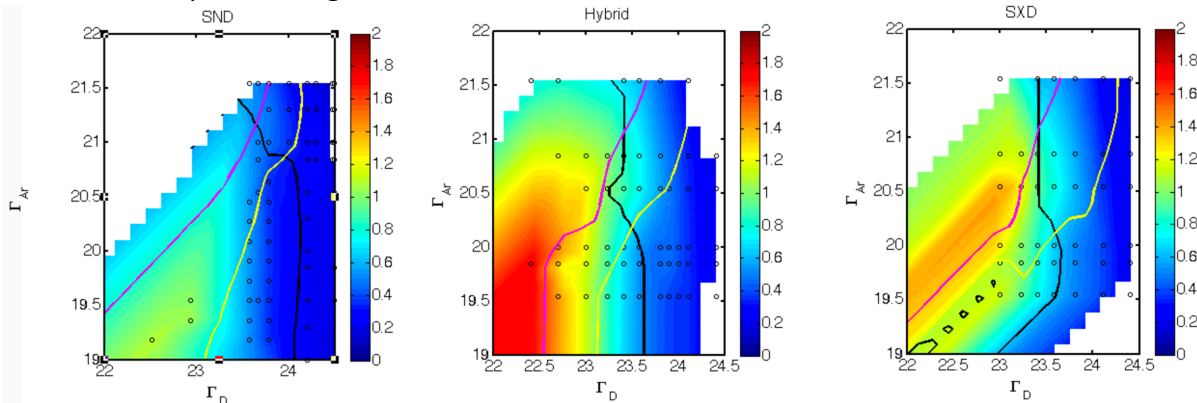


Figure 56: comparison between the SND, Hybrid (center) and SXD (right) operating space. The symbols and lines are consistent with those in Figure 4 and explained in the text above it.

The operating space is marginally smaller than the SXD but significantly larger than the SND. The fact that the Hybrid operating space is closer to the SXD than the SND might be a confirmation of the role of the connection length, which for the hybrid is closer to the former.

While a campaign of hybrid simulations at $P_{SOL}=300MW$ was successful and converged, no operating space was found for this configuration at higher power. On the other hand, a couple of points were close to be acceptable, which suggests that also in terms of power handling the hybrid is better than the SND (but worse than the SXD). Interestingly, this seems to be confirmed by the fact that the hybrid radiation is mostly localized below the X-point, as in the SXD configuration. The results obtained thus confirm that the continuum of the configurations seem to show smooth transitions between one design and another (at least between the SND and the SXD).

Both a Random Sampling and Princeton-D Morphing methods were used to create TF coil geometry. The structural calculations, performed with the stress intensity criterion, still show problematic points in several regions of the outer limb of the coil (see Figure 57), which suggests that this preliminary design still requires improvements (a working point should exist assuming that the SND and the SXD have one, see Section 4.1). It is possible, for example, that moving the PF4 and PF6 outward would be beneficial as this could lead to more D-shaped profiles (this has not been attempted because of lack of time).

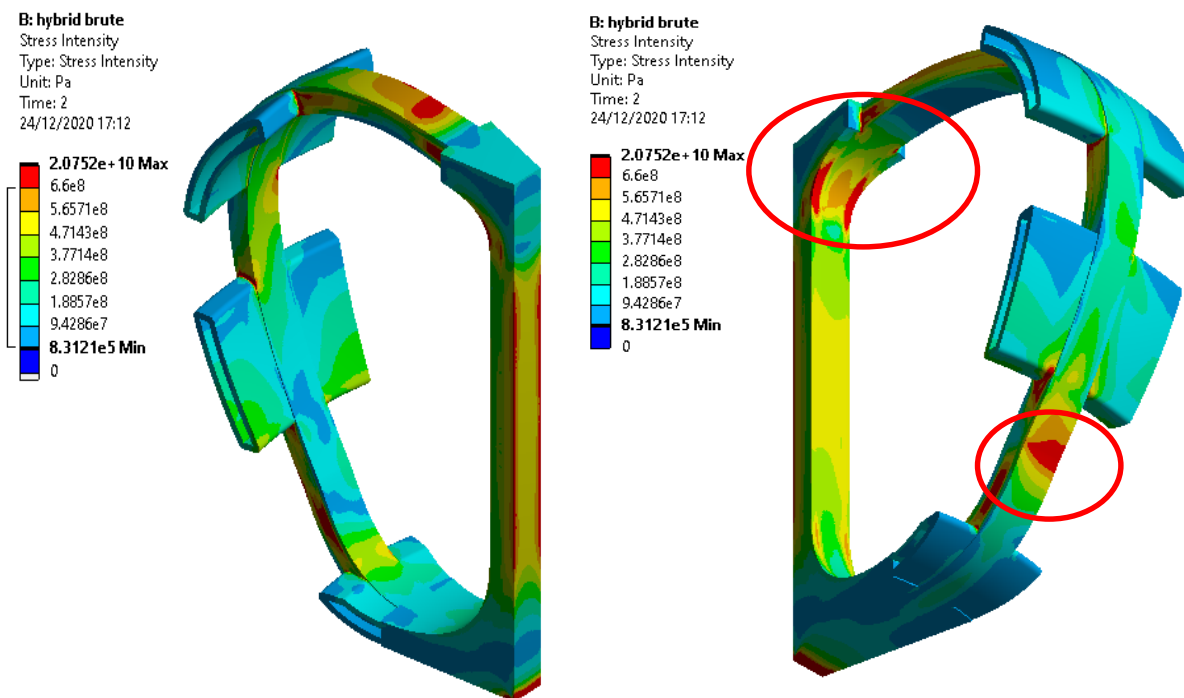


Figure 57: two views of the stress maps for the hybrid TF coil. The two red circles show where the stresses exceed the threshold.

Moving now to control, passive vertical stability is not problematic, and the optimized vacuum vessel and the stabilizing plates perform similarly, see table below:

Table 15: hybrid passive vertical stability.

Configurations	Scenario snapshot	With Optimized VV		With stabilizing plate	
		γ [s^{-1}]	m_s	γ [s^{-1}]	m_s
SX-Hybrid	FT	1.98	0.99	2.06	0.97
	FT_li1	2.17	0.88	2.31	0.85
	SRD	5.29	0.50	5.67	0.48

If perturbed, the hybrid responds with the usual ELM or MD variations (see Section 4.2) a displacement slightly higher than the SND but much better than the other ADCs is now achieved (compare Table 6):

Table 16: response of the plasma centroid to imposed perturbations of the equilibrium parameters.

Configuration	ΔZ_0 [cm] With optimized VV	ΔZ_0 [cm] With stability plates	Disturb
SX-Hybrid	5.5	5.3	ELM
	6.8	-6.4	MD

The analysis of the power needed by the control system to return the plasma to its original position after displacements was done only for the case with internal coils, giving results aligned with the SND (10-20MW in the worst-case scenario of 15cm displacement in the SRD phase and much smaller in all the other cases).

6. Conclusions and recommendation

The results reported in this document provide a comprehensive overview of the current knowledge of the physics and engineering of the alternative divertor configurations for reactor scale machines. For its breadth, this is probably the most thorough study performed so far in the fusion community. Despite that, many results have a significant margin for improvement both in physics and engineering. Despite that, a rigorous approach to standardization of the tools and documentation of the procedure was enforced, so that the baseline and ADC solutions can be fairly compared. In other words, while absolute numbers can and should be questioned in basically all the results presented, the comparisons are solid, and the relative merit of each solution can be assessed with relative confidence (given the models used).

It was shown that physics predictions are still quite challenging despite the progress achieved in the last few years. It was essential to progress our understanding in a coordinated way, with state-of-the-art codes and standardized approaches. Multifluid simulations showed an increased margin in the operating space of the SXD and XD with respect to the SND. Order two factors in the separatrix density, minimum impurity concentration and seeding, maximum power handled were observed. While this might not seem much, it is indeed a significant margin, especially when coming to handling the power flowing towards the targets. While more sophisticated models might well change the margin, it is judged unlikely they will change the trends. Turbulence simulations in 3D have shown a different behavior of the fundamental structures causing the transport in the ADCs. More analysis is required to assess the impact of this observation, but it would be important to incorporate poloidally varying and ADC dependent transport coefficients in the multifluid runs in order to have more accurate predictions.

From the engineering point of view, we have shown that all ADCs can be designed with a set of TF and external PF coils, although accommodating the potentially beneficial features imposes some additional constraints. These result in deformed TF coils, and PF coils in inconvenient positions or too far away from the plasma. Stress levels in the TF coils are large and close to the limits but, in certain cases, they are comparable to the simplified WP-DTT1/ADC SND. The fact that the PF coils are on average far from the plasma implies that control with only external coils is expensive and likely unfeasible. On the other hand, also in this case, the problem is shared by the SND solution, although in a milder way (still hundreds of MW would be needed to stabilize the plasma at the start of ramp down). Internal vertical stabilization control coils would provide a solution to this problem but are likely to open others due to their survival in a nuclear environment and their challenging remote maintenance and installation procedures. Control becomes crucial whenever the benefits of

a configuration require precise control of a secondary X-point (e.g. SFD, DND). It is therefore concerning that the SFD (ideal and minus) appears to be very sensitive to perturbations (the SFD plus could therefore be more suitable as a potential solution). Remote handling in general appears to be more complex for most ADCs, but a number of potential solutions were identified. Neutronics analysis does not show major differences between the baseline and SND configuration, especially as far as the TBR and nuclear heating in the coils are concerned (when differences exist, they are typically in favor of the ADCs).

It is therefore evident that all ADCs will come at a cost, both financial and in engineering complexity. However, it is the Project Leader opinion that in this phase the exhaust challenge cannot be quantified with a continuous variable like cost, but rather with a binary one: are we completely confident that the baseline exhaust solution will work or not? If we still have some residual doubt, the cheaper option might turn out to be the most expensive, as its real cost would be a solution that does not deliver. In other words, ADCs should be seen as an insurance policy rather than a bargain.

From the data collected over the years by WP-DTT1, and reported in this document, it clearly appears that no ideal solution to a fusion reactor's exhaust problem exists and that large uncertainties still surround its physics and engineering. While ADCs promise benefits, they are neither so evident or confirmed enough that moving decidedly in their direction can be agreed confidently without risks. On the other hand, both progress in theoretical tools and experimental results might well be too slow on the ambitious (but needed) DEMO timescale.

First principle modelling is essential, but the capability of carrying out reliable simulations requires a coherent and targeted effort since present day codes, both turbulent and multifluid, do not appear to be capable of providing simulations that are at the same time well resolved, physically relevant and computationally reasonable. The modelling work of WP-DTT1/ADC, while as advanced as possible, has shown all the limitations of our current capabilities when predictive simulations for reactor design are concerned. Without a serious and coherent European effort, such a solution might well take a few decades. Similarly, experimental results will soon be able to rely on a number of new machines with ADC capabilities, but none of them will be able to reproduce DEMO conditions and their results should be carefully and skeptically scrutinized to assess reactor relevance, which in some cases could be marginal. The big value of these devices will therefore be in investigating fundamental mechanisms of ADC physics, but this has to be matched by an equal effort in understanding extrapolation, especially in a subject like exhaust where size matters (and might well be the fundamental driver).

At the same time, the ITER single null solution presents problems as well, some of which are common to the ADCs. While the experimental maturity of this concept is undisputed for present day machines, the uncertainty surrounding the extrapolations to reactor scales is not smaller than for ADCs, since all these divertor concepts are based on the same physics. If we are skeptical about the ADC physics, how can we not be of the SND predictions, which are based on the same tools and models? The larger validation database for the SND might be a reason, but the ability to interpolate well does not imply ability to extrapolate equally efficiently.

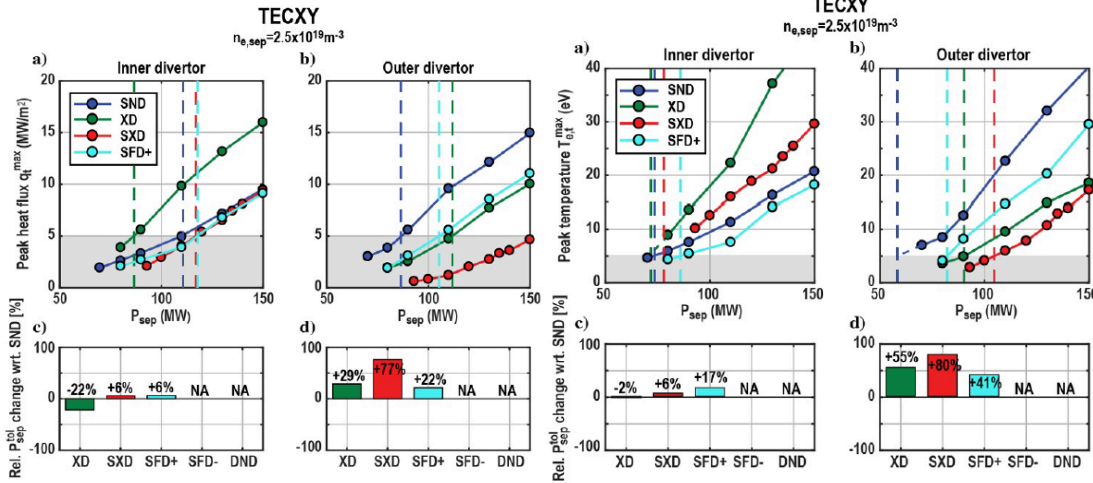
With this in mind, it is evident that large uncertainties still surround the problem, despite the significant progress achieved in the last few years. The personal opinion of the Project Leader is therefore there are only two reasonable paths. The first is to try to ensure as much margin as possible in both the physics and engineering, so that potentially negative surprises could be mitigated, while maintaining an aggressive timeline for the reactor design. It would be wise, however, to remain as close as possible to solutions that we currently judge the most reliable. This would imply moving in the neighborhood of the baseline solution, making relatively small changes that can provide more margin. In this category could fall the hybrid SND/SXD, an attempt to maximize the poloidal flux expansion at the target (quasi-XD), potentially a SFD plus if the secondary X-point can be sufficiently controllable. Obviously, not all these options are equally mature, and we have focused our attention only on the first (an early selection of maybe one or two alternatives would be useful). The second path would be to maintain complete flexibility in the design in order to adjust to new and potentially disruptive or groundbreaking discoveries or innovations. This option, obviously, would require significantly more resources and a structure that can adapt in an agile way to change. The repercussions on the machine integration would be potentially so massive for a DEMO size device that this second approach might well be unfeasible or, at least, difficult (but maybe not impossible).

Appendix I

Two codes were used to simulate the ADCs in the early years of the work package: TECXY [Zagorski R. and Gerhauser H. (2004) Phys. Scr. 70 173] and SOLEDGE2D [Bufferand H. et al (2013) J. Nucl. Mater. 438 S445].

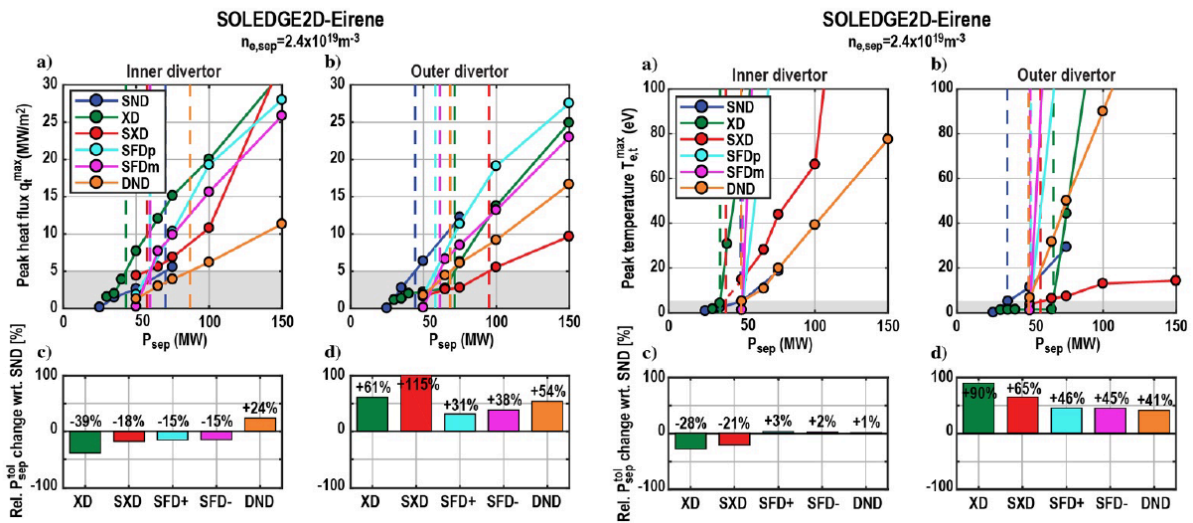
TECXY simplifies the target geometry by assuming a perpendicular incidence of the flux surfaces at the target and uses an analytic model for neutral particles (its applicability is limited once the interaction with neutrals becomes significant). The perpendicular heat flux at the target is then deduced from the grazing angle of the field line and the calculated parallel heat flux. The code was applied to all the ADCs, but intrinsic limitation of the code cannot allow topologies with multiple X-points, so that a SFD plus was considered with larger separation of the X-points than the standard SFD, limiting the extent of the considered PFR to the region between primary and secondary X-point.

The results of the code suggest that the ADCs can tolerate more power crossing the separatrix before the heat fluxes and temperature at the target become too large, at least as far as the outer target is concerned. For the inner target, the XD shows a worse performance than the SND. Again, these results do not account for radiation physics in the divertor, which can change things quite significantly. Also, the SFD used is not entirely compatible with the simulations done later on.



Some simulations with Ar seeding at constant separatrix density and power were carried out, showing an improved ability to handle the heat loads and the target temperature, but this was already expected. Also, it was shown that the impurity level at the separatrix was lower (Z_{eff} was around 40% lower) in ADCs than in the SND for the same radiated power in the divertor.

Simulations were also carried out with SOLEDGE2D, which included a more realistic description of the topology of the equilibrium and a kinetic neutral treatment.



The SOLEDGE2D simulations have a qualitative but not quantitative agreement with the TECXY results. All configurations have a better handling of the power at the outer target, but the inner target shows more marked asymmetries than TECXY. We cannot speculate the reason for this, but the lack of Ar radiation and the consequent lack of modification of the local temperature profiles suggests that the asymmetry considerations cannot be completely reliable.

As more recent simulations have shown, it is important to explore the whole parameter space, varying both the seeding and the fueling level in the machine in order to have a fair comparison. Indeed, fixing the impurity level or the separatrix density can be too restrictive

and does not allow to identify the optimal operating point of the divertors. In addition, the lack of a proper treatment of the seeded impurities (not evolved, mocked up by a P_{sep} reduction), which is extremely important to assess detachment properties, is a severe limitation of this approach. As a consequence, the simulations discussed here should be considered as a first partial attempt at analyzing the performance of the different configurations rather than a definitive answer on how the ADCs compare to the SND and to each other.

Appendix II

The code used to generate the grid is DivGeo (DG), which is the standard tool for SOLPS meshing. It was decided to use the 96x36 grid point SND configuration generated by Fabio Subba as a reference for alternative configurations. It was agreed to have the mesh done by the person that will work on the configuration, with the Activity Coordinator (Leena Aho-Mantila) providing review for all the meshes generated in order to ensure consistency of all simulations. The reference grid files were put on a machine that was easily accessible to all members of the team (the AUG cluster). It was decided to have centralized SND input files that were used as reference. These SND input files were fully compatible with specifications given below. Each person responsible for the work on the different ADCs copied those files for their own branch without changing anything. Any deviation from the standard approach was to be discussed and reviewed by the group.

The upstream heat flux decay length, λ_q , was set to 3mm for all configurations. This is not based on physical scalings, which are not available for completely detached divertors and radiative core conditions (DEMO operational regimes), but on the fact that we needed a reasonable reference for a fair comparison between configurations. The way to set this SOL width will be discussed in the following, here the emphasis is on the resolution of the mesh, and on the fact that the decay length needs to be resolved by at least 3 poloidal grid points. The reference grids have 18 points inside the separatrix and 18 outside. Using a variable resolution grid with a factor ~ 1.07 radial increase in the spacing between two points [$\sum_{k=0}^{N-2} \delta^k \lambda_q = (1 - \delta^{N-1})\lambda_q / (1 - \delta)$, with $\delta=1.07$ and $N=18$] this gives a total gridded SOL width of $\sim 30\lambda_q$, corresponding to roughly 8-9cm at the upstream midplane (to be precise, $\delta_1=0.001$ and $\delta_2=0.15$ in DG). The outer limit is given by the beginning of the wall shadow (first interaction point close to the secondary X-point on top of the machine).

In ADCs, the resolution upstream, downstream and at the X-point was maintained more or less the same, which means that the number of grid points can be increased to accommodate the different magnetic geometry. Unfortunately, the SFD configurations cannot satisfy these conditions, considering that the flux expansion at the X-point is significantly different from other designs.

The depth of the grid in the core is around 15-20 ion Larmor radii, around 10cm in order to allow for future pedestal studies. The depth of the grid in the PFR, instead, is roughly determined by the radial width of the SOL in the main SOL at the level of the X-point.

Regarding the simulation set-up, it was decided to use the same version of the code: SOLPS 3.0.6 develop. All problems with the code should be discussed via [Slack](#). The simulation uses fluid neutrals. All the simulations will use deuterium as the main fuel (tritium will be assessed in the future, but was deemed unimportant for the moment), Helium as an intrinsic impurity and Argon as a seeded impurity for divertor heat load control. Argon was included in the fluid simulations (neutral, fully stripped and everything in between bundled together).

The procedure agreed was to proceed by doing a fueling (gas puff) and seeding scan, while coarse power and λ_q scans (3 points each) were left for the future (although a number of configurations did do the power scan already). The philosophy was to use engineering parameters without any sort of feedback.

Each “matrix scan” was preceded by a single fluid simulation per ADC, aimed at assessing the feasibility of the approach, the convergence of the code and the performance of the mesh. These initial fluid simulations were performed at 150 MW of input power and 4×10^{19} separatrix density in density feedback and provide a way to “anchor” the matrix scan.

The sources were calculated in the following way: assuming a 2GW reactor, the rate, α , at which He is produced is given and is: $2 \times 10^9 \left[\frac{J}{s} \right] = \alpha \left[\frac{1}{s} \right] \times 2.8 \times 10^{-12} [J]$, where $2.8 \times 10^{-12} J$ is the energy released per reaction (17.6 MeV). It is therefore easy to see that the He production rate is around 7×10^{20} ions (α particles) per second. This is the value that will be used as core He rate in the simulations. For the Deuterium, we assume a factor 50 with respect to the He, and hence the core rate will be 3.5×10^{22} nuclei per second (see discussion below). The Ar seeding will be fixed at 0.1% of the total D rate (puff+core) and injected from the same midplane nozzle as the D puff. Finally, the initial D puff was determined by the first feedback simulations in order to get $4 \times 10^{19} \text{ m}^{-3}$ separatrix density.

As far as the dissipative coefficients are concerned, we used ITER as a guideline for the modelling, lacking better theoretical or experimental indications (this is a big gap in our understanding, but the simulations are comparative in nature, so that an arbitrary choice in the decay length might not affect the overall trends). In particular, ITER uses $\chi_e = \chi_i = 1 \text{ m}^2/\text{s}$ and $D = 0.3 \text{ m}^2/\text{s}$ in the SOL, dropping to $0.2 \text{ m}^2/\text{s}$ for all the coefficients in the core (the latter representing neoclassical values). All the ADC simulations were performed with $\chi_e = \chi_i = 0.3 \text{ m}^2/\text{s}$ and $D = 0.1 \text{ m}^2/\text{s}$ in the SOL, thus maintaining the same ratio as ITER, reducing the perpendicular transport to compensate the reduced parallel transport (due to longer connection length). This gives $\lambda_q \sim 3 \text{ mm}$ for the SND, which was used as a reference. For the same dissipative coefficients, the other ADCs have slightly different decay lengths, but always around 3mm. In the core, all the DEMO parameters were reduced to $0.1 \text{ m}^2/\text{s}$ to simulate the pedestal region. The transition between the SOL and the core was governed by a connecting function thus defined: the separatrix parameters are the same as the SOL parameters; the transition region covers 5 mm inside the separatrix; at -5mm, the core parameters are used; at -2.5mm we take the geometric mean between the core and SOL parameters (truncated to the first decimal), hence $\chi_e = \chi_i = 0.17 \text{ m}^2/\text{s}$. For lack of a better estimate, the viscosity was taken at $0.2 \text{ m}^2/\text{s}$, as in ITER.

In the “matrix” scan, the higher gas puff rate is limited by the Greenwald limit. We estimated that 4×10^{19} separatrix density will be close to the limit, assuming 7×10^{19} Greenwald density, similar to ITER (where it is 8×10^{19}). The range of the Ar scan was constrained by the impurity separatrix concentration (below 1%). Finally, the input power was held fixed at 150MW initially, expecting roughly 10% of the input power to be radiated in the core, so that $P_{\text{sep}} \approx P_{\text{input}}$. In certain configurations the power crossing the separatrix was changed to 50MW or 300MW in order to have a feeling for the power sensitivity of the results.

Other specifications are as follows. The single feedback simulations were started with flat initial conditions. The single test simulations developed first for each ADC were used as initial condition for all matrix scan simulations in order to allow for parallel calculations and faster convergence. The recycling coefficient in all simulations was set to 1, as we are considering steady state conditions and saturated walls. Regarding kinetic corrections, we will take flux limiters for ions, electrons and neutrals. In particular, for lack of better models, we will use the values employed in ITER’s simulations (Kukushkin): 0.2 for the electron heat flux, 10^5 for the ion heat flux and 0.375 for the viscosity. For the neutral fluid model, we will take 1, consistently with Dave Coster’s simulations. The neutral diffusivity is calculated by the code and the maximum and minimum values are bounded.